NOTICE

The quality of this microform is heavily dependent upon the quality of the original thesis submitted for microfilming. Every effort has been made to ensure the highest quality of reproduction possible.

If pages are missing, contact the university which granted the degree.

Some pages may have indistinct print especially if the original pages were typed with a poor typewriter ribbon or if the university sent us an inferior photocopy.

Previously copyrighted materials (journal articles, published tests, etc.) are not filmed.

Reproduction in full or in part of this microform is governed by the Canadian Copyright Act, R.S.C. 1970, c. C-30.

AVIS

La qualité de cette microforme dépend grandement de la qualité de la these soumise au microfilmage. Nous avons tout fait pour assurer une qualité supérieure de reproduction.

S'il manque des pages, veuillez communiquer avec l'université qui a conféré le grade.

La qualité d'impression de certaines pages peut laisser à désirer, surtout si les pages originales ont été dactylographiées à l'aide d'un ruban usé ou si l'université nous a fait parvenir une photocopie de qualité inférieure.

Les documents qui font déjà l'objet d'un droit d'auteur (articles de revue, tests publiés, etc.) ne sont pas microfilmés.

La reproduction, même partielle, de cette microforme est soumise à la Loi canadienne sur le droit d'auteur, SRC 1970, c. C-30.

Canada

THE UNIVERSITY OF ALBERTA

Dose Calculations for Megavoltage Photon Beams
Using Convolution

BY

G. COLIN FIELD

A THESIS

SUBMITTED TO THE FACULTY OF GRADUATE STUDIES AND RESEARCH

IN PARTIAL FULFILMENT OF THE REQUIREMENTS FOR THE DEGREE

OF MASTER OF SCIENCE

IN

MEDICAL PHYSICS

DEPARTMENT OF PHYSICS

EDMONTON, ALBERTA
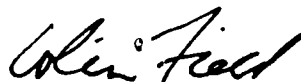
SPRING, 1988

ISBN 0-315-42823-6

THE UNIVERSITY OF ALBERTA

RELEASE FORM

Name of Author: G. COLIN FIELD

Title of Thesis: Dose Calculations for Megavoltage Photon Beams Using Convolution

Degree: Master of Science

Year this Degree Granted: 1988

Permission is hereby granted to THE UNIVERSITY OF ALBERTA LIBRARY to reproduce single copies of this thesis and to lend or sell such copies for private, scholarly, or scientific reseach purposes only.

The author reserves other publication rights, and neither the thesis nor extensive extracts from it may be printed or otherwise reproduced without the author's written permission.

Colin Field

7424 32 Avenue

Edmonton, Alberta, T6K 1J8

Date: _27 April, 1988_

THE UNIVERSITY OF ALBERTA

FACULTY QF GRADUATE STUDIES AND RESEARCH

The undersigned certify that they have read, and recommend to the Faculty of

Graduate Studies and Research for acceptance, a thesis entitled, **Dose Calculations for**

Megavoltage Photon Beams Using Convolution, submitted by **G. Colin Field**

in partial fulfilment of the requirements for the degree of **Master of Science in Medical**

Physics.

Supervisor

Date: 27 April, 1988

ABSTRACT

Radiation therapy is used in 55% of all cancer patients treated in Alberta.

Fundamentally, the determination of dose requires the complete specification of the particle fluence as a function of particle type and particle energy, the tissue interaction coefficients in the patient, and the average energy deposited by these particles. The "Convolution" method simplifies the total fluence calculation to the determination of only the primary fluence. Kernels, which describe the energy spreading from a primary photon impulse site, are convolved with the primary fluence to yield the resulting dose distribution.

This work graphically displayed the convolution kernels obtained by Monte Carlo simulations in three Canadian laboratories (0.10 to 50 MeV), and in so doing demonstrated an error in the original calculation. The kernels have been recently regenerated by the National Research Council of Canada for world wide distribution. The corrected kernels have been analyzed, and are consistent with the physics of radiation transport.

Dose distributions in a homogeneous water medium were calculated using the convolution technique in both the real and Fourier domains; the application of Fourier techniques yielded a reduction in computation time of 14 times for a 64^2 dose matrix (i.e 22.5 seconds on a VAX 11/780 processor). The calculated results were compared to experimental dose measurements for Co-60 and 15 MV X ray beams and the agreement is good (within 3%) in a homogeneous medium. The results computed by the convolution technique were also compared to those calculated by a more conventional algorithm (CBEAM); convolution showed better agreement (5%-10%) with experimental data in situations requiring more predictive power (i.e. blocked field).

Unfortunately, the strict convolution technique is not appropriate in inhomogeneous media, although, its "cousin" superposition technique may be applied. The relationship between various dose calculation algorithms and the inherent assumptions have been documented. The ultimate goal remains to incorporate these algorithms into routine treatment planning in order to treat the cancer patient optimally with radiation.

ACKNOWLEDGEMENTS

I would like to express my sincere appreciation to the following who made this thesis possible:

My wife and daughter, Melissa and Katrina, who tolerated a part-time husband and father.

Dr. J.J. Battista for his enthusiasm, "blackboard sessions", and the constructive use of his red pen.

Dr. J.W. Scrimger for his late night help in taking dose measurements.

Dr. S.R. Usiskin and the Cross Cancer Institute, who aptly handled the administrative details which allowed me to complete my M.Sc. as a part-time employee.

Ernest Mah, for the use of his "dose difference" software and many informal discussions.

John Antolak, for assistance with the automated dose measurement system he developed.

Don Robinson, for destroying a weekend to proof-read this thesis.

Wayne Logus, for his renown scrounging ability.

Lee Santon of Abraxas Engineering, for his reliable library of software tools.

Dr. Rock Mackie and Mr. Rob Andrews for their ideas and computer programs.

Dr. A.L. Boyer for exciting me about Fourier space during a visit to our laboratory.

The Radiation Oncology department of the Cross Cancer Institute for the use of their computer facilities in the preparation of this thesis.

v

TABLE OF CONTENTS

viii

LIST OF TABLES

LIST OF FIGURES

Chapter 1

Introduction to Radiotherapy Dose Calculations

In the beginning.....

1.0   Introduction to Radiotherapy Dose Computations

Radiation therapy is one of the three common techniques used in the treatment of cancer. It is used to treat 55% of all cancer patients in Alberta, as part of the overall management of the disease. In using radiation, three basic strategies are currently followed in order to improve the probability of cure and minimize the chance of treatment complications:

1) A uniform high dose must be delivered to the target volume (e.g. zone of known disease, including pathways for spreading disease).

2) Specific critical structures must receive as little dose as is reasonably achievable (e.g. spinal cord).

3) Total energy delivered (or integral dose) to the entire patient should be minimized to improve the overall tolerance to irradiation (e.g. immunological competence).

These three requirements are all related to the quantity of dose delivered to a region in the patient. The absorbed dose, or dose, is defined as the energy absorbed from ionizing radiation per unit mass of tissue.

Thus, the problem in radiation therapy from a physical viewpoint is to predict and deliver a known quantity of dose to specified locations. The International Commission on Radiation Units and Measurements (ICRU) recommends that dose be *delivered* to the target volume with an error of less than ±5% (ICRU 24, p45-50). A similar argument has been made for normal tissue irradiation if the dose approaches the tolerance levels of normal tissue. This is only an estimate of the required accuracy since the clinical measurement of human response remains subjective. Nonetheless, increases in dose of 5-10% have certainly produced unexpected treatment complications (Task Group 10, 1975). Each step involved in the delivery of dose (machine calibration, patient positioning, dose

calculation) must therefore be performed with an accuracy better than ±5%. Cunningham (1982, p 103) has recommended that an accuracy of ±3% be achieved in the dose *computation* step of treatment planning.

In order to achieve this level of computational accuracy, the "input" to the calculation algorithm must be accurately known. Computed Tomography (CT) scans with X-rays or magnetic resonance yield the precise three dimensional (3D) description of patient anatomy required to localize tumour and normal tissues accurately, provided the patient is imaged while in the treatment position (Battista et.al. 1979, Henkelman et.al. 1984). The radiation sources and beam modifying devices can be accurately specified. Thus, one of the major causes of uncertainty during treatment planning lies in the dose calculation algorithm *per se*. For the computed dose to be accurate within ±3%, and assuming negligible (or random) errors resulting from the specification of the above "input" parameters, the dose calculation algorithm alone must be accurate to *better* than ±3%.

Accuracy is not the only "yardstick" to assess the performance of a dose calculation algorithm. There is a competing factor, calculation speed, which in general varies inversely with the accuracy of the calculation. For a dose calculation algorithm to be used clinically for interactive treatment planning, the calculation times must be reasonable. For example, the entire calculation of a 3D dose distribution of 64x64x64 points should ideally be a few minutes per beam[1]. To date, no calculation algorithm has achieved this combined level of accuracy and speed; the use of two-dimensional planning with methods of limited accuracy and acceptable speed (≈ 1 minute per beam) is today's common practice.

---

[1]Although "batch" processing may be tolerable for specific cases of clinical importance, it is not desirable for routine use.

The advent of a new calculation algorithm - the "Convolution method" - may change this situation (Mackie et.al. 1987, Boyer and Moc 1986, Ahnesjö et.al. 1987, Mohan et.al. 1986). However, before adopting an algorithm for clinical treatment planning, a series of questions should be answered:

- What are the implicit and explicit physical and mathematical assumptions?

- How accurate is the algorithm for test cases where dose measurements are possible?

- How long does it take to calculate a complete 3D dose distribution?

- Is the algorithm easy to use from an operator's point of view?

- How difficult is the algorithm to implement and maintain from a software perspective?

- Will the calculation assumptions affect the dose results to a level which is clinically significant (i.e. 3%)?

This thesis poses the fundamental question, "*Is the convolution algorithm clinically useful for calculating dose distributions for megavoltage photon beams?* ". This question will be answered by examining the previous questions. Thus, before determining the applicability of the convolution algorithm in solving the clinical problem, as depicted in Figure 1.1, we must first isolate the assumptions of the algorithm and verify its performance under the ideal conditions, as depicted in Figure 1.2. Table 1.1 summarizes the difference between these two situations. Comparisons between calculated results and experimental results should initially be performed in situations which match the "ideal situation" as closely as possible.

Primary collimator

Field flattening filter

Secondary collimator

Field modifying device

Patient or phantom

Target

Treatment table

Verification detector
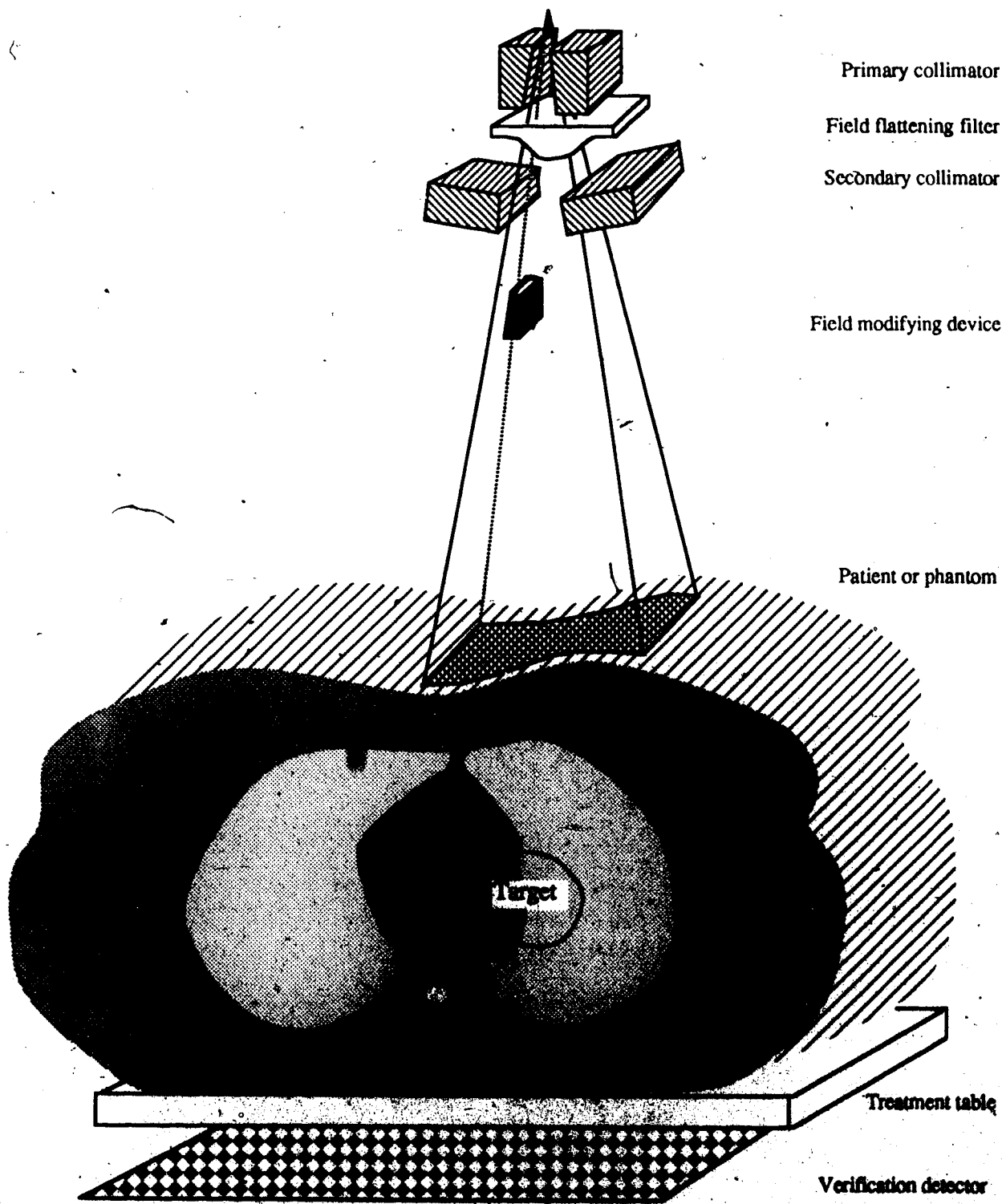
Figure 1.1. The "real" situation.
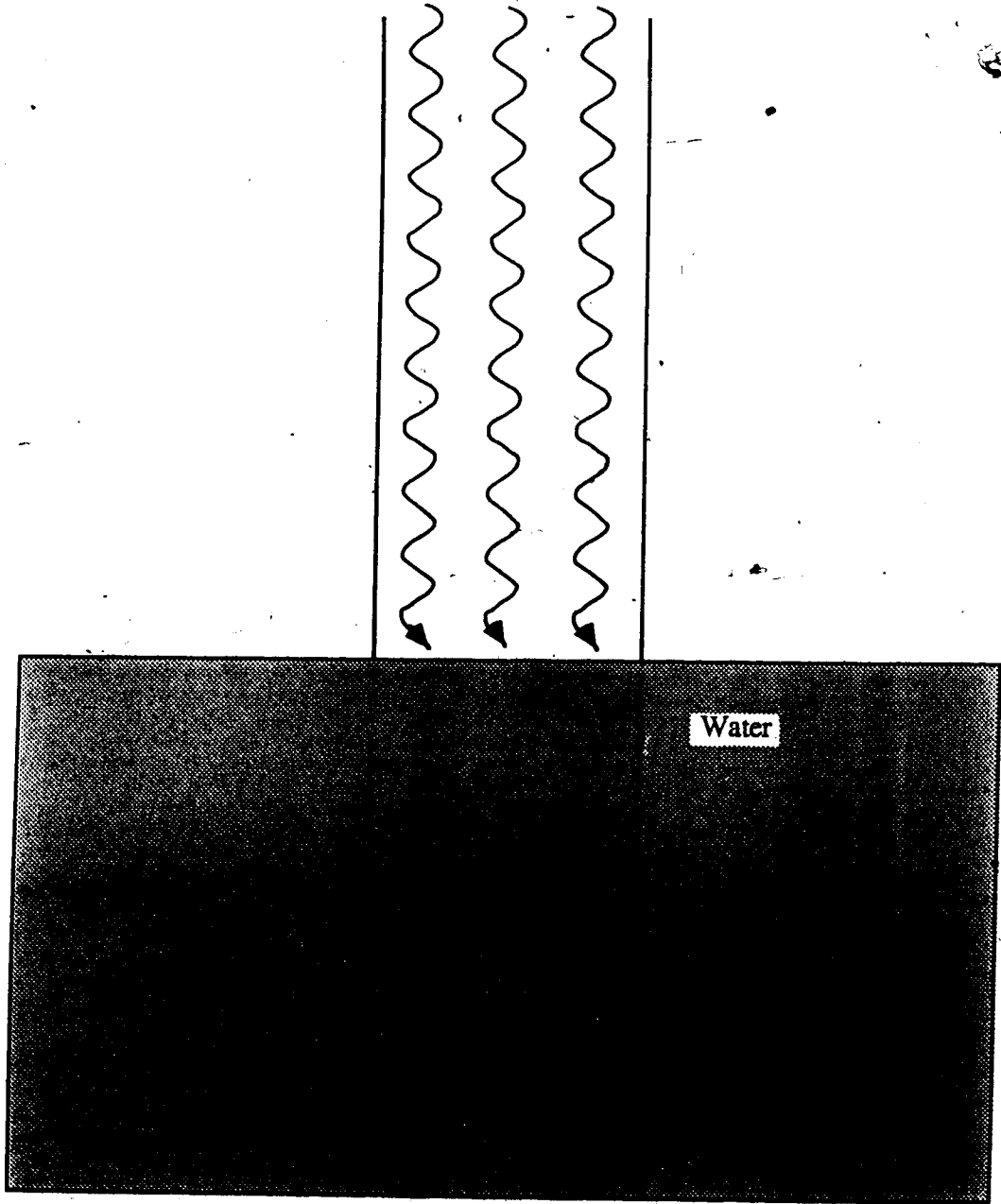
Figure 1.2. The "ideal" situation.

	"Real" situation	"Ideal" situation
inhomogeneous medium	yes	no
finite medium	yes	no
divergent beam	yes	no
poly-energetic beam	yes	no
non-uniform beam	yes	no
beam modifying devices	yes	no
dimensionality	3D	2D

Table 1.1.. Comparison of the "real" and "ideal" dose calculation situations.

The intent of this thesis is to demonstrate the feasibility of the "convolution" model under a restricted set of conditions (see Figure 1.2) before extending it to handle more complex situations. Thus, this thesis is intended to review the foundations of the convolution algorithm and provide a "solid footing" for its future evolution. A detailed investigation of this type is timely since many of the inherent assumptions have been obscured by frantic development (Convolution 1986).

The answer to the "fundamental question" is methodically developed through the following four chapters of this thesis.

Chapter 2 examines the interactions of radiation with matter. This presents a consistent and concise overview of the fundament concepts required to examine the physical basis of the convolution algorithm. The subjects to be discussed include: interaction mechanisms, radiation field quantities, the transport equation, and radiation equilibrium. These concepts are related through a most general expression for absorbed dose. This chapter concludes the introduction of concepts and Chapters 3 and 4 contain results of this investigation.

Chapter 3 begins by specifying the parameters required to define a dose calculation problem. The most general expression for the absorbed dose is then examined from a

number of different viewpoints. A Green's function formalism is eventually reduced to a superposition integral, which forms the basis of the convolution algorithm. The assumptions of this algorithm are explicitly stated, and the kernels required to evaluate the convolution integral are examined in detail. After the convolution integral is represented in a form amenable to machine computation, an interesting reciprocity relationship is examined.

Chapter 4 evaluates one-dimensional and two-dimensional convolutions in real space. After a review of Fourier techniques, the 2D convolution is performed using Fast Fourier Transforms. Comparisons are made between the two techniques for evaluating the convolution. Calculated results are compared to experimental data, and a discussion of the practical limitations and techniques for overcoming some of the convolution assumptions ensues.

Chapter 5 contains a general discussion of calculation algorithms using kernels, and a specific discussion of the convolution algorithm. Areas requiring further investigation in order to develop these "kernel based" calculation algorithms are suggested. The fundamental question posed by this thesis is answered in the conclusions to this thesis.

Chapter 2

Interaction of Radiation with Matter

Knowledge is of two kinds.

We know a subject ourselves,

or we know where we can find information upon it.

Samuel Johnson

9

2.0 Interaction of Radiation with Matter

This chapter summarizes the terms and fundamental concepts required to determine the dose distribution resulting from an arbitrary photon beam impinging on an arbitrary phantom, as depicted previously in Figure 1.1. It begins with a brief discussion of the mechanisms through which radiation interacts with matter. Quantities used to describe a radiation field (e.g. fluence, energy imparted) and its interaction with matter (e.g. interaction cross sections) are defined . These quantities are then used in specifying the 'absorbed dose'. It will be seen that the determination of fluence is a major problem and so particle transport equations and their solutions are briefly described. Radiation equilibrium is discussed as it relates to the simplification of the particle transport and absorbed dose problems.

We are interested in "absorbed dose" since it is related to the biological damage inflicted by ionizing radiation. Ionizing radiation consists of charged (e.g. electrons or positrons) and uncharged particles (e.g. photons) capable of causing ionizations. Ionizations may either be caused directly through interactions with the atomic electrons (e.g. Compton scattering); or, indirectly through interactions which produce particles capable of causing ionization directly (e.g. pair production).

Primary photons interact in a variety of ways which scatter or absorb the photon, and may or may not liberate a charged particle[2]. Charged particles are directly responsible for the deposition of energy in the medium. The number of interactions experienced by photons prior to their "death" or prior to exiting the medium are several orders of magnitude fewer than those experienced by electrons. For example, a 0.5 MeV electron makes about 100,000 collisions along its path, while a photon of the same energy would be completely absorbed after about 10 collisions in an infinite medium (Berger 1963). In a

---

[2]An interaction is considered a process that alters the direction and/or energy of the incident particle.

clinical situation, the approximate number of photons incident on a patient for a 'simple' 3

field treatment of a mediastinum, using 5 MeV photons in a 10x10 cm² field is in the order

of 10^{12} photons for a dose of 10 Gy. Thus, there are many interactions contributing to the

deposition of energy in a patient. The task of tracking each particle through its many

interactions in order to keep track of the energy deposition appears monumental. In an

effort to determine "how much" energy is deposited, let us first look at "how" energy is

deposited in a medium.

2.1   Interaction Mechanisms

Interaction mechanisms are the means by which ionizing radiation interacts with

matter. Interactions are characterized by interaction coefficients which are average

quantities dependent upon the type and energy of radiation, the type of matter to be

interacted with, and the type of interaction. The most fundamental interaction coefficient is

the (collision) cross section, σ, which is the probability of a single particle interacting with

a single target. Photon interaction coefficients to be discussed (section §2.1.1) are: linear

attenuation coefficents, mass attenuation coefficients, mass energy transfer coefficients,

and mass energy absorption coefficients. Charged particle interaction coefficients to be

discussed (section §2.1.2) are: total mass stopping power, collisional stopping power,

radiative stopping power, and linear energy transfer.

2.1.1   Photon Interactions

The photon interaction mechanisms are classified in Table 2.1 according to the

particle with which the photon interacts and the result of the interaction. Incident photons

used in radiation therapy have maximum incident energies of up to 30 MeV from

accelerators; so the **important interaction mechanisms** for the energy range of interest in this work are suitably highlighted.

These interaction processes are all statistical in nature. The probability of each competing process can be expressed as a collision cross section for the specific process. A collision cross section is the same as the linear attenuation coefficient if the presence of multiple targets does not affect the interaction probability (i.e. there is no 'shielding'). The interaction mechanisms with very small cross sections are deemed unimportant in this work and are dealt with in various references (Attix 1986, Fitzgerald et.al. 1967, Evans 1955, NBS 583, ICRU 28). The important interaction mechanisms will now be discussed .

interaction with	Result of interaction		
	Absorption	Elastic scattering (coherent)	Inelastic scattering (incoherent)
Atomic electrons	**photoelectric effect**	**Rayleigh scattering**	**Compton scattering**
Nucleons reaction	photonuclear scattering	Thomson scattering	Nuclear resonance
Electric field of charged particles or nuclei	**pair production**	Delbruck scattering	
Meson field of nucleons	photomeson production		

Table 2.1. Photon Interaction Mechanisms.

2.1.1.1 Photon Interaction Coefficients

Photon interaction coefficients are useful for characterizing interactions between photons and matter. The *total linear attenuation coefficient* , μ, can be used to determine the number of photons which have interacted while traversing a thickness, x, in a medium of density ρ.

$$N = N_0 e^{-\mu x} \tag{2.1}$$

where

  N is the number of particles that did not interact in traversing a
      distance x
  N_0 is the number of incident particles
  μ is the linear attenuation coefficient [cm^{-1}]
  x is the distance travelled in the medium [cm]

Thus, the number of particles "removed" from the beam is given by:

$$N_{interacted} = N_0 (1-e^{-\mu x}). \tag{2.2}$$

The total linear attenuation coefficient is determined by summing the linear attenuation

coefficients for each of the individual interaction processes.

$$\mu = \tau + \sigma_{coh} + \sigma_c + \kappa \qquad [cm^{-1}] \tag{2.3}$$

where

  μ is the total linear attenuation coefficient
  τ is the linear attenuation coefficient for photoelectric absorption
  σ_c is the linear attenuation coefficient for Compton scattering
  σ_{coh} is the linear attenuation coefficient for coherent (Raleigh)
      scattering
  κ is the linear attenuation coefficient for pair production

The *mass attenuation coefficient*, defined as the linear attenuation coefficient

divided by the density of the medium (μ/ρ), is a useful quantity since it is independent of

the actual density of the absorber. This stems from the fact that interaction probabilities are

expressible as cross sections per atom, $_a\tau$, $_a\kappa$, and $_a\sigma_c$. We can relate mass attenuation

coefficients to *atomic attenuation coefficients* ($_a\mu$) which describe the attenuation per atom

of the material (see equation 2.4).

$$\frac{\mu}{\rho} = \frac{N_A}{A} {}_a\mu \qquad [cm^2/g] \tag{2.4}$$

where

  (μ/ρ) is the mass attenuation coefficient [cm^2/g]
  N_A is Avogadros number [6.02205 X 10^{23} atoms/mole]
  A is the atomic weight [g/mole]
  $_a\mu$ is the atomic attenuation coefficient [cm^2/atom]

For Compton interactions, an *electronic attenuation coefficient* ($_e\sigma$) describing the attenuation per electron can be related to the atomic attenuation coefficient.

$$_a\sigma = Z \ _e\sigma \qquad [cm^2/atom] \quad (2.5)$$

where

    $_a\sigma$ is the Compton atomic cross section [cm²/atom]

    $_e\sigma$ is the Compton electronic cross section [cm²/electron]

    Z is the atomic number [electrons/atom]

Attenuation coefficients answer the question "How many interactions occur?", but if our interest is in the dose, we need to answer the questions: "How much of the incident photon energy is *transferred* to kinetic energy of charged particles?", and "How much of the transferred energy is actually *absorbed* by the medium?".

There are numerous references which define two or more terms in an effort to answer these questions. Unfortunately, there has been much variation in the use of words as well as their meanings (i.e. there is a significant difference between "imparted energy" and "energy imparted" (ICRU 33). A very lucid explanation of these terms has been given by Attix (1986).

The average energy transferred, $\overline{\epsilon}_{tr}$, is the average amount of the incident photon energy which is converted to kinetic energy of charged particles during the initial interaction of the photon. The average energy absorbed, $\overline{\epsilon}_{ab}$, is the average amount of the incident photon energy which is eventually absorbed by the medium from electrons during their slowing down process. There are two energy attenuation coefficients which characterize the energy tranferred and the energy absorbed.

The *mass energy transfer coefficient*, μ_{tr}/ρ, describes the average amount of energy transferred to kinetic energy of electrons due to the initial interaction.

$$\mu_{tr}/\rho = \mu/\rho \ (\overline{\epsilon}_{tr}/E_0) . \qquad [cm^2/g] \quad (2.6)$$

where

    $\overline{\epsilon}_{tr}$ is the average energy transferred to kinetic energy of electrons per initial interaction

    E_0 is the incident photon energy

The *mass energy absorption coefficient* , μ_{ab}/ρ , describes the average energy

absorbed by the medium during the slowing down process

$$\mu_{ab}/\rho = \mu/\rho \ (\overline{\varepsilon_{ab}}/E_0) \qquad\qquad [cm^2/g] \qquad (2.7)$$

where

    $\overline{\varepsilon_{ab}}$ is the average energy absorbed by the medium from charged
        particles

    E_0 is the incident photon energy

The two mass energy coefficients are related as follows:

$$\mu_{ab}/\rho = \mu_{tr}/\rho \ (1-g) \qquad\qquad [cm^2/g] \qquad (2.8)$$

where

    μ_{ab}/ρ is the mass energy absorption coefficient

    μ_{tr}/ρ is the mass energy transfer coefficient

    g represents the fraction of energy from charged particles which is
        re-radiated as bremsstrahlung radiation during the slowing
        down process. This fraction is assumed NOT to be locally
        absorbed and so does not contribute to dose. (i.e. g = [$\overline{\varepsilon_{tr}}$ -
        $\overline{\varepsilon_{ab}}$] / $\overline{\varepsilon_{tr}}$)

The mass energy transfer coefficient has the same units as the linear attenuation

coefficient and will always be smaller than the linear attenuation coefficient (see equation

2.6). The linear attenuation coefficient can be decomposed into: the energy 'transfer'

coefficient (μ_{tr}), and the energy 'scatter' coefficient (μ_s) according to conservation of

energy in the *initial* interaction:

$$\mu = \mu_{tr} + \mu_s \qquad\qquad [cm^{-1}] \qquad (2.9)$$

where

    μ is the linear attenuation coefficient representing the probability of
        any kind of interaction which "removes" a photon of energy E_0
        from the beam.

    μ_{tr} is the energy 'transfer' coefficient representing the energy
        initially tranferred to the medium.

    μ_s is the energy 'scattering' coefficient which represents the energy
        which is re-directed as scattered photons.

For example (see Figure 2.1), when a single 10 MeV photon interacts with carbon,
$\overline{\varepsilon_{tr}}$=7.30 MeV and $\overline{\varepsilon_{ab}}$=7.04 MeV (Johns and Cunningham 1983). This means that on
average 7.30 MeV is transferred initially to kinetic energy of the launched electrons and

only 7.04 MeV is eventually absorbed in the carbon. The difference, 7.30-7.04=0.26

MeV, is re-radiated as bremsstrahlung and not locally absorbed. The remainder of the

incident photon energy (i.e. the scatter component $\overline{\epsilon_s}$), 10.0-7.30=2.70 MeV, is scattered

from the beam. This energy distribution is shown in Figure 2.1.

The total attenuation coefficients, energy transfer coefficients and energy absorption

coefficients are averages based on the individual interaction coefficients. Now, let us look

at the individual attenuation coefficients for each of the major interaction mechanisms

(Table 2.1), in order of increasing importance as a function of increasing energy:

photoelectric effect, Rayleigh scattering, Compton scattering, and pair production.
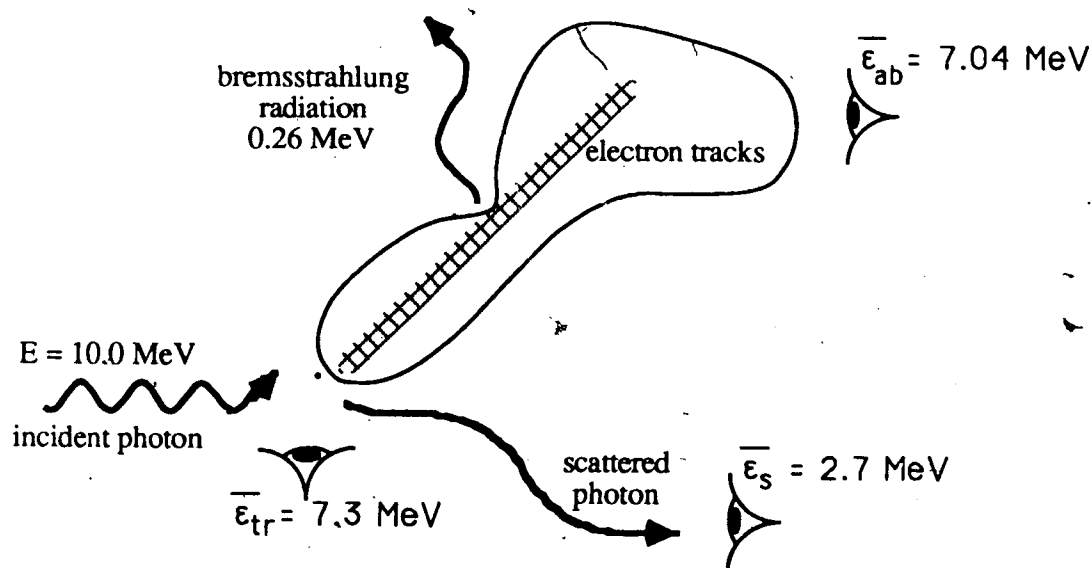
Figure 2.1. An example of the energy transferred, absorbed, re-radiated, and scattered.

2.1.1.2 Photoelectric Effect

The photoelectric interaction (see Figure 2.2) consists of a photon being absorbed

by an atom, and the subsequent ejection of a "photoelectron". The kinetic energy of the

ejected electron is equal to the photon kinetic energy less the electron binding energy. The

excited atom emits characteristic (or flourescence) radiation as it returns to the ground state.
Prior to leaving the atom, this flourescent photon may suffer an "internal photoelectric"
interaction ejecting an Auger electron. The photoelectric process accounts for 50% of the
interactions in water for photons with energies up to about 35 keV.
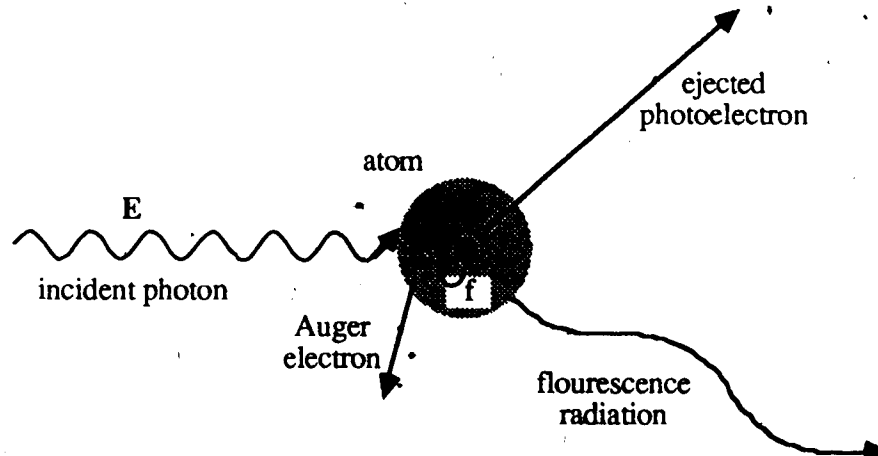
Figure 2.2. The Photoelectric Effect

Theoretical determination of the interaction cross sections are difficult presumably
because the atom is involved as a whole; photoelectric cross sections are therefore
predominantly empirical. The approximate dependence of the atomic cross section on
atomic number (Z) and incident photon energy (E_0) is well known (Johns and Cunningham
1983):

$$_a\tau \approx \frac{Z^n}{E_0^3}$$

(2.10)

where

n = 4.8 for biological material (Z<15)

$\quad$ 4.0 for 16<Z<82

The mass attenuation coefficient for the photoelectric effect is

$$\frac{\tau}{\rho} = {_a\tau} \, \frac{N_A}{A}$$

[cm²/g]   (2.11)

Since Z/A is roughly constant (except for hydrogen), the mass attenuation coefficent varies inversely with E_0^3 and proportionally to Z^n where n=3.8 for biological material or n=3.0 for higher atomic number materials.

The mass energy transfer coefficient is given by :

$$\tau_{tr}/\rho = \tau/\rho \ (1-\delta/E_0) \qquad\qquad [cm^2/g] \qquad (2.12)$$

where

   δ is the average energy of the incident photon 'escaping' as
      flourescent radiation. This corresponds to the binding energy
      less the energy imparted to Auger electrons.
   E_0 is the incident photon energy

Since the binding energy for biological tissues is about 500 eV, the photoelectron receives almost all the incident photon energy. Ignoring the flourescence radiation, $\tau_{tr} \approx \tau$:

The mass energy absorption coefficient is given by

$$\tau_{ab}/\rho = \tau_{tr}/\rho \ (1-g) \qquad\qquad [cm^2/g] \qquad (2.13)$$

where

   g is the bremsstrahlung radiation from all photoelectric and Auger
      electrons

Since the energy of the photoelectrons and Auger electrons is in the order of binding energies , the production of bremsstrahlung is negligible (see section §2.1.2.1). Thus, $\tau_{ab} \approx \tau_{tr} \approx \tau$.

2.1.1.3   Rayleigh Scattering

In contrast to the photoelectric absorption of a photon, Rayleigh scattering occurs,

when bound atomic electrons cooperatively scatter an incident photon (see Figure 2.3).

This is a coherent elastic scattering process confined to small angles,which can contribute

up to 10% of the total interaction cross section for incident photons below 0.1 MeV in

water.

scattered
photon

electrons
in atom
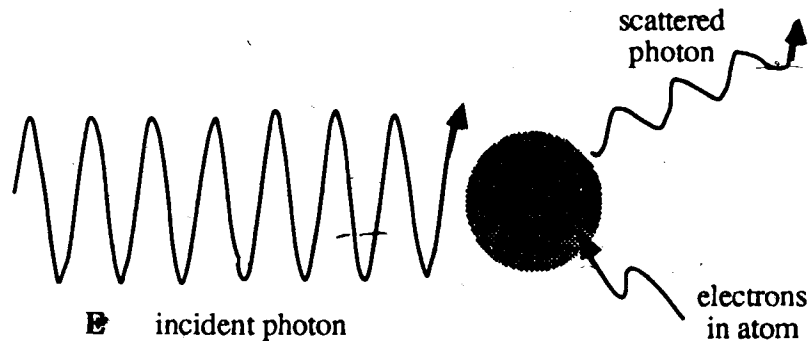
incident photon

Figure 2.3. Rayleigh scattering

2.1.1.4   Compton Scattering

The scattering of an incident photon by a "virtually free" electron is called Compton

scattering (Figure 2.4). This mechanism is inelastic since some small amount of energy is

required to overcome the binding energy of the scattering electron, and it is incoherent

because "virtually free" electrons scatter independently of each other. This process

accounts for about 90% of all energy transferred by incident photons interacting in water in

the energy range of 0.1 to 5 MeV. This interaction is studied in detail here because it will

help us interpret the convolution kernels in Chapter 3.
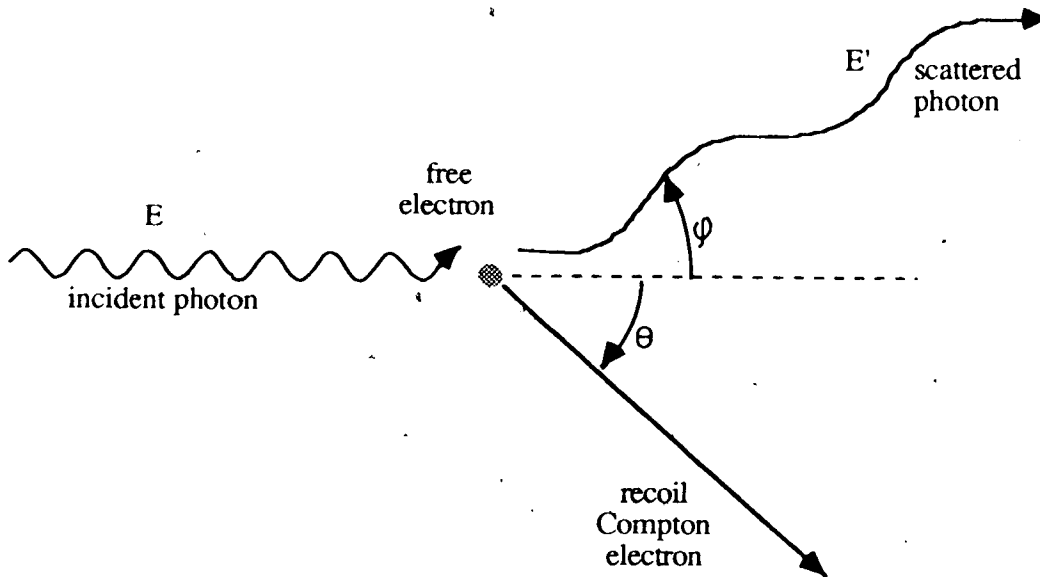
Figure 2.4. The Compton Interaction

The most fundamental interaction coefficient, the *electronic cross section* , $_e\sigma_c$, describes the probability of a Compton interaction with an electron. The differential electronic cross section for the probability of a *photon being scattered* into a unit solid angle (Ω) about angle φ has been calculated by Klein and Nishina from quantum mechanical principles (Heitler 1954). These cross sections are stated in equation 2.14 and have been tabulated by various authors (Hubbell 1969, Nelms 1953).

$$\frac{d_e\sigma_c}{d\Omega} = \frac{r_0^2}{2} \left[\frac{1}{1 + \alpha(1-\cos\varphi)} \right]^2 \times \left[1 + \cos^2\varphi + \frac{\alpha^2(1-\cos\varphi)^2}{1 + \alpha(1-\cos\varphi)} \right]$$

(2.14)

where

$d_e\sigma_c/d\Omega$ is the differential cross section per electron for scattering a photon of frequency v, with a deflection φ into a solid angle $d\Omega$

$r_0^2 = (e^2/m_0c^2)^2 = 7.94 \times 10^{-26} \text{cm}^2$ is the electron classical radius squared

$\alpha = E_0/m_0c^2$ is the incident photon energy in units of electron rest mass

The *total electronic cross section* can be found by integrating over all scattering angles, yielding the probability of scattering at any angle.

$$e^{\sigma}c = 2\pi r_0 \left\{ \frac{1+\alpha}{\alpha^2} \left[\frac{2(1+\alpha)}{1+2\alpha} - \frac{\ln(1+2\alpha)}{\alpha} \right] \right.$$

$$\left. + \left[\frac{\ln(1+2\alpha)}{2\alpha} - \frac{1+3\alpha}{(1+2\alpha)^2} \right] \right\} \qquad (2.15)$$

The cross section representing the *energy scattered* can be obtained by weighting the *total cross section* with the fractional energy carried off by the scattered photon, $(1 + \alpha(1-\cos\varphi))^{-1}$. This is given below

$$\frac{d_e\sigma_s}{d\Omega} = \frac{r_0^2}{2} \left[\frac{1}{1 + \alpha(1-\cos\varphi)} \right]^3 X \left[1 + \cos^2\varphi + \frac{\alpha^2(1-\cos\varphi)^2}{1 + \alpha(1-\cos\varphi)} \right].$$

$$(2.16)$$

The total *energy scattering* cross section is

$$e^{\sigma}s = 2\pi r_0 \left[\frac{4\alpha^2}{3(1+2\alpha)^3} - \frac{(1+2\alpha)}{\alpha^2(1+2\alpha)^2}(1+2\alpha-2\alpha^2) + \frac{1}{2\alpha^3}\ln(1+2\alpha) \right]$$

$$(2.17)$$

The Compton electronic *energy transfer* cross section is the average fractional energy loss of the incident photon and is obtained by subtraction

$$e^{\sigma}tr = e^{\sigma}c - e^{\sigma}s \qquad (2.18)$$

The Compton electronic energy transfer can alternately be considered as the energy gain of the recoil electron:

$$_e\sigma_{tr} = \sigma_c \ (E_e/E_0) \qquad\qquad (2.19)$$
where
E_e is the average energy of the Compton recoil electron

Figure 2.5 demonstrates the relative importance of $_e\sigma_c$, $_e\sigma_s$, and $_e\sigma_{tr}$ as a function of photon energy. Figure 2.6 shows the angular distribution of the number of Compton recoil electrons for different incident photon energies.
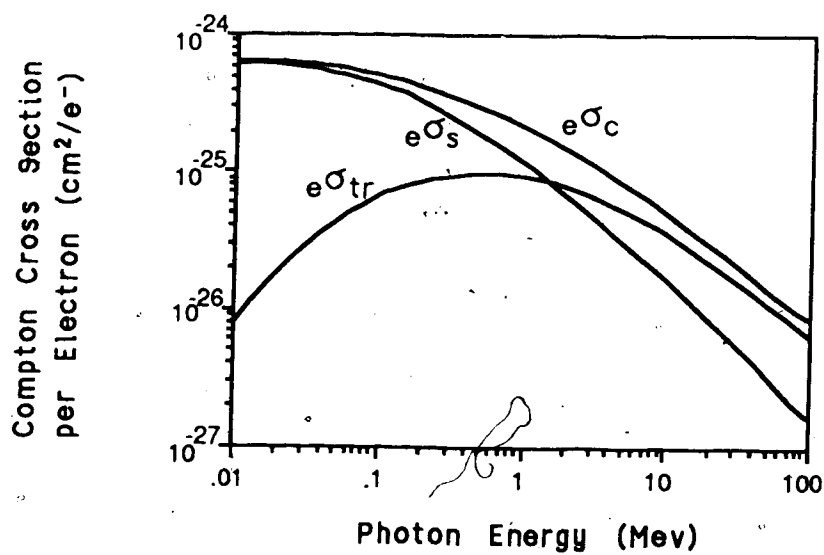
Figure 2.5. The total electronic Compton coefficient ($_e\sigma_c$), the Compton scatter coefficient ($_e\sigma_s$), and the Compton transfer coefficient ($_e\sigma_{tr}$) for a free electron plotted against incident photon energy.
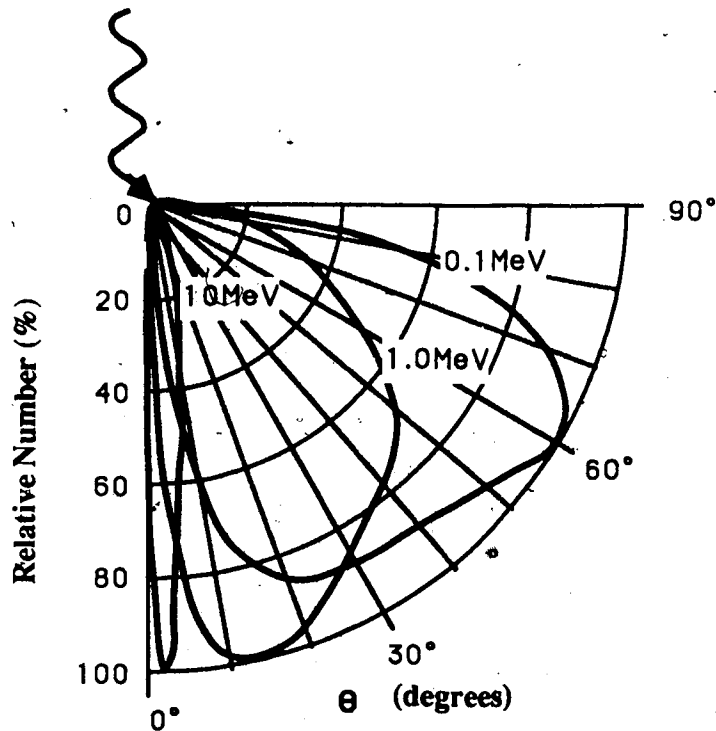
Figure 2.6. Angular distribution of the number of Compton recoil electrons per unit interval of angle.

2.1.1.5 Pair Production

Photons with energy in excess of 1.02 MeV may be absorbed in the neighbourhood of an atomic nucleus and produce an electron-positron pair (Figure 2.7). The positron is eventually annihilated by recombination with an electron of the absorbing medium, yielding a pair of photons (see §2.1.2.2). Pair production becomes the dominant interaction (>50%) in water for incident photon energies above about 30 MeV.

The atomic cross section for pair production, varies proportionally to Z^2 and varies approximately as $\log(E_0)$ (Attix 1986). Again since N_A/Z is fairly constant, the mass attenuation coefficient varies proportionally to Z and roughly as $\log(E_0)$.

The mass transfer coefficient is given by

$$\kappa_{tr}/\rho = \kappa/\rho \ (1-2m_0c^2/E_0) \qquad\qquad [cm^2/g] \qquad (2.20)$$

where

m_0c^2 is the rest mass of the electron (0.511 MeV).

The mass energy absorption coefficient is given by:

$$\kappa_{ab}/\rho = \kappa_{tr}/\rho \ (1-g) \qquad\qquad .[cm^2/g] \qquad (2.21)$$

where

g is the percentage of the transferred energy emitted as
    bremsstrahlung radiation by either the electron or positron.
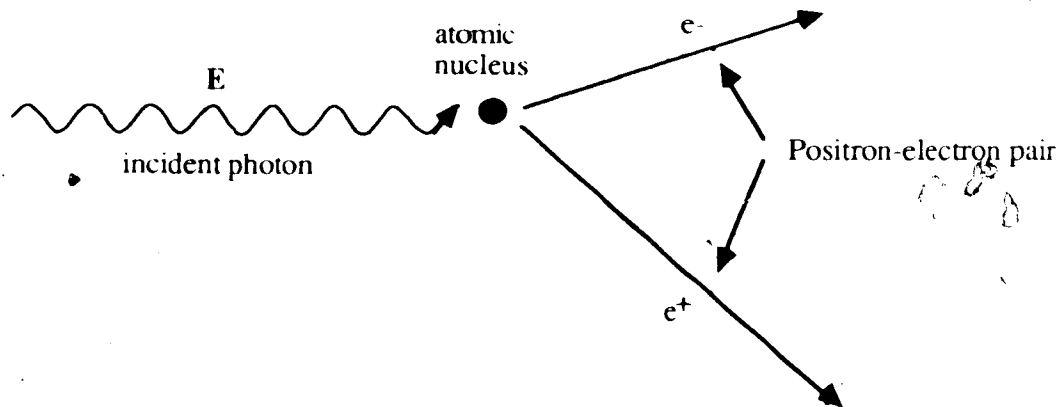
Figure 2.7. Pair Production

2.1.1.6 Comparison of the Cross Sections

Table 2.2 summarizes energy absorption and scattering coefficients for each of the interaction mechanisms.

	Transferred energy	Scattered energy	comment
τ	$\tau_{tr}/\tau = 1-\delta/E_0$	$\tau_s/\tau = \delta/E_0$	$\tau \approx \tau_a$
σ	$\sigma_{tr}/\sigma_c = E_e/E_0...$	$\sigma_s/\sigma_c = ...$	$\sigma_c = \sigma_{tr} + \sigma_s$
σ_{coh}	$\sigma_{tr}/\sigma_{coh}=0$	$\sigma_s/\sigma_{coh}=1$	ignore: elastic small angle
κ	$\kappa_{tr}/\kappa = 1-2mc^2/E_0$	$\kappa_s/\kappa = 2mc^2/E_0$	$\kappa \approx \kappa_a$

Table 2.2. A comparison of the energy transfer and energy scatter coefficients.

Figure 2.8 demonstrates the iso-importance of the three major interaction mechanisms as a function of photon energy and atomic number. For example, for a photon energy of 0.1 MeV the photoelectric and Compton effects are equal for an atomic number of 23. For larger Z, the photoelectric effect is dominant and for smaller Z the Compton effect is dominant. For a fixed Z (water, bone, and lead are shown on Figure 2.8), a more detailed examination of the interaction cross sections is possible. In this work, we restrict our attention to water equivalent material where the Compton effect is dominant for the energy range of 35 keV to 30 MeV. However, it should be noted, that for lead the Compton effect is dominant only for the energy range of 600 keV to 5 MeV.
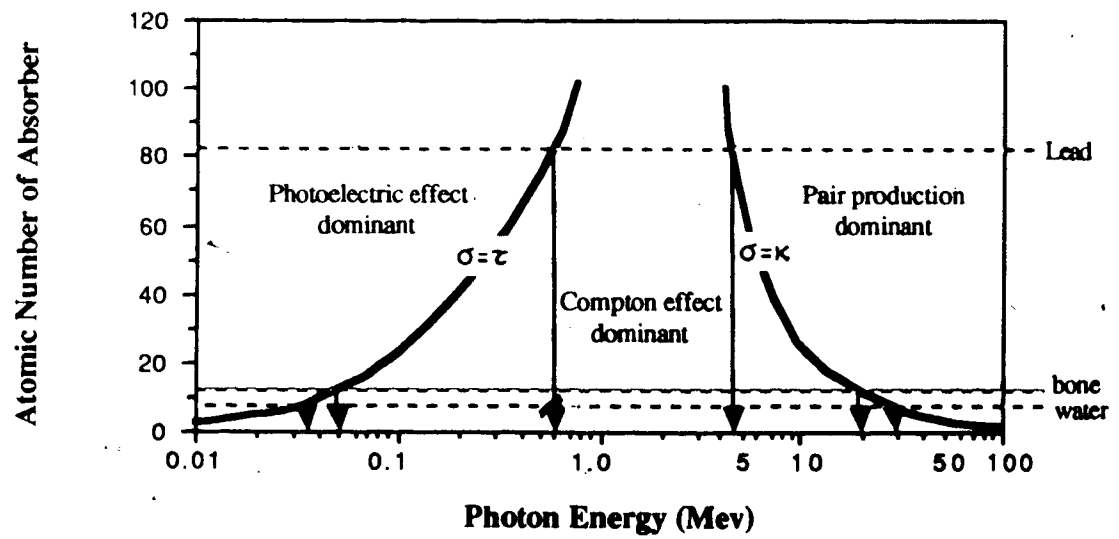
Figure 2.8. Relative importance of σ, τ, and κ as a function of energy and Z

Figure 2.9 shows the relative importance of the major photon interactions occurring in water. The relative importance is measured in two ways: one as a percentage of the total

number of interactions and alternately as a percentage of the total energy transferred. We see that in water, Compton interactions account for 90% of the energy transfer to electrons in water for the energy range of 0.10 to 5.0 MeV.

Incident Photon Energy (MeV)

Legend (top graph):
- Rayleigh
- Compton
- Photoelectric
- Pair Production

Incident Photon Energy (MeV)

Legend (bottom graph):
- Compton
- Photoelectric
- Pair Production
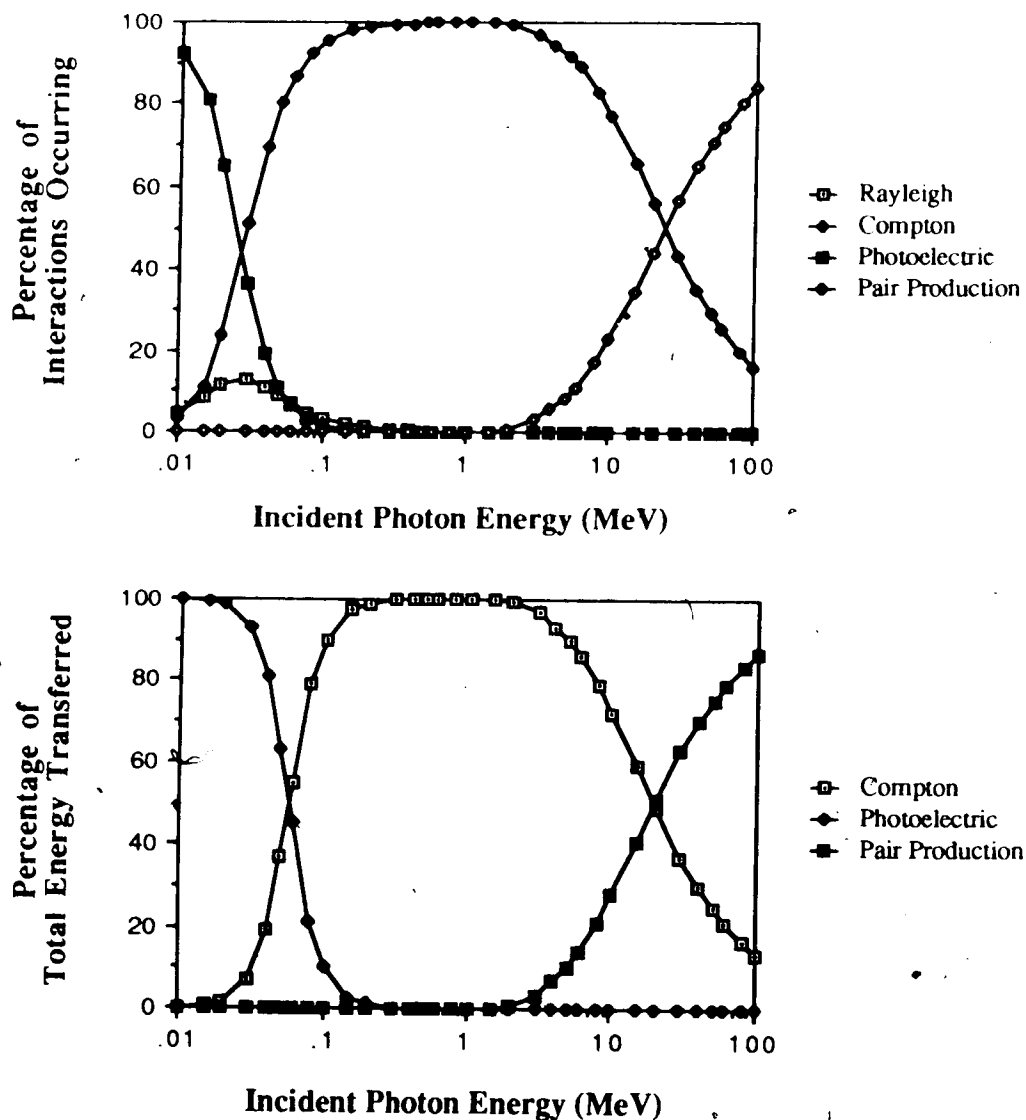
Figure 2.9. Relative importance of σ, τ, **and** κ **as a function of energy in water**
a) Percentage of photons interacting in water as a function of energy
b) Percentage of energy transferred in water as a function of energy

2.1.2 Charged Particle Interactions

The interactions of charged particles set-in-motion (electrons and positrons) by incident photons are of primary importance in X and γ radiation dosimetry since these particles are the direct depositors of energy. Charged particles experience Coulomb interactions; and positrons, since they are antimatter, eventually experience an annihilation process. These interactions will now be briefly discussed.

2.1.2.1 Coulomb Interactions

Charged particles can undergo both elastic and inelastic Coulomb interactions. Inelastic interactions are those for which the incoming particle loses energy resulting in atomic ionization or excitation; while elastic interactions simply redirect the incoming particle with kinetic energy conservation. These Coulomb interactions may occur with the electrostatic field of the atom as a whole, individual atomic electrons, or the nucleus itself. The electrostatic field that the incoming charged particle mainly interacts with, can be determined according to the impact parameter, b, and the atomic radius, a, as illustrated in Figure 2.10.
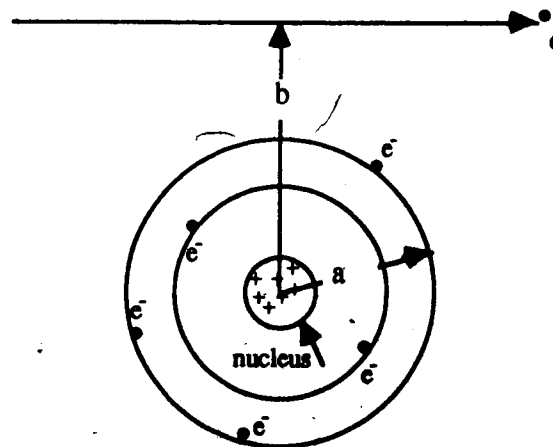
Figure 2.10. The impact parameter and atomic radius.

At a great distance from the atom (b»a), the Coulomb field of the charged particle "feels" the atom as a whole, with the net result of transferring a little energy (≈eV) to the atom. Since these distant interactions are more probable than "near hits" with individual atoms, these "soft" interactions occur the most frequently and account for roughly half the energy transferred to the medium (Attix 1986).

As the impact parameter approaches the atomic radius (b≈a), the charged particle will be chiefly interacting with an atomic electron. In these "hard" collisions, the incoming particle transfers a significant fraction of its incident energy to an atomic electron and "knocks" it from the atom. These electrons (called δ-rays) also undergo Coulomb interactions depositing energy along a track separate from the primary charged particle (see Figure 2.11). Although hard collisions are not as numerous as soft collisions, the fraction of the incident energy of the primary particle transferred through hard collisions to the medium is generally comparable to the fraction of energy transferred through soft collisions (Attix 1986).

After experiencing the previous two interactions, the charged particle may also penetrate the atom (b«a), and interact with the electrostatic field of the nucleus. In 97-98% of all such interactions, the particle scatters *elastically* and does not excite the nucleus or radiate energy. This mechanism has a high probability for occurrence with electrons in the Mev range, and is largely responsible for the tortuous path followed by the electron. The remaining 2-3% of the interactions result in significant energy loss and the emission of Bremsstrahlung (braking radiation) radiation. While this interaction is responsible for energy loss of the incident particle, it does not directly result in ionization or excitation of the atom (Attix 1986, Nahum 1985). Bremsstrahlung radiation is relatively unimportant in tissue-like materials for electrons (and positrons) below 10 MeV.
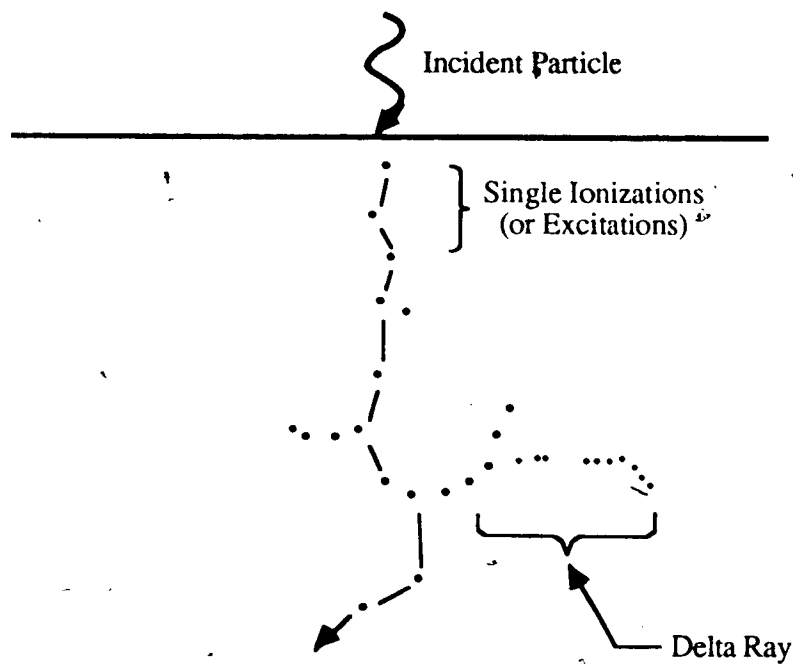
Figure 2.11. Electron tracks.

2.1.2.2   Positron Annihilation

Positrons experience the same Coulomb interactions as do electrons. However, since positrons are antiparticles, they will eventually be captured by an electron in the medium and be annihilated. This annihilation process is more probable for low energy positrons and results in the production of two photons. If the positron and electron are both at rest when they undergo annihilation, then two photons will be produced each with 0.511 MeV and travelling in opposite directions (as illustrated in Figure 2.12).
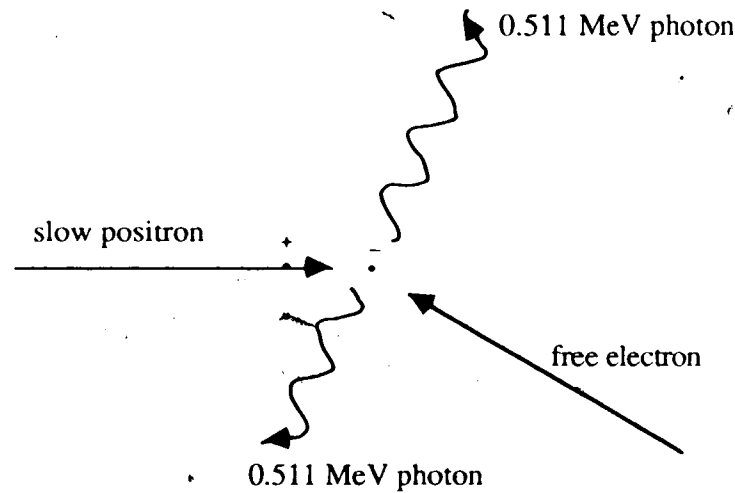
Figure 2.12. Kinematics of positron annihilation.

2.1.2.3   Stopping Power

The large number of small energy losses due to "soft" collisions has lead to the "continuous slowing down approximation" (CSDA). The average energy loss per unit path length is represented by the *linear stopping power* . In analogy with the mass attenuation coefficient for photon interactions, there is a corresponding mass stopping power. The stopping power can also be separated into two components; the collision stopping power and the radiative (or bremsstrahlung) component (equation 2.22). These will be briefly described.

$$\left[\frac{dE}{dl} \right]_{tot} = \left[\frac{dE}{dl} \right]_{col} + \left[\frac{dE}{dl} \right]_{rad} \qquad [MeV/cm] \qquad (2.22)$$

where

$(dE/dl)_{tot}$ is the total linear stopping power representing the total energy lost by a charged particle in traversing a distance dl in material of density ρ

$(dE/dl)_{col}$ is the linear collision stopping power representing the average energy lost by a charged particle in traversing a distance dl due to "soft" and "hard" collisions

$(dE/dl)_{rad}$ is the linear radiative stopping power representing the average energy lost by a charged particle in traversing a distance dl due to bremsstrahlung events with the atomic nucleus

In summary, Figure 2.13 shows the mass collision stopping power for water as a function of electron kinetic energy. For example, an electron with a kinetic energy of 10 MeV has a collision stopping power of about 2.0 MeV cm^2/g (2.0 MeV/cm) in water (ICRU 28).
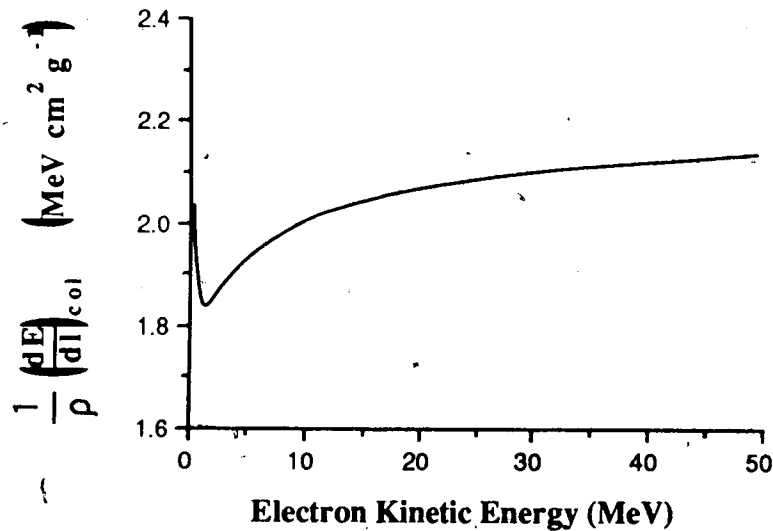
Figure 2.13. Energy dependence of the collision stopping power in water.

Figure 2.14 show the radiative stopping power as a function of electron kinetic energy. The relative importance of the radiative stopping power to the collision stopping power is given approximately by equation 2.23 and is plotted in Figure 2.15 for various media.

$$\frac{S_{rad}}{S_{col}} \approx \frac{E Z}{800} \tag{2.23}$$

where

E is the electron energy (MeV)
Z is the atomic number of the medium
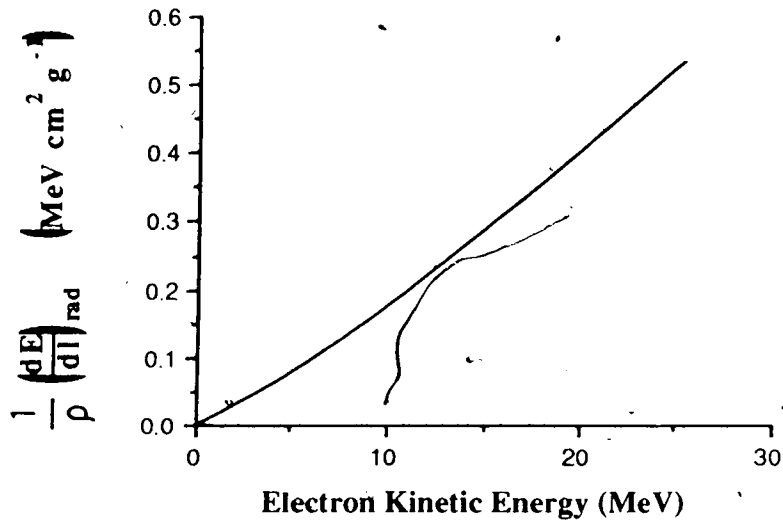
Figure 2.14. Energy dependence of the radiative stopping power in water.
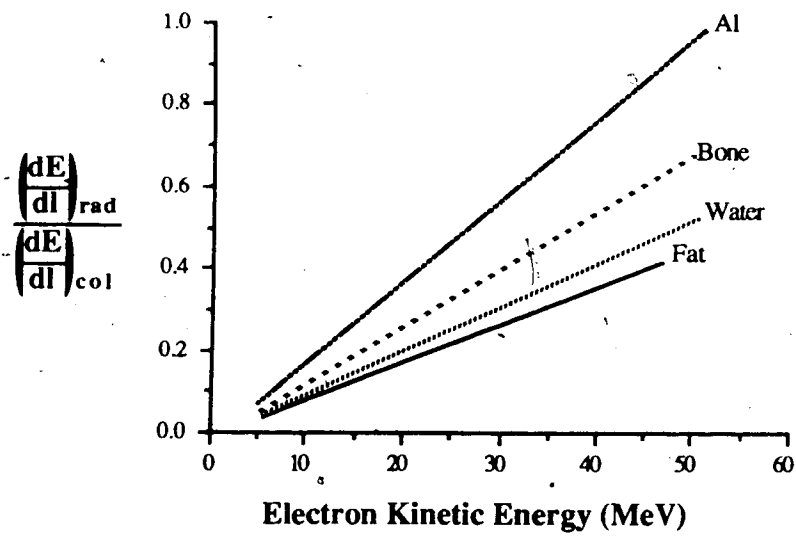
Figure 2.15. Relative importance of radiative losses compared with collision losses in different materials.

2.1.2.4   Linear Energy Transfer

The second interaction coefficient used to quantify energy loss is the linear energy transfer (LET) or restricted linear collision stopping power ,L_Δ.

$$L_\Delta = \left[\frac{dE}{dl} \right]_\Delta \qquad \text{[MeV/cm]} \qquad (2.24)$$

where

$(dE/dl)_\Delta$ is the energy lost by a charged particle in traversing a distance dl due only to collisions with electrons in which the energy loss is *less* than Δ.

Note the relationship between the collision stopping power and the LET;

$$L_\infty = \left[\frac{dE}{dl} \right] \qquad \text{[MeV/cm]} \qquad (2.25)$$

L_∞ "counts" all collision energy losses, as does the collision stopping power.

Figure 2.16 plots the total stopping power, collision stopping power and linear energy transfer (Δ=10 keV) as a function of electron kinetic energy. In the energy range of interest in this work (up to 30 MeV), the radiative stopping power is relatively unimportant in water.
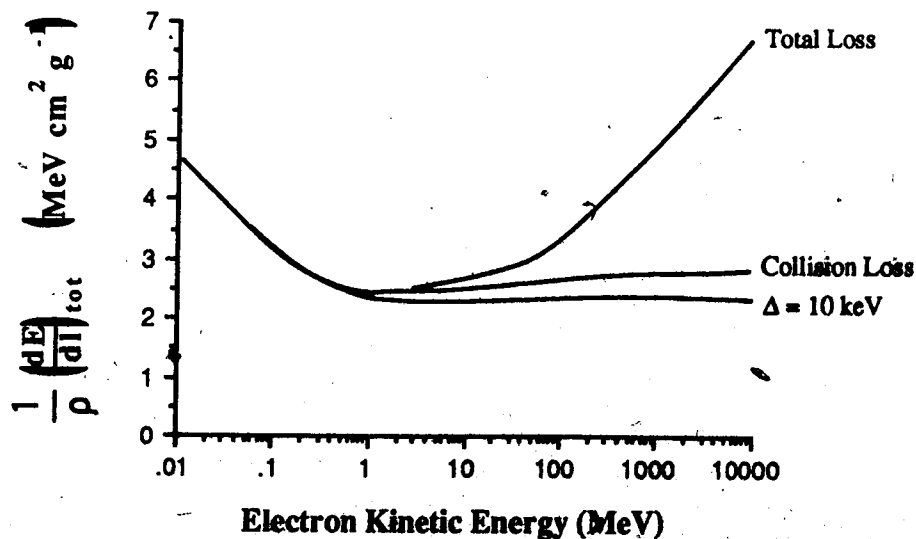
Figure 2.16. The energy dependence of the linear energy transfer function (Δ=10keV), total and collision stopping powers in water.

2.2 Description of Radiation Fields

This section will define and illustrate the terms used to describe a radiation field

(fluence) and the transfer of energy (energy imparted) to an absorbing medium, resulting in

the deposition of absorbed dose.

2.2.1 Fluence

A complete description of a radiation field requires that for all points in space (r),

and at all times (t)[3], the number of particles (N) of type (i), kinetic energy (E), and direction

of motion (Ω) be specified. The function $N(i,E,\Omega; r)$ represents such a quantity.

However, the use of this function is somewhat limited since it will answer the question,

"How many particles are travelling exactly in the direction Ω ?"; but in practice we are more

interested in answering the question "How many particles are travelling in the direction

$\Omega \pm \Delta\Omega$?". Thus, the particle radiance, $P_{i,\Omega}(r)$, is of more use. The particle radiance,

defined below, has the meaning that $P_{i,\Omega}(r)\, d\Omega\, da_{\perp}$ is the expectation value of the

number of particles N of type i traveling in the direction $d\Omega$ around Ω which at the point r

will pass through the area element $da_{\perp}$, as shown in Figure 2.17.

$$P_{i,\Omega}(r) = \frac{d^2N(i,\Omega; r)}{d\Omega\, da_{\perp}} \qquad (2.26)$$

Throughout this work, subscripts on functions will indicate a spectral distribution

of that function with respect to the subscripted variable(s). For example, $P_{i,\Omega}(r)$ is the

spectral distribution of the particle radiance with respect to particle type and direction of

motion. P_{Ω} and $P(\Omega_1,\Omega_2)$ are related by the following equation, depicted in Figure 2.18.

---

[3]We are interested in the dose distribution resulting after a time which is very large compared to the energy

redirection and deposition events. Thus, the time dependence will be ignored hereafter in this discussion.

$$N(\Omega_1, \Omega_2) = \int_{\Omega_1}^{\Omega_2} P_\Omega \, d\Omega \qquad (2.27)$$

This function $P_{i,\Omega}(r)$ is a field quantity which means that it has a value at each point

of space. This is stressed by writing $P_{i,\Omega}(r)$ instead of just $P_{i,\Omega}$.
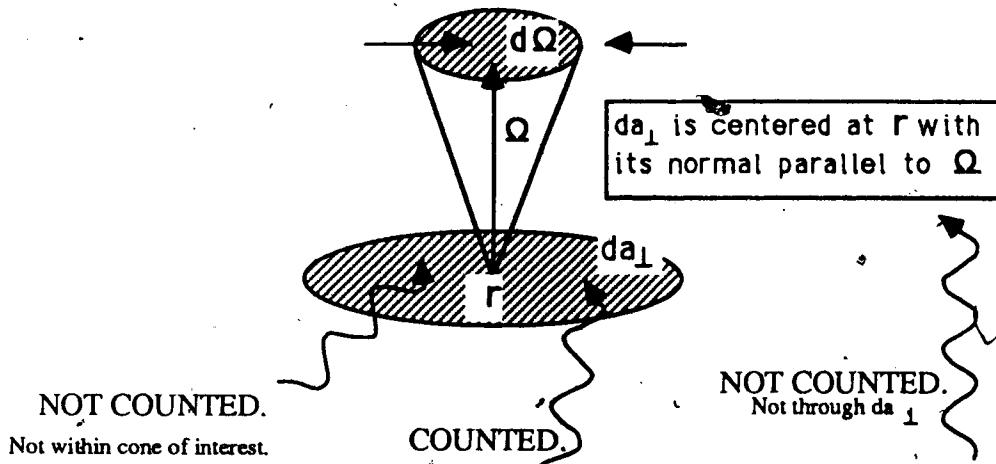
Figure 2.17. Definition of the particle radiance.
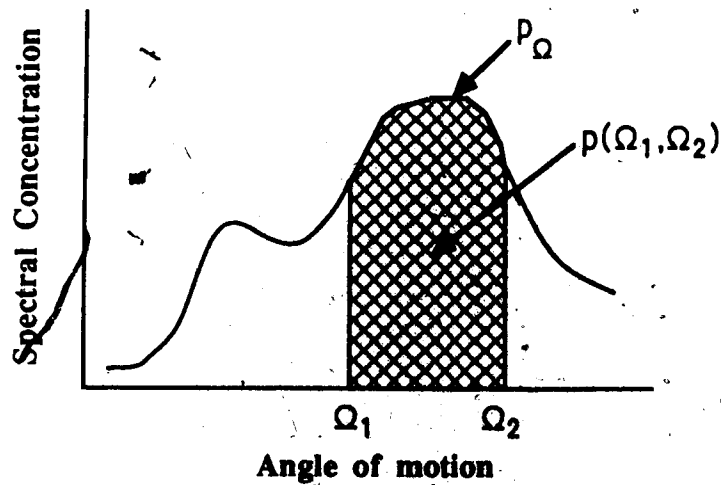
Figure 2.18. Spectral distribution of the incident angle of the particle radiance.

The most fundamental description of a radiation field is P_E, the spectral distribution

with respect to kinetic energy of the particle radiance:

$$P_{i,E,\Omega}(r) = \frac{dP_{i,\Omega}(r)}{dE} = \frac{d^3N(i,E,\Omega \ ;r)}{dE \ d\Omega \ da_\perp} \qquad (2.28)$$

The particle fluence for each particle type is a more common method of describing the average number of particles at a point, irrespective of energy or direction. It is defined below and depicted in Figure 2.19 for particle type, i.

$$\Phi_i(r) = \int_0^{E_{max}} dE \int_{4\pi} d\Omega \ \frac{d^3N(i,E,\Omega \ ; \ r)}{dE \ d\Omega \ da_\perp} \qquad (2.29a)$$

$$= \int_{4\pi} d\Omega \ \frac{d^2N(i,\Omega \ ; \ r)}{d\Omega \ da_\perp} \qquad [cm^{-2}] \qquad (2.29b)$$

Equation 2.29b may be written as follows and interpreted as the number of particles striking a sphere of cross sectional area Δa (see Figure 2.19).

$$\Phi_i(r) = \Delta N(i) \ / \ \Delta a \qquad (2.30)$$

where
        $\Delta N(i)$ is the total number of particles of type i crossing the surface
                of a sphere centered on the point of interest, r
        Δa is the cross sectional area of the sphere
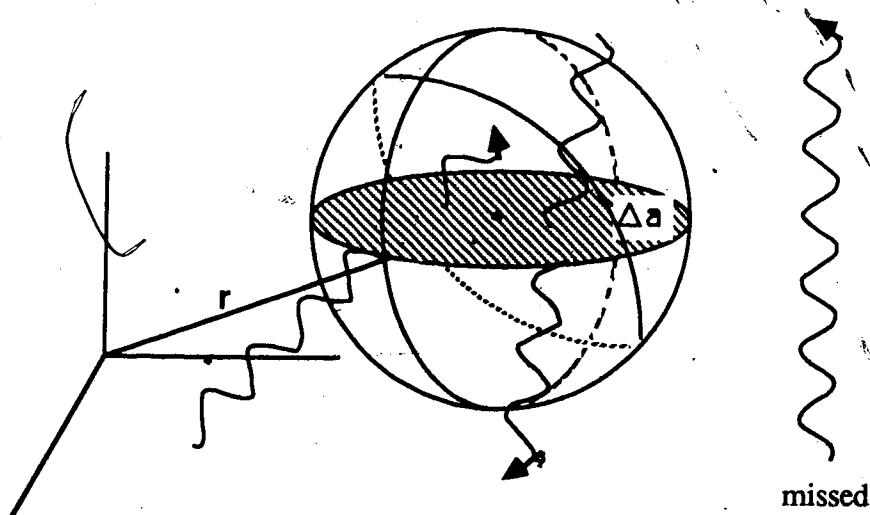
Figure 2.19. Particle fluence. The total number of particles of all directions and energy crossing the surface of sphere centered at r, divided by the cross sectional area of the sphere.

The energy fluence, $\Psi(r)$, is obtained by multiplying $P_E(r)$ by the kinetic energy of each particle and integrating:

$$\Psi(r) = \int_0^{E_{max}} dE \int_{4\pi} d\Omega \; E \; P_{E,\Omega}(r) \qquad [MeV/cm^2] \quad (2.31)$$

The particle fluence and energy fluence previously defined are scalar quantities.

Vector quantities may be similarly established by representing $P_{E,\Omega}(r)$ in a vector form:

$$P_{E,\Omega}(r) = P_{E,\Omega}(r) \; \hat{\Omega} \qquad (2.32)$$

where
$\hat{\Omega}$ is a unit vector in the direction of motion Ω

The vectorial particle fluence and vectorial energy fluence are used in radiation transport theory, which we will discuss briefly in section §2.3 and are given by:

$$\Phi(r) = \int_0^{E_{max}} dE \int_{4\pi} d\Omega \; P_{E,\Omega}(r) \; \hat{\Omega} \qquad [cm^{-2}] \qquad (2.33a)$$

$$\Psi(r) = \int_0^{E_{max}} dE \int_{4\pi} d\Omega \; E \; P_{E,\Omega}(r) \; \hat{\Omega} \qquad [MeV/cm^2] \quad (2.33b)$$

As an example of the difference between the vectorial and scalar fluence, consider two identical particles travelling antiparallel to each other; the vectorial fluence is zero while the scalar fluence is not.

2.2.2   Energy Redistribution

In order to determine the absorbed dose to a point, the average energy deposited in the volume of interest must be known. In section 2.1.1.1 we discussed the mass energy transfer, absorption, and scattering coefficients. These coefficients are based upon the probability of interactions occurring anywhere and are independent of the volume size. At this point, it is important that we make a clear distinction between these concepts. Refer to Attix (1986) for a detailed discussion.

2.2.2.1   Energy Transferred

The energy transferred is the kinetic energy received by charged particles (e.g. electrons and positrons) from uncharged particles (e.g. photons) in the specified finite volume V, regardless of where or how they eventually expend that energy. Kinetic energy transferred among charged particles (e.g. the creation of a δ-ray) is NOT to be included in ε_{tr}. Stated mathematically, we have

$$\varepsilon_{tr} = (E_{in})_\gamma - (E_{out})_\gamma^{non-radiative} + \sum Q \qquad (2.34)$$

where

ε_{tr} is the energy transferred to charged particles in volume V

$(E_{in})_\gamma$ is the energy of uncharged particles entering V

$(E_{out})_\gamma^{non-radiative}$ is the energy of uncharged particles leaving V
- excluding that energy originating from the radiative losses of charged particles while in V (i.e. bremsstrahlung and annihilation events)

$\sum Q$ is the net energy derived from mass-energy conversions in V ($m \rightarrow E$ positive; $E \rightarrow m$ negative)

Positron annihilation results in a rest mass decrease, for which Q is positive. Pair production is an example of rest mass increase, for which Q is negative.

A quantity of interest, closely related to the average energy transferred, is the Kinetic Energy Released per unit MAss (KERMA). It is defined by:

KERMA $= \Psi \ (\mu_{tr}/\rho)$ [MeV/g] (2.35)

where

Ψ is the energy fluence discussed in section 2.2.1

μ_{tr}/ρ is the mass energy transfer coefficient discussed in section 2.1.1.1

2.2.2.2 Energy Absorbed

The amount of energy transferred to electrons which is subsequently absorbed by the medium is described by the energy absorption. The amount of energy absorbed by the medium as a result of the intial interaction in V is given by

$$\varepsilon_{ab} = (E_{in})_\gamma - (E_{out})_\gamma^{non-radiative} - E_\gamma^{radiative} + \sum Q \quad (2.36)$$

$$= \varepsilon_{tr} - E_\gamma^{radiative}$$

where

ε_{ab} is the energy absorbed by the medium

$E_\gamma^{radiative}$ is the energy emitted as radiative losses by charged particles which originate in V, regardless of where the radiative loss occurs.

Note that μ_{ab} is not only dependent on Z at the point of interest (as is μ_{tr}) but also along the entire track length of the electron (since this affects the bremmstrahlung component).

A quantity of interest, closely related to the average energy absorbed, is the Collision KERMA, defined by:

Collision KERMA $= \Psi \ (\mu_{ab}/\rho)$ [MeV/g] (2.37)

where

Ψ is the energy fluence discussed in section 2.2.1

μ_{ab}/ρ is the mass energy absorption coefficient discussed in section 2.1.1.1

2.2.2.3   Energy Deposited

In considering absorbed dose, we are interested in the energy deposited and remaining in the volume of interest. The quantity representing this is the energy deposited, or as its often called, the "energy imparted" (K.R. Kase et.al. 1985, ICRU 33):

$$\epsilon = (E_{in})_\gamma - (E_{out})_\gamma + (E_{in})_{e^\pm} - (E_{out})_{e^\pm} + \sum Q \qquad (2.38)$$

where

ϵ is the energy imparted to matter of mass m in volume V
$(E_{in})_\gamma$ is the energy of all uncharged particles entering V
$(E_{out})_\gamma$ is the energy of all uncharged particles leaving V
$(E_{in})_{e^\pm}$ is the energy of all charged particles entering V
$(E_{out})_{e^\pm}$ is the energy of all charged particles leaving V
$\sum Q$ is the net energy derived from rest mass changes occuring in V
($m \rightarrow E$, Q is positive. $E \rightarrow m$, Q is negative)

In summary, an example will illustrate the distinctions between the energy coefficients. As shown in Figure 2.20, an incident photon of energy E_0 experiences a Compton interaction in the volume of interest and is scattered with energy E_1. An electron is set-in-motion with kinetic energy E_e and within the volume emits a bremsstrahlung photon of energy E_2. Upon leaving the volume, the electron has energy E'_e and subsequently produces another X-ray of energy E_3. For this situation, the energy transferred, the energy absorbed, and the energy deposited within the volume are:

$$
\begin{aligned}
\epsilon_{tr} &= E_0 - E_1 & &= E_e \\
\epsilon_{ab} &= E_0 - (E_1 + E_2 + E_3) & &= E_e - (E_2 + E_3) \\
\epsilon &= E_0 - (E_1 + E_2 + E'_e) & &= E_e - (E_2 + E'_e)
\end{aligned}
\qquad (2.39)
$$
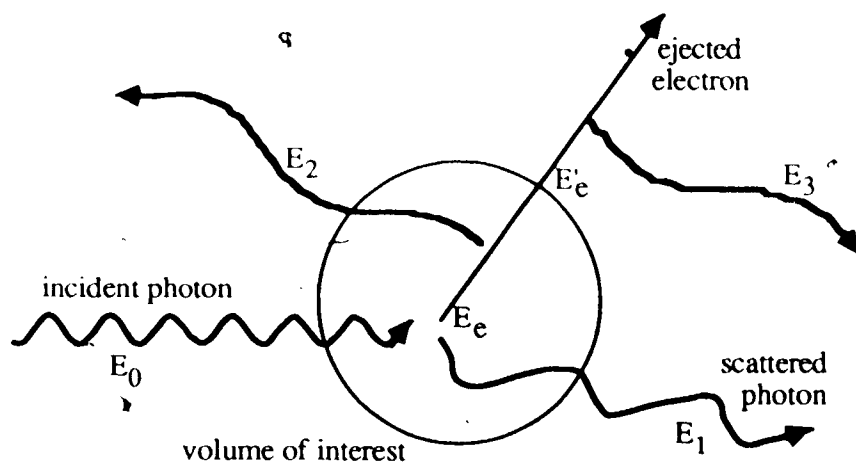
Figure 2.20. Distinction between the energy transferred, absorbed, and deposited for a Compton interaction.

ε is energy deposited and remaining within V by electrons and photons.

ε_{tr} is energy converted from photons to KE of electrons which may or may NOT remain in V (i.e. "knock-on" electrons escaping the volume)

ε_{ab} is energy converted from photons to KE of electrons which remains as KE of electrons (i.e. subtract all radiative losses of electrons originating in V). This energy may or may NOT remain in V. .

In this example, we followed only one interaction. In practice many discrete events contribute to the average energy deposited in a volume.

$$\varepsilon = \sum_{events} \delta\varepsilon_i \qquad (2.40)$$

where

ε is the energy imparted to the matter in the volume of interest

$\delta\varepsilon_i$ is the energy imparted by the discrete event, i, occurring within the volume.

Numerical Monte Carlo techniques can be used to follow the cascade of photons and charged particles which cross a sample volume in order to evaluate equation 2.38. This was done in the generation of "the convolution kernels" discussed in §3.3. Equation 2.38 may also be evaluated analytically as follows.

The net transport of energy through d A into the volume of interest (i.e in the

direction -dA) is the scalar product -dA · Ψ. Integrating the energy fluence vector over

the entire surface of the volume yields the net energy flow (see Figure 2.21);

$$\sum E_{in} - \sum E_{out} = - \oint_{S(V)} \Psi \cdot dA \tag{2.41}$$

Applying the divergence theorem, the surface integral is transformed to a volume integral.

$$\oint_{S(V)} \Psi \cdot dA = \int \int \int \nabla \cdot \Psi \, dV \tag{2.42}$$
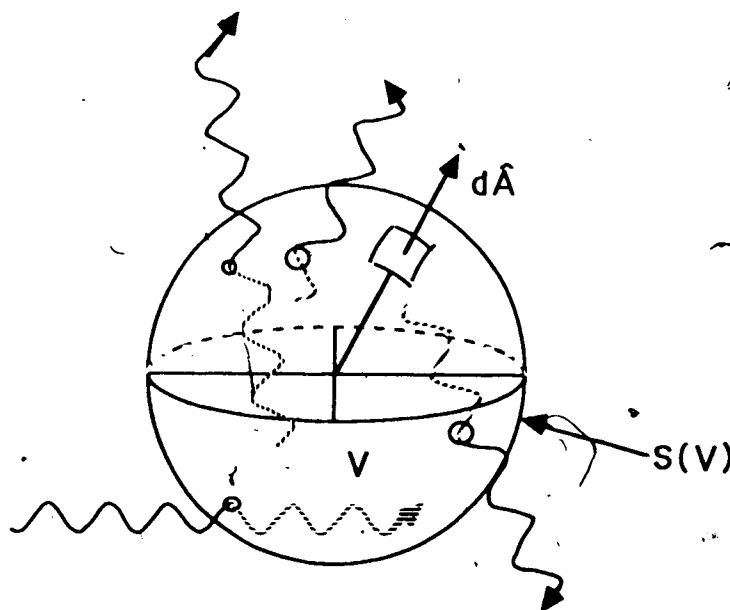
Figure 2.21. Net transport of energy through the volume of interest

Combining equation 2.41 and 2.42 we can write the mean energy imparted to the volume dV as:

$$\epsilon = - \int \int \int \nabla \cdot \Psi \, dV + \sum Q \qquad (2.43a)$$

$$= \int \int \int (-\nabla \cdot \Psi + \frac{d(\sum Q)}{dV}) \, dV \qquad (2.43b)$$

where

$\sum Q$ has been written as the volume integral of $d(\sum Q)/dV$

Thus, the energy imparted to a volume is seen to be the sum of the divergence of the energy vectors, plus (or minus) any changes in rest mass *inside* the volume of interest.

2.2.3 Absorbed Dose

· "Absorbed dose" is related to the biological damage inflicted by ionizing radiation since the ionization triggers a sequence of chemical reactions which upset cell metabolism. All interactions in which energy is deposited in tissue in the form of atomic ionization or excitation, and increases in chemical or crystal lattice energy contribute to absorbed dose, defined as (Carlsson 1982, ICRU 24, ICRU 33):

$$D = \lim_{m \to 0} \left[\frac{\overline{\varepsilon}}{m} \right] \tag{2.44a}$$

$$= \lim_{V \to 0} \left[\frac{1}{\rho} \frac{\overline{\varepsilon}}{V} \right] \tag{2.44b}$$

where:

D is the absorbed dose to a point (1 Gy ≡ 1 J / Kg)
$\overline{\varepsilon}$ is the mean energy imparted to an infinitesimal volume element
  (1 J ≡ 6.2414 x 10^{18} eV ≡ 6.2414 x 10^{11} erg)
m is the mass of the infinitesimal volume element (Kg)
V is the volume of the infinitesimal element (m^3)
ρ is the density of matter in the infinitesimal element (Kg/m^3)

Equation 2.44b shows that in the limiting process of equation 2.44a, we require the density of the matter to remain constant and the volume of matter to approach zero. However, as the volume of matter approaches zero, statistical fluctuations become more prevalent, as illustrated by Figure 2.22. Thus, in order to evaluate equation 2.44a, the following stipulations must be made:

1) $\overline{\varepsilon}$ must be interpreted to mean the expectation value of the energy imparted to the mass

2) the mass must be small enough for the fluence to be uniform within it but large enough to contain many interactions so that statistical fluctuations will be negligible.

ϵ/m

D

Log m
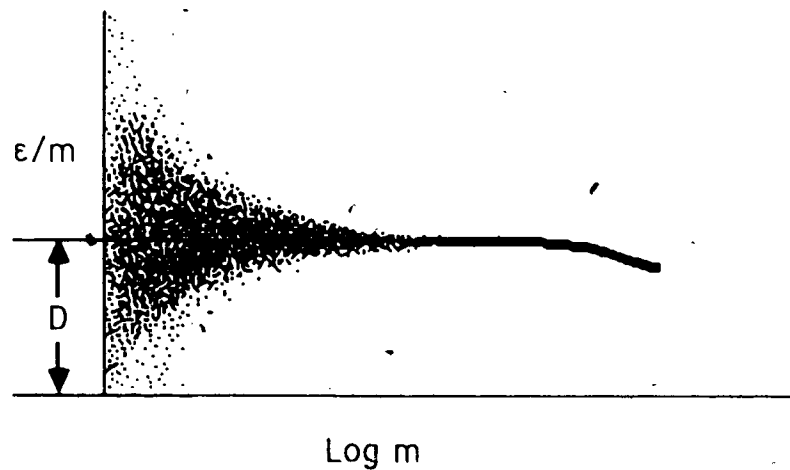
Figure 2.22. Microdosimetry "dose".

Substituting $\bar{\epsilon}$ from equation 2.43b into equation 2.44b, the dose can be written as (Carlsson 1979):

$$D = -\frac{1}{\rho} \nabla \cdot \Psi + \frac{1}{\rho} \frac{d(\Sigma Q)}{dV} \qquad (2.45)$$

Equation 2.45 establishes a connection between radiation transport theory concerned with the motion of particles and radiation dosimetry concerned with the resultant energy deposition. Both radiation transport theory and radiation dosimetry are concerned with interactions in an infinitesimal volume (Rossi and Roesch 1962, Roesch 1968, Spencer 1971). As we shall see, the determination of the energy fluence, Ψ, is very difficult; and the next approach eliminates the need to determine the energy fluence directly.

Carlsson (1979) determines the amount of energy deposited in a volume of interest very simply by summing the number of interactions occuring in the volume and multiplying by the average energy deposited by an interaction. Mathematically : .

$$D = \frac{dN}{dm} \, \overline{\delta\epsilon} \tag{2.46}$$

where

, dN/dm is the total number of interactions taking place per unit mass of the medium

$\overline{\delta\epsilon}$ is the average of the energies imparted by these processes

The total number of basic processes taking place per unit mass of the medium can be determined through interaction cross sections and particle fluences. Contributions to dose may be from both external sources (teletherapy) or internal sources (brachytherapy).

$$\frac{dN}{dm} = \frac{dN_{interactions}}{dm} + \frac{dN_{sources}}{dm} \tag{2.47}$$

where

$$\frac{dN_{interactions}}{dm} = \sum_i \int \Phi_{i,E}(r) \, \frac{\mu_i(E)}{\rho} \, dE$$

$\dfrac{dN_{sources}}{dm}$ is the number of emissions from an internal radiation source.

Combining Equations 2.46 and 2.47 establishes a generalized absorbed dose equation.

$$D(r) = \sum_i \int \Phi_{i,E}(r) \, \frac{\mu_i(E)}{\rho(r)} \, \overline{\delta\epsilon_i}(E) \, dE + \frac{dN_s}{dm} \, \overline{\delta\epsilon_s} \tag{2.48}$$

where

$\Phi_{i,E}(r)$ is the particle fluence, differential in kinetic energy for particle type i

$\mu_i(E)/\rho$ is the total interaction cross section per unit mass for particles of type i and kinetic energy E

$\overline{\delta\epsilon_i}(E)$ is the average value of the energy imparted for interaction processes initiated by particles of type i and kinetic energy E

dN_s/dm is the number of nuclear transformations per unit mass

$\overline{\delta\epsilon_s}$ is the average value of the energy imparted for nuclear transformations (e.g. a radioactive source)

This is a very general statement which can be applied to the determination of absorbed dose for any radiation transport problem including primary radiations which generate a shower of secondary particles. We have already dealt with the determination of $\mu_i(E)$ and $\delta\overline{\epsilon_i}(E)$. Section §2.3 deals with the determination of $\Phi_{i,E}(r)$, and §2.4 examines simplications to the dose calculation problem when situations of radiation equilibrium exist.

2.3 The Transport Equation

In order to compute the absorbed dose using equation 2.48, the particle fluence differential in kinetic energy must be known for all particle types at the "point" of interest. For a primary beam of photons, both photon and electron fluences are required in the general case. Unfortunately, this requires the complex solution of the coupled two particle Boltzmann transport equation for which there appears to be no closed analytic solution for an external beam incident on an arbitrary heterogeneous medium (Fitzgerald et.al. 1967). Under simplifying conditions of radiation equilibrium (discussed in section 2.4), a closed analytic solution may be possible. This section will concentrate on the Boltzmann equation for an arbitrary radiation source and medium.

A transport equation relates the strength of radiation sources, the absorption and scattering properties of the matter present to the quantities that describe the radiation field in the medium. Restricting ourselves to one particle type, the transport equation has been written as follows (Fitzgerald et.al. 1967, Roesch 1968)

$$S(E,\hat{\Omega};r) + \int dE' \int d\hat{\Omega}' \ \Phi_{E',\Omega'}(r) \ \mu_{E,\Omega}(E,\hat{\Omega};E',\hat{\Omega}') = \nabla \cdot \hat{\Omega} \Phi_{E,\Omega}(r) + \mu(E)\Phi_{E,\Omega}(r)$$

$$(2.49)$$

where

$S(r,E,\hat{\Omega})$ is the source term, accounting for the creation of particles

$\Phi_{E,\Omega}(r)$ is the particle fluence differential in kinetic energy and direction

$\mu_{E,\Omega}(E',\hat{\Omega}';E,\hat{\Omega})$ is the cross section for the state transition from $(E',\hat{\Omega}')$ to $(E,\hat{\Omega})$

$\mu(E) = \int dE' \int d\hat{\Omega}' \mu_{E,\Omega}(E',\hat{\Omega}';E,\hat{\Omega})$ total interaction cross section

The Boltzmann transport equation is a particle "bookkeeping" equation. It balances the number of particles entering (LHS) and leaving (RHS) a 6-dimensional "volume" element consisting of 3 spatial coordinates (r), 2 angular coordinates (Ω) and one energy coordinate (E). A particle in this 6-dimensional "volume" element $d\xi = dV \ d\hat{\Omega} \ dE$ is in the spatial volume element dV travelling in the direction $d\hat{\Omega}$ around $\hat{\Omega}$ with energy between

E and E+dE. The number of particles in this element corresponds to the particle fluence, differential in energy and angle: $\Phi_{E,\Omega}(r)$ (see section 2.2.1).

Consider the left hand side of equation 2.49. Two processes can introduce a particle into the volume $d\xi$; a particle may be 'born' in it (e.g. a beta emitter) or a particle may be 'in-scattered' from another volume element. The source term, $S(r,E,\hat{\Omega})$ accounts for the creation of particles in the volume element $d\xi$. The 'in-scattering' term, $\int dE'$ $\int d\hat{\Omega}'\Phi_{E',\Omega'}(r)$ $\mu_{E,\Omega}(E,\hat{\Omega};E',\hat{\Omega}')$, accounts for the scattering from one state $(E', \hat{\Omega}')$ to the state of interest $(E, \hat{\Omega})$.

Now consider the left hand side. Two processes can remove particles from the volume element $d\xi$; spatial divergence out of the volume dV, or a collision that removes the particle from the state $(E, \hat{\Omega})$. The term $\nabla \cdot \hat{\Omega}\,\Phi_{E,\Omega}(r)$ represents the divergence of the particle fluence. The term $\mu(E)\Phi_{E,\Omega}(r)$ represents the number of particles "removed" from the state of interest $(E, \hat{\Omega})$.

As mentioned previously, we require the coupled two particle transport equation since photons (γ) can set electrons (and positrons) in motion, and charged particles can reciprocate by setting photons in motion (e.g. brèmsstrahlung). The addition of a term to account for the transformation from one particle type to another produces the coupled electron-photon transport:

$$\nabla \cdot \hat{\Omega}_1 \Phi_{1,E,\Omega}(r) + \mu(E_1)\Phi_{1,E,\Omega}(r) = S_1(r) + \qquad (2.50a)$$
$$+ \int dE_1 \int d\hat{\Omega}_1{}' \; \Phi_{1,E',\Omega'}(r) \; \mu_{E,\Omega}(E_1,\hat{\Omega}_1;E_1{}',\hat{\Omega}_1{}')$$
$$+ \int dE_2 \int d\hat{\Omega}_2 \; \Phi_{2,E,\Omega}(r) \; \mu_{E,\Omega}(E_1,\hat{\Omega}_1;E_2,\hat{\Omega}_2)$$

$$\nabla \cdot \hat{\Omega}_2 \Phi_{2,E,\Omega}(r) + \mu(E_2)\Phi_{2,E,\Omega}(r) = S_2(r) + \qquad (2.50b)$$
$$+ \int dE_2 \int d\hat{\Omega}_2{}' \; \Phi_{2,E',\Omega'}(r) \; \mu_{E,\Omega}(E_2,\hat{\Omega}_2;E_2{}',\hat{\Omega}_2{}')$$
$$+ \int dE_1 \int d\hat{\Omega}_1 \; \Phi_{1,E,\Omega}(r) \; \mu_{E,\Omega}(E_2,\hat{\Omega}_2;E_1,\hat{\Omega}_1)$$

The subscripts 1 and 2 represent the type of radiation (e.g photons and electrons). $\mu_{E,\Omega}(E_1,\hat{\Omega}_1;E_2,\hat{\Omega}_2)$ is the cross section for the formation of radiation of type 1 having energy E_1 and direction $\hat{\Omega}_1$ from radiation of type 2 having energy E_2 and direction $\hat{\Omega}_2$.

The transport equation for the second particle type is indentical to the first except that the subscripts are reversed. This pair of equations must be solved together for Φ_1 and Φ_2 indicating the coupled nature of the problem.

Now let us return to the simpler case of 1 particle type. The transport equation of 2.49, when integrated along the vector $\hat{\Omega}$, becomes (Attix and Roesch pg 234):

$$\Phi_{E,\Omega}(r) = \int_0^\infty da \; \exp\left\{ \int_0^a \mu(a')da' \right\} \times \left[S(E,\hat{\Omega},r-a\hat{\Omega}) + \right.$$

$$\left. \int dE' \int d\hat{\Omega}' \; \Phi_{E',\Omega}(r-a\hat{\Omega}) \; \mu_{E,\Omega}(E,\hat{\Omega};E',\hat{\Omega}',r-a\hat{\Omega}) \right] \qquad (2.51)$$

where
a is the distance along $\hat{\Omega}$, positive in the $-\hat{\Omega}$ direction

The source term represents radiation of the desired energy and direction emitted by the radiation source along a "ray" in the direction $\hat{\Omega}$ from r. This radiation contributes to $\Phi_{E,\Omega}(r)$ but is attenuated before reaching r. The exponential term "traces" along the "ray" to determine the photon attenuation (hence we have "ray tracing"). Similarly, the contribution from the in-scatter term is attenuated before reaching r.

A few approaches have been taken to solve this problem and will be discussed briefly. Other methods are discussed in a number of references. (Duderstadt and Martin 1979, Fitzgerald et.al. 1967, Attix and Roesch 1968, Kase et.al. 1985)

2.3.1 Solution by Iteration

The transport equation can be solved in an iterative manner by determining the fluence distribution of unscattered (or primary), once scattered, and multiply scattered photons. If the order of scattering is denoted by a subscript, i, then

$$\Phi_{E,\Omega}(r) = \sum_{i=0}^{\infty} \Phi_{i,E,\Omega}(r) \qquad (2.52)$$

The primary fluence arrives unscattered from the sources; so equation 2.51 yields:

$$\Phi_{0,E,\Omega}(r) = \int_0^{\infty} da \ S(E,\hat{\Omega},r-a\hat{\Omega}) \ \exp\left\{-\int_0^a \mu(a')da'\right\} \qquad (2.53)$$

The ith scattered radiation comes from those photons which have that scattered (i-1) times previously; hence for i greater than 0

$$\Phi_{i>0,E,\Omega}(r) = \int_0^{\infty} da \ \exp\left\{\int_0^a -\mu(a')da'\right\} \times$$

$$\left[\int dE' \int d\hat{\Omega}' \ \Phi_{i-1,E',\Omega'}(r-a\hat{\Omega}) \ \mu_{E,\Omega}(E,\hat{\Omega};E',\hat{\Omega}',r-a\hat{\Omega})\right] \qquad (2.54)$$

The calculation of the unscattered (primary) component is not too difficult. The first-scatter component is harder to calculate, but still feasible (Wong et.al. 1981); the higher order components are almost always very difficult to calculate. In dose calculations, the approach of separating the primary and scatter components has been used extensively (Cunningham 1972) although the calculation of ith scatter from $(i-1)^{th}$ scatter has not.

2.3.2 Solution by Green's Function

If we knew $G_{E,\Omega}(r; E',\Omega',r')$, the solution to the transport equation for a unit point source at r' and emitting monoenergetic radiation of energy E' in the direction Ω', then the unique solution for an arbitrary source distribution could be written as (Attix and Roesch 1968, Case 1957)

$$\Phi_{E,\Omega}(r) = \int dE' \int d\Omega' \int dV' \ G_{E,\Omega}(r; E',\Omega',r') \ S(E',\Omega',r') \qquad (2.55)$$

where

$\Phi_{E,\Omega}(r)$ is the particle fluence distribution with respect to particle
    energy and direction

$G_{E,\Omega}(r; E',\Omega',r')$ is the Green's function which describes the particle
    fluence distribution at r resulting from a point source at r' of
    particles with energy E' and direction Ω'

$S(E',\Omega',r')$ is the source term which describes the energy and angular
    spectra of source particles originating at r'.

The Green's function is calculated by making the source term in the Boltzmann equation a monodirectional point source of a specific energy and direction and then solving the Boltzmann transport equation for the specific boundary conditions (i.e. patient). This solution only provides a 'piece' of the complete Green's function; the location, energy and direction of the point source must be varied in order to 'build up' the entire Green's function. This tedious procedure would also need to be repeated for all anticipated phantoms (or patients), which is not currently practical. Approximate means of generating the complete Green's functions for different phantoms are therefore required.

This method does assume that the transport equation can be solved for a point source incident on an arbitrary phantom. Unfortunately, even this problem is very difficult to solve analytically. Monte Carlo methods are currently the only means of solving the particle fluence problem in general.

2.3.3 Solution by Monte Carlo

The Monte Carlo technique (Raeside 1976) is very similar to solving a problem experimentally except that the "experiment" is performed by a computer. This method is based on the use of random sampling (hence the name) to obtain the solution to the transport equation. A simplistic description of this process will now be given.

A photon is initially set in motion in a specific direction and with a specific energy. The photon travels a distance which is selected randomly according to the probability of interaction. Once the interaction distance has been selected, the type of interaction must be determined. Another random number is used to determine whether the interaction was photoelectric, Compton, or pair production based on the probabilities of each type of interaction occurring. Additional decisions will have to be made depending upon the type of interaction. For example, if a Compton interaction occured, then the angle of scattering will have to be determined according to the Klein-Nishina formula. The resulting scattered electron may be put on a 'stack' to be followed later. This process is carried on until the photon is absorbed or leaves the phantom. The first electron on the 'stack' is 'popped' off and followed until it leaves the phantom or 'dies' (by reaching a cut-off energy). When the particle stack becomes empty (i.e. all the secondary particles are followed to completion), a second incident photon is set in motion. This process is repeated until the launching of another photon will not affect the solution to within some acceptable level of statistical uncertainty. (Nelson and Jenkins 1980, Nelson et.al. 1985)

The statistical uncertainty in this result is related to the number of photons used in the simulation:

$$\sigma = \frac{1}{\sqrt{\text{\# of histories}}} \qquad (2.56)$$

Thus if 10^4 particles are scored in an end result, the uncertainty is 1%. However, all histories do not contribute equally to the statistics in each volume element (or "voxel"). In order to arrive at a solution with sufficiently good statistics in all the voxels of a homogeneous medium (highly symmetric), histories in the order of one to ten million incident photons are needed. In situations of poor symmetry (i.e. inhomogenous phantom), the number of incident photons may be orders of magnitude higher. The corresponding computer time required to follow these particles usually varies from hours to even months depending upon the energy of the incident particles, the phantom geometry, the desired statistical accuracy, and the type of computer performing the calculations.

The Monte Carlo approach is the most promising method for solving the coupled photon-electron transport problem, but is currently impractical in routine clinical use due to speed limitations in computer technology.

In conclusion, we can state that the fluence calculation for the coupled photon-electron problem is extremely difficult if not impossible to solve in the general case. Simplications enabled by radiation equilibrium will be discussed in the following section.

2.4 Radiation Equilibrium

As mentioned previously, in order to calculate the absorbed dose we require complete knowledge of the radiation field (i.e. the fluence, differential in energy, for all types of particles). The determination of the particle fluence is a formidable task (§2.3). Under some situations of radiation equilibrium, the requirement of complete knowledge of the radiation field may be relaxed. However, when no radiation equilibrium exists, such as near the interfaces between media, the complete knowledge of the radiation field is still required. This section deals with the simplifications resulting from different forms of radiation equilibrium.

Radiation equilibrium is defined as the condition such that the energy of a specific particle type entering a volume is the same as the energy of the same particle type leaving the volume. This is expressed mathematically as

$$\nabla \cdot \Psi_i = 0 \tag{2.57}$$

where

$\nabla \cdot \Psi_i$ is the divergence of the vectorial energy fluence for particles of type i (see section §2.2.1)

For an incident photon beam, Ψ is made up of two components, Ψ_γ and Ψ_e. Hence we can break radiation equilibrium into two components, charged particle equilibrium ($\nabla \cdot \Psi_e = 0$) and uncharged particle equilibrium ($\nabla \cdot \Psi_\gamma = 0$). Each will be discussed briefly. Charged particle equilibrium has also been decomposed into other forms of equilibrium. The reader should refer to Attix (1986) for more detailed information.

2.4.1 Complete Radiation Equilibrium

For complete radiation equilibrium we have $\nabla \cdot \Psi_i = 0$, and Equation 2.45 yields the dose to a point :

$$D = \frac{1}{\rho} \frac{d(\Sigma Q)}{dV} \qquad\qquad (2.58)$$

In the presence of complete radiation equilibrium, the absorbed dose is simply the net rest mass converted to kinetic energy per unit mass at the point of interest. In a vacuum, $\nabla \cdot \Psi = 0$, $d(\Sigma Q)/dV = 0$, but the absorbed dose is also zero; a situation of little interest. For a non-zero dose, complete radiation equilbrium cannot exist unless $d(\Sigma Q)/dV > 0$. Complete radiation equilibrium may occur for a uniformly distributed radioactive source, but will not occur for an external photon beam, so complete radiation equilibrium is of little interest in this work.

2.4.2 Charged Particle Equilibrium

In contrast to complete radiation equilibrium, charged particle equilibrium (CPE) is of great interest for an external photon beam. Figure 2.23 depicts an external beam of photons irradiating a finite homogeneous medium. CPE is achieved at distances greater than the maximum range of charged particles from all boundaries of the medium if;

1) The mean free path of the incident photons is much larger than the maximum range of the liberated charged particles.

2) The photon attenuation is negligible over the distance of the charged particle range.
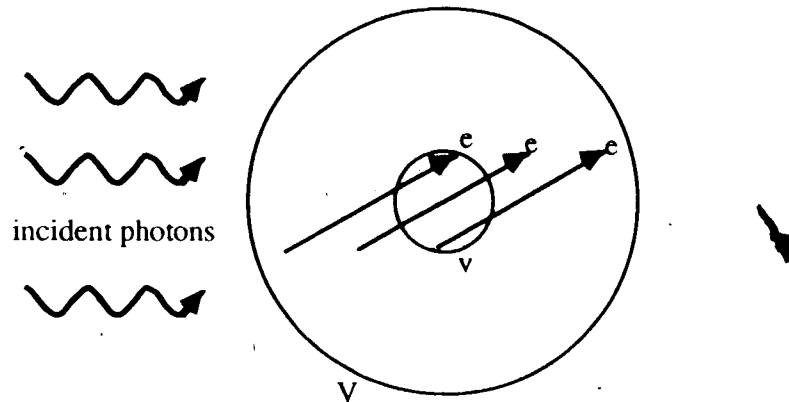
Figure 2.23. Charged particle equilibrium.

Under these conditions, charged particles are introduced uniformly in the small volume v, with the same direction and energy distribution everywhere in the medium V. In this case $(E_{in})_e = (E_{out})_e$, and the energy imparted becomes

$$\varepsilon = (E_{in})_{\gamma} - (E_{out})_{\gamma} + \sum Q \qquad (2.59)$$

Eliminating $\sum Q$ from equations 2.59 and 2.36 yields

$$\varepsilon_{ab} = \varepsilon + (E_{out})_{\gamma} - (E_{out})_{\gamma}^{nonradiative} - E_{\gamma}^{radiative} \qquad (2.60)$$

If the volume is small enough so that all radiative-loss photons escape,.we can assume that any radiative loss experienced by a charged particle after leaving v will be replaced by an identical radiative-loss photon entering v. Thus

$$(E_{out})_{\gamma} = (E_{out})_{\gamma}^{nonradiative} + E_{\gamma}^{radiative} \qquad (2.61)$$

and equation 2.60 reduces to

$$\varepsilon_{ab} = \varepsilon \qquad (2.62)$$

Thus, under conditions of CPE, the energy absorbed is seen to be identical to the energy imparted; and, dose and collision KERMA become identical! This provides a

simpler method for calculating absorbed dose since only the photon energy fluence is required in the KERMA calculation (equation 2.37)!

Under what situations does CPE exist? Let us answer this question by saying when CPE does *not* exist. Failure to reach CPE will result from: inhomogeneities in density or atomic composition, or non-uniformity in the field of indirectly ionizing radiation. Some practical situations where CPE fails to occur include:

- **Close to a Source.** Due to beam divergence, the energy fluence will be much larger on the source side. Thus, more electrons will be set-in-motion nearer to the source.

- **Near Field Boundaries.** Within the maximum electron range of the field edges, there will be a lack of laterally scattered electrons due to the lack of incident indirectly ionizing radiation beyond the field edges.

- **Build-up region.** CPE fails in the charged particle "build-up" region due to a lack of incident charged particles from outside the phantom. The volume of air required to compensate for the missing tissue is prohibitively large (i.e. the entire volume of air would never be irradiated).

- **Under beam modifying devices.** These devices prevent a uniform indirectly ionizing radiation fluence. Hence charged particles are not uniformly liberated and CPE does not exist.

- **Near inhomogeneities.** Inhomogeneities prevent the uniform generation of charged particles due to variations in interaction cross sections with density and atomic number.

- **High Energy Radiation.** As the energy of indirectly ionizing radiation increases, the range of secondary charged particles increases more rapidly than the mean free path of the indirectly ionizing radiation (see Table 2.3). Thus, the same failure occurs as in the case of being close to a source. The

number of charged particles decreases with depth due to the increase in the

attenuation of the indirectly ionizing radiation.

Photon Energy (MeV)	E_{tr} (MeV)	Electron Range (cm)	Photon Attenuation over Electron Range (%)
0.1	0.0148	0.0006	0.01
1.0	0.440	0.148	1.0
10	7.33	3.75	8.0
30	26.1	11.47	17.5

Table 2.3. Photon attenuation over a distance of the maximum range of electron set-in-motion in water as a function of photon energy. Generated from data in Johns and Cunningham (1983)

Thus, CPE fails to exist in many practical situations. In this case, a complete

knowledge of the radiation field is required in order to determine the absorbed dose.

Chapter 3 deals with numerical solutions to the photon beam dose calculation problem.

Chapter 3

Photon Dose Calculations

"I consider that a man's brain originally is like a little empty
attic, and you have to stock it with such furniture as you
choose. ... Now, the skillful workman is very careful indeed
as to what he takes into his brain-attic. He will have nothing
but the tools which may help him in doing his work, but of
these he has a large assortment, and all in the most perfect
order. It is a mistake to think that the little room has elastic
walls and can distend to any extent. Depend upon it, there
comes a time when for every addition of knowledge you
forget something that you knew before. It is of highest
importance, therefore, not to have useless facts elbowing out
the useful ones."

A Study in Scarlet
Sir Arthur Conan Doyle

3.0 Photon Dose Calculations

This chapter begins by specifying the parameters required to fully define the photon dose calculation problem. The most general solution of calculating the dose to a point, $D(r)$, resulting from an arbitrary beam of radiation impinging upon an arbitrary system is then examined. This general solution, is then expressed in a Green's function formalism, which requires the specification of a Green's function (or kernel) and a 'source' function (e.g. particle fluence). Various approximations can be made to reduce the complexity of the fluence calculation but then the kernel calculation becomes more difficult. This compromise between fluence and kernel calculations is briefly discussed. With simplifying assumptions, the Green's function formalism is reduced to a convolution integral. The properties of the convolution integral and kernels are examined in detail.

3.1 Definition of the General Problem

In the most general specification of the dose calculation problem, we have a "radiation field" of arbitrary size, shape, direction, and particle type, incident upon an "irradiated system". The irradiated system is usually considered to be the patient, since the dose distribution there is of primary importance. However, in the more general case, it could also include field flattening filters, collimators, field modifying devices, treatment table, and portal verification detectors, where a knowledge of particle fluence is desireable. We shall say that the irradiated system is comprised of four sub-systems: the field production sub-system, the field shaping sub-system, the patient sub-system, and the verification sub-system (see Figure 3.1).

For now, we restrict our attention to the patient sub-system, but this discussion applies to the entire irradiated system. The parameters affecting the dose calculation can be specified within three groups;

1) specification of the radiation field

Primary collimator

Field flattening filter

Field production sub-system {

Secondary collimator

Field shaping sub-system {

Field modifying device

Patient sub-system

Patient or phantom

Target

Treatment table

Verification detector

Verification sub-system
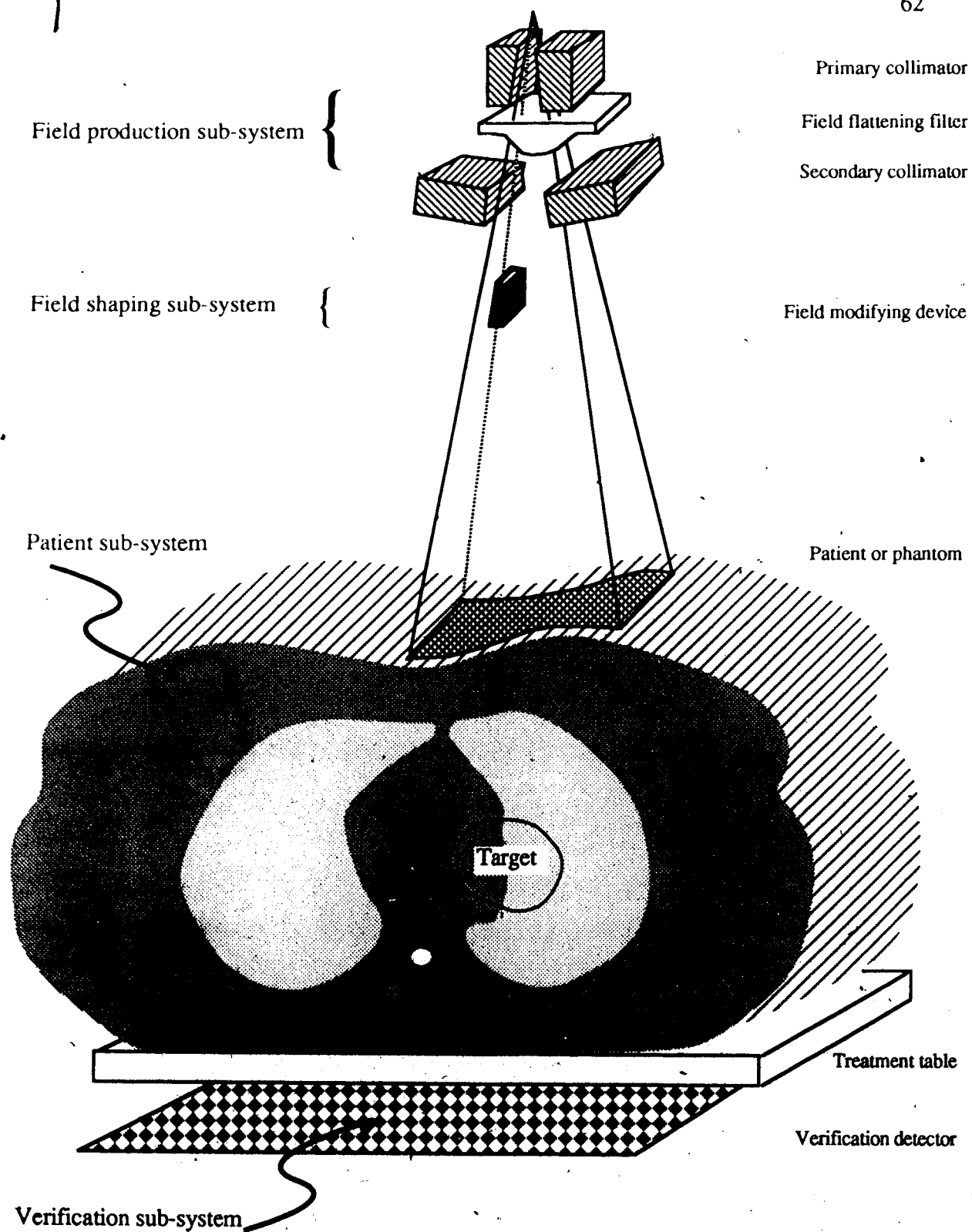
Figure 3.1. Illustration of an irradiated system with four sub-systems and their components.

2) specification of the irradiated system (i.e. patient sub-system)

3) specification of the interactions of radiation with matter (chapter 2).

The dose calculation algorithm must then take these "input" parameters and generate a dose distribution - accurately and quickly.

3.1.1 Parameterization of the Radiation Field

The field of radiation is fully defined by the particle source term, $S_i(E,\hat{\Omega};r)$, which describes the number of particles created at r as a function of energy, angle, and particle type. If internal sources are present (e.g. brachytherapy), this function would be specified throughout the entire irradiated system. However, for an external radiation field, all particles are created outside the irradiated system. These particles are included in the source term by suitable placement on the surface of the irradiated system (e.g. $S_i(E,\hat{\Omega},r_0)$ where r_0 defines the surface of the patient sub-system, see Figure 3.2). The incident particle spectrum (both energy and angle) should accomodate spectral changes resulting from the field production sub-system and the field shaping sub-system. Exogenous photon and electron contaminants from the field production and field shaping sub-systems can thus be modelled through photon and electron source terms[4].

---

[4]For example, one could start with a source term describing the radiation source incident on the field production sub-system and transport these particles through the field production sub-system and onto the field shaping sub-system. The particles emerging from the field shaping sub-system could be further transported onto the patient sub-system, forming the patient sub-system 'source' term, $S(E,\Omega,r_0)$.
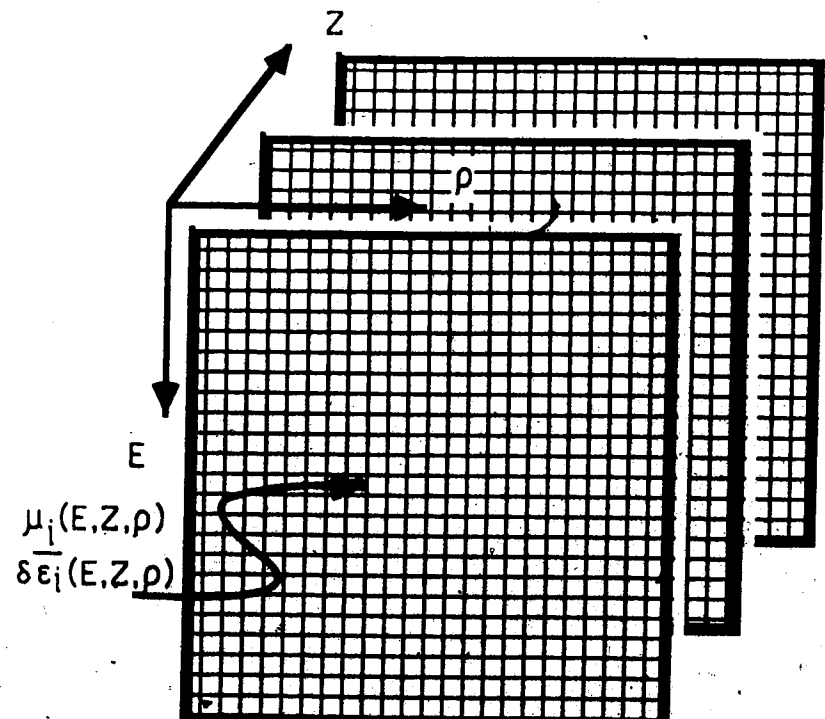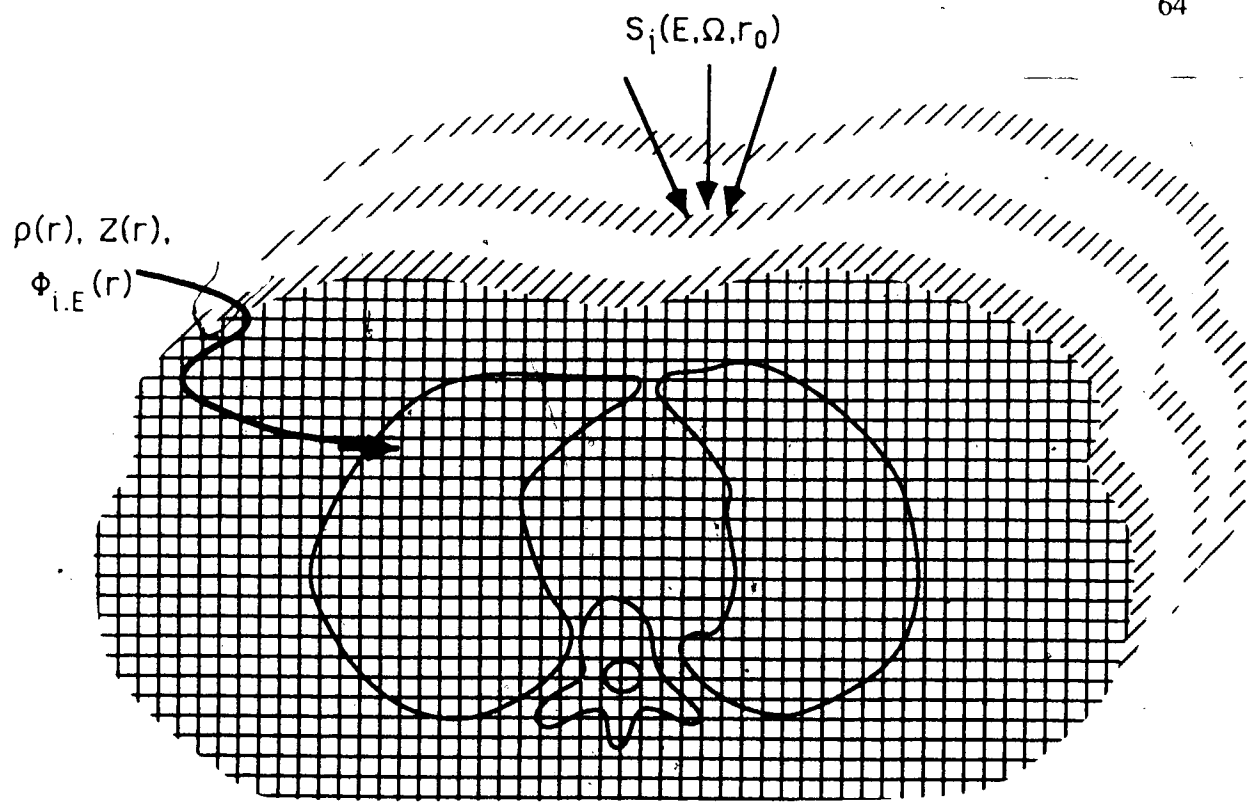
Figure 3.2. The photon dose calculation problem. Parameterization of the radiation field and patient sub-system. Look-up tables for the interaction of radiation with matter.

3.1.2 Parameterization of the Irradiated System

The electron density and (ideally) the atomic number distribution must be specified everywhere within the irradiated system. This specification is most accurately given by one or more three-dimensional (3D) arrays of tissue volume elements (voxels) (see Figure 3.2).

3.1.3 Parameterization of the Interaction of Radiation with Matter

The interaction of radiation with matter has been described fully in Chapter 2. We shall assume that tables containing attenuation coefficients, and the average energy deposited as a function of energy, atomic number, and electron density are available (see Figure 3.2).

3.2 Solutions

The particle source term, irradiated system specification, and interaction coefficients are used together to compute the particle fluence, differential in energy and particle type, $\Phi_{i,E}(r)$, within the irradiated system (see §2.3). The particle fluence can then be used to determine the absorbed dose everywhere in the patient. This last step is especially simplified under conditions of radiation equilibrium (see §2.4).

In order to determine the absorbed dose in the general case for an external photon beam, let us assume a knowledge of the following quantities (depicted in Figure 3.2):

- a description of the particle beam incident on the surface of the irradiated system, $S_i(E,\hat{\Omega};r_0)$, from which we can calculate the particle fluence differential in energy and particle type, $\Phi_{i,E}(r)$

- a 3D voxel description (e.g. a set of CT scans) of the phantom anatomy, $\rho(r)$,

- the interaction cross sections, $\mu_i(E,Z,\rho)$

- the average energy imparted, $\delta\overline{\epsilon}_i(E,Z,\rho)$

Given these quantities, we usually wish to determine the resulting dose 'distribution', consisting of the dose to a number of points - anywhere from 1 point to 64^3 points

3.2.1 The General Solution

In order to develop the convolution method, we begin with the fundamental equation (2.48). Ignoring nuclear transformations, and collecting terms we can rewrite this equation as

$$D(r) = \sum_i \int \Phi_{i,E}(r) \; \frac{\mu_i(E,Z,\rho)\,\delta\overline{\epsilon}_i(E,Z,\rho)}{\rho(r)} \; dE \qquad (3.1a)$$

$$= \sum_i \int \Phi_{i,E}(r) \; G_i(E,Z,\rho;r) \; dE \qquad (3.1b)$$

where

$G_i(E,Z,\rho;r)$ represents the average energy imparted per mass per incident particle of type i at the voxel centered at r

- Figure 3.3 depicts a photon incident on a phantom and its subsequent interactions, labeled 1 to 4. Electron tracks are depicted by a series of dots and dashes. Assuming one incident photon and interactions as depicted, Equation 3.1 could be used to determine the dose distribution as follows.

1. $\Phi_{i,E}(r)$ is calculated knowing $S_i(E,\Omega;r_0)$, and the interaction coefficients, using the transport equation (see §2.3) and would include the photon and electron particles as depicted.

2. $G_i(E,Z,\rho;r)$ is calculated by 'looking up' prestored values for $\mu_i(E,Z,\rho)$, and $\delta\overline{\epsilon}_i(E,Z,\rho)$ and dividing by the density $\rho(r)$ of the local matter. The prestored values of $\delta\overline{\epsilon}_i(E,Z,\rho)$ can be generated with Monte Carlo techniques for the voxel size being used.

3. Equation 3.1 is then evaluated by integrating over the energies and then

    summing the contributions from each particle type striking the voxel.

Unfortunately the first step is very difficult to perform in the general case (see §2.3).

However, there are ways to simplify the fluence calculation and these will be described

next.

3.2.2   Various Green's Function Formalisms

If Equation 3.1b is used to determine the dose to a point, two functions need to be

available: the particle fluence, $\Phi_{i,E}(r)$, and the kernel, $G_i(E,Z,\rho;r)$. The kernel or Green's

function describes how energy is deposited for a unit particle impulse. So far, we have

specified the impulse as being the particle fluence for all particle types. However, if we

restrict the impulse to photons only, the kernel will include the transport of electrons away

from the point of photon interaction. There are other such scenarios possible which

separate the responsibility for transporting particles, as summarized in Table 3.1. These

are now discussed individually.

	Fluence contains the transport of:	Kernel contains $\delta\epsilon$ plus:
3.2.1	all particles	nil
3.2.2.1	all γ (except brem&annih)	$\gamma^{b\&a}$ and $e^\pm$ transport,
3.2.2.2	primary γ	$\gamma^{1,2...}$, $\gamma^{b\&a}$ and $e^\pm$ transport
3.2.2.3	no particles (γ on surface only)	$\gamma^{0,1,2...}$, $\gamma^{b\&a}$ and $e^\pm$ transport

Table 3.1. Separation of particle transport between the fluence and kernel.

$$\text{calculate } \Phi_{i,E}(r) \text{ in all voxels}$$

$$\text{scope of } G_i(E,Z,\rho,r) \longrightarrow \square$$
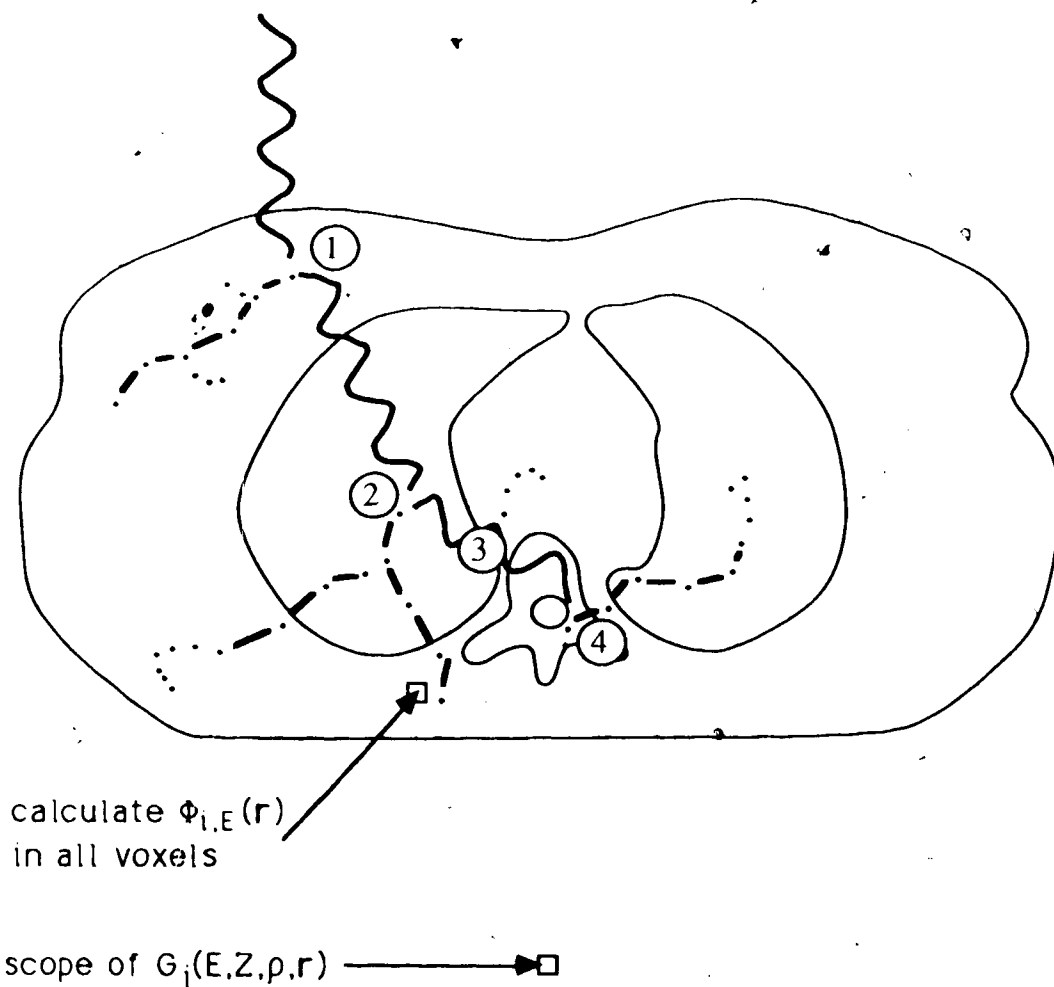
Figure 3.3. Evalution of the geheral absorbed dose equation (3.1).

3.2.2.1   Approach One - fluence transports all photons[5]

As indicated in section §2.3 the calculation of the photon fluence is an order of magnitude simpler that the calculation of an electron fluence. Since electrons are the energy depositing particles, and G_i contains the energy deposited, it is consistent to couple the electron transport in with $G_i(E,Z,\rho;r)$. In order to do this, we need to indicate the point of photon interaction, r', as well as the point at which the energy is deposited, r. We also

---

[5]excluding the transport of bremmstrahlung and annihilation photons

need to stipulate the incident photon direction in order to propogate the electron's deposition of energy correctly. The functions $\Phi_{\gamma,E}(r)$ and $G_i(E,Z,\rho;r)$ thus become functions of Ω, the incident photon direction. $D(r)$ becomes

$$D(r) = \int d\Omega \int dr' \int \Phi_{\gamma,E,\Omega}(r') \quad G_e(E,Z,\rho,\Omega;r,r') \quad dE \qquad (3.2)$$

Note that $\Phi_{\gamma,E,\Omega}(r')$ represents the photon fluence differential in energy and direction at r'. The problem of explicitly determining the electron fluence has been incorporated in the computation of $G_e(E,Z,\rho,\Omega;r,r')$; which is now recognized as a "Green's function". This function describes the imparted energy (at r) as a result of a photon fluence impulse of energy E and particle direction Ω at the point r'. Figure 3.4 illustrates the de-coupled photon transport, $\Phi_{\gamma,E,\Omega}(r')$, and the electron transport and energy deposition, $G_e(E,Z,\rho,\Omega;r,r')$. Each photon interaction has a corresponding electron kernel associated with it. Note that the kernel for each photon interaction has the photon incident from the kernel 'top'.

Bremsstrahlung and annihilation photons bring to light the problem of the 'coupled' nature of photon and electron transport. Should these photons be transported as part of the photon fluence, or should the resulting electrons they release have their imparted energy included in $G_e(E,Z,\rho,\Omega;r,r')$? The latter is easier since the two functions, $\Phi_{\gamma,E,\Omega}$ and G_e, can be treated completely independently. If bremsstrahlung photons are added to the photon fluence then there is 'feedback' between G_e and $\Phi_{\gamma,E,\Omega}$ and they cannot be determined independently, complicating the fluence calculation.

Note that the spatial extent of G_e is larger than for that of Figure 3.3 since the spread of electrons needs to be described. If the electron energy is deposited 'on the spot', then the scope of G_e and G_i would be identical.

calculate $\Phi_{\gamma,E,\Omega}(r')$
in all voxels

①

②

③

④

scope of $G_e(E,Z,\rho,\Omega;r,r')$

①

②

③

④
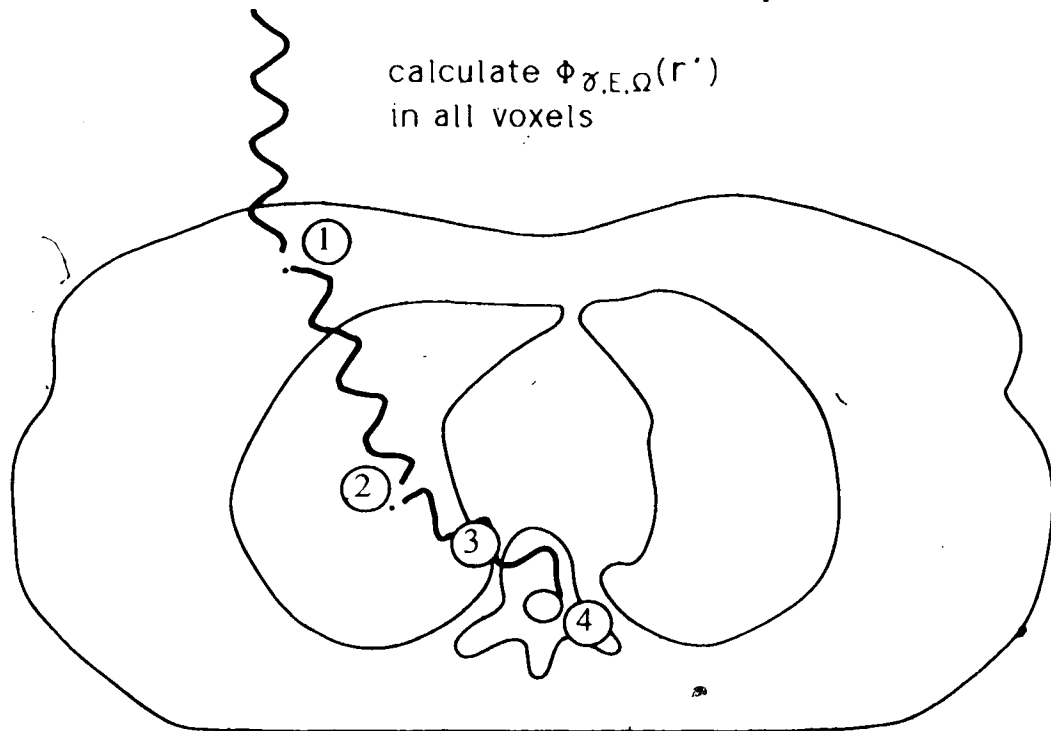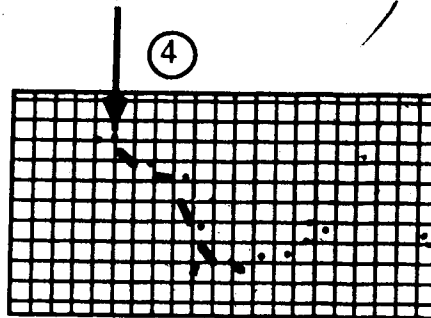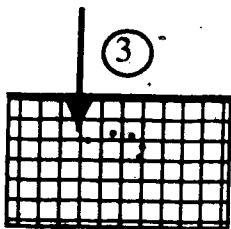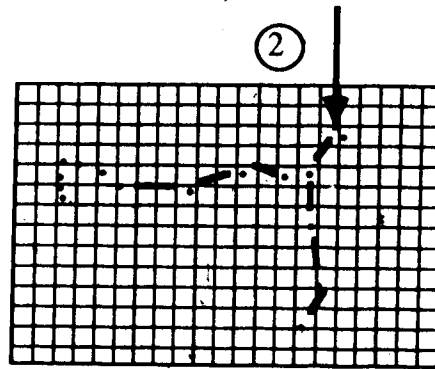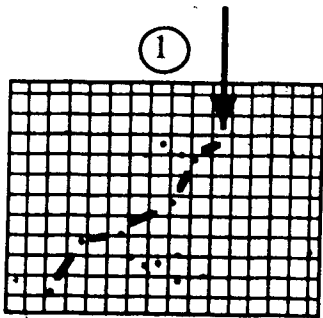
Figure 3.4. Illustration of Approach One

3.2.2.2 Approach Two - fluence transports primary photons only

We can go one step further in simplifying the photon fluence calculation by moving

the transport of secondary photons from the fluence calculation to the kernel calculation.

As a result the kernels must contain the transport of *all* secondary particles. In doing this,

subsequent separation of the transport of photons and electrons becomes impossible. This

approach requires a fluence calculation for only primary photons which can be performed

easily. In this scenario, Equation 3.1 becomes:

$$D(r) = \int d\Omega \int dr' \int \Phi_{\gamma^0,E,\Omega}(r') \quad G_{e\&\gamma>0}(E,Z,\rho,\Omega;r,r') \quad dE \qquad (3.3)$$

This is a "superposition integral" which will be used as the *starting point to develop*

the convolution method. Figure 3.5 depicts the primary photon fluence and the prestored

results of $G_{e\&\gamma>0}(E,Z,\rho,\Omega;r,r')$.

3.2.2.3 Approach Three - fluence does not transport photons

In this approach, the kernel contains the transport of all particles and the subsequent

deposition of energy. The fluence function simply specifies the number of primary

photons striking the surface of the irradiated system. This approach is often called a pencil

beam approach, and is used in electron beam dose calculations. The usefulness in photon

beam calculations is questionable. Figure 3.6 illustrates the contents of the kernel and

fluence functions.

calculate $\Phi_{\gamma^0,E,\Omega}(\mathbf{r}')$
in all voxels

scope of $G_{e\&\gamma>0}(E,Z,\rho,\Omega;\mathbf{r},\mathbf{r}')$
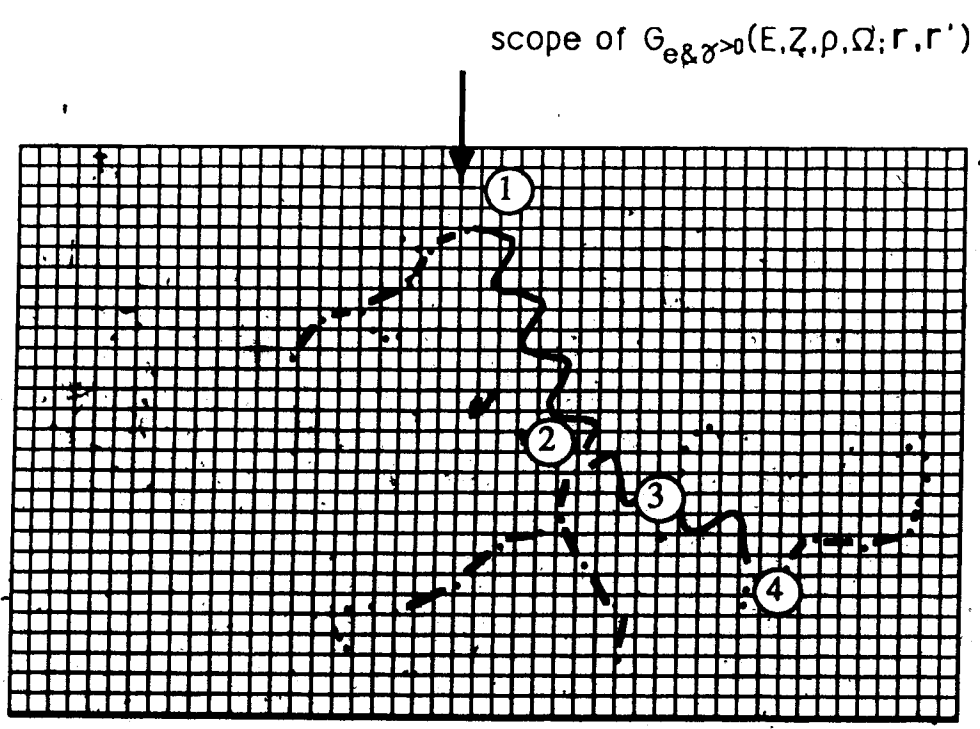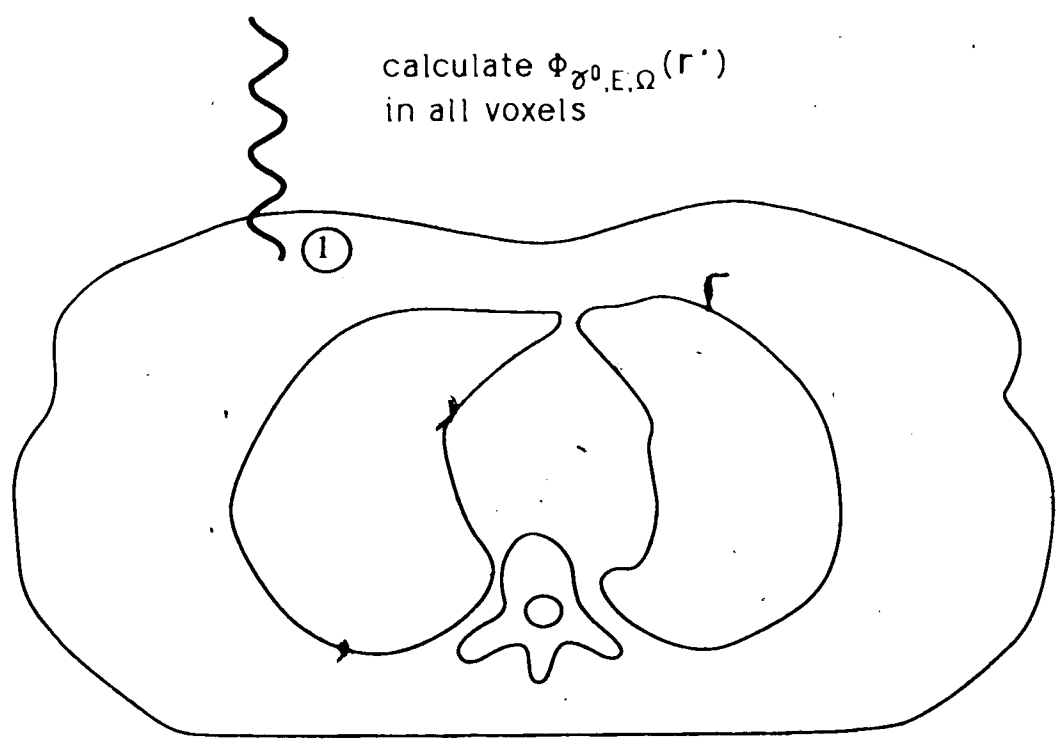
Figure 3.5. Illustration of Approach Two

calculate $\Phi_{\gamma^0,E,\Omega}(r_0)$
on the surface only

scope of $G_{e\&\gamma}(E,Z,\rho,\Omega; r,r)$
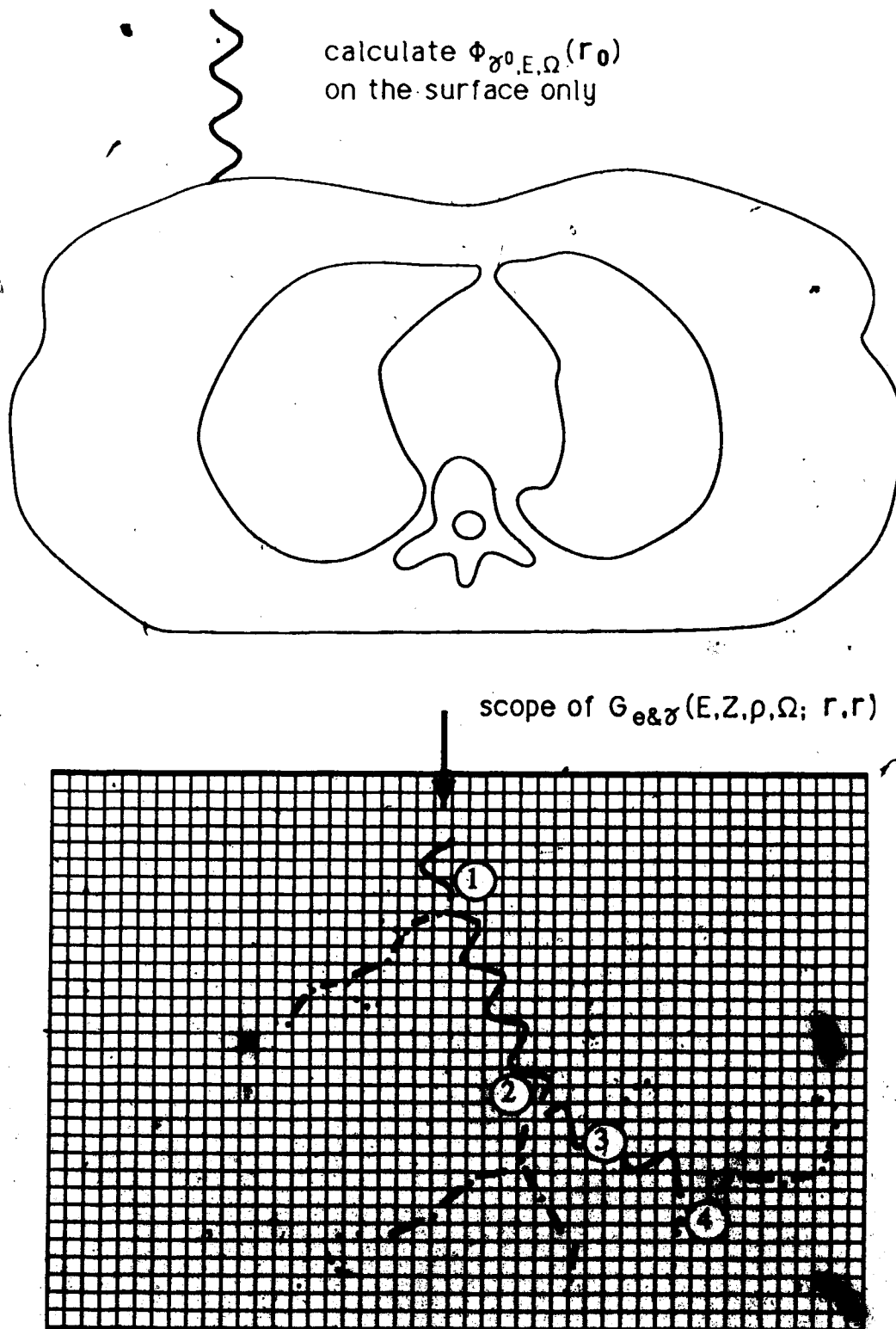
Figure 3.6 Illustration of Approach Three

3.2.3 Other Approaches

The difficulty of the photon dose calculation problem has led to the development of methods which lose sight of the microscopic physics and algorithms which lose sight of the physics altogether! The established semi-empirical methods of calculating dose distributions in homogeneous and inhomogenous media have been documented elsewhere (Van de Geign et.al. 1980, Cunningham 1983). In general, the transport of secondary photons and charged particles is grossly approximated, exogenous photon and electron scatter from beam modifying devices are ignored, and charged particle equilibrium is assumed.

3.2.4 Convolution Formalism

We begin with the superposition integral discussed in section §3.2.2.2. Equation 3.3 may be rewritten by rearranging the order of integration:

$$ D(r) = \int dE \int d\Omega \int dr' \; \Phi_{\sigma^0,E,\Omega}(r') \; G_{e\&\sigma>0}(E,Z,\rho,\Omega;r,r') \qquad (3.4) $$

where

D(r) is the absorbed dose at r

$\Phi_{\sigma^0,E,\Omega}(r')$ is the *primary* photon fluence differential in photon energy and direction at r'

$G_{e\&\sigma>0}(E,Z,\rho,\Omega;r,r')$ is a Green's function representing the electron energy deposited at r due to a primary photon impulse at r'.

r' is the location of the primary photon impulse

r is the location of the energy deposition

E is the incident photon energy

Ω is a unit vector in the incident photon direction

This superposition integral requires that the Green's function $G_{e\&\sigma>0}(E,Z,\rho,\Omega;r,r')$ be known everywhere in the irradiated system for a *primary* photon impulse. The Green's function is dependent upon incident photon spectrum of energy and angle; as well as the atomic number distribution (Z(r')), and electron density distribution($\rho(r')$) within the

phantom. The general photon beam dose calculation problem could be solved by convolving this Green's function with any arbitrary primary photon fluence $\Phi_{\gamma^0,E,\Omega}(r')$.

. Since this general Green's function is spatially variant (i.e. it depends on both r and r') it must be known for every point in the irradiated system. This is currently impractical, because of the large amount of computation time required to generate even a single Green's function for a homogeneous water medium with a high degree of symmetry (see section §3.4). For an inhomogeneous medium with poor symmetry, this computation time would escalate further beyond reason.

The solution is to estimate the spatially variant Green's function from a set of spatially invariant Green's functions. In a homogeneous medium this is reasonable, but requires further study. The following base assumptions are introduced:

1) a mono-energetic photon beam

2) all incident photons travel along a 'ray' from a point source

3) an infinite source to surface distance (SSD)

4) an irradiated system which is homogeneous and water equivalent

5) an irradiated system of infinite size

Assumptions 1, 2 & 3 remove the explicit integration over E and Ω. Assumption 4 removes the dependence on atomic number (Z) and electron density (ρ). Assumptions 3, 4 & 5 ensure the Green's function is *spatially invariant* which means that only the *distance between* the dose deposition site and the primary photon impulse, (r-r'), is important. The practical impact of these assumptions is discussed in detail in section §4.4. Under these assumptions, equation 3.4 becomes:

$$D(r) = \int dr' \, \Phi_{\gamma^0,E}(r') \, G_{e\&\gamma>0}(E;r-r')$$

(3.5a)

Setting $s = r - r'$, $\Rightarrow$ $r' = r - s$, $dr' = -ds$, Equation 3.5a can be rewritten as:

$$D(r) = \int ds \, \Phi_{\gamma^0,E}(r-s) \, G_{e\&\gamma>0}(E;s)$$

(3.5b)

These are complimentary forms of a convolution integral which we've been

waiting for!

The primary photon fluence, $\Phi_{\gamma^0,E}(r')$, is represented simply by:

$$\Phi_{\gamma^0,E}(r') = \Phi_{\gamma^0,E}(r_0) \times e^{-\mu l} \qquad (3.6)$$

where

$\Phi_{\gamma^0,E}(r_0)$ is the photon fluence incident on the phantom surface (photons per cm^2).

μ is the linear attenuation coefficient (cm^{-1})

l is the ray length travelled in the phantom from r_0 to $r'(cm)$

The convolution technique has received a lot of attention recently as a dose

calculation algorithm (Mackie et.al. 1987, Boyer amd Moc 1986, Ahnesjö et.al. 1987,

Mohan et.al. 1986) although it appeared as early as 1949 (Johns et.al. 1949) . In much of

this previous work, the assumptions listed above have been tacit and additional ones have

been made for inhomogeneous media. From the rigorous stance of this work, these

additional assumptions merit further study, even though results obtained to date have been

very promising (Mackie et.al. 1985).

Convolution is a standard image processing algorithm used to modify a picture

element (pixel) value based on the neighbouring pixels. This technique is commonly used

for matching objects, measuring image properties, removing noise, and filtering images.

Most newsworthy has been the role it played in locating the Titanic (Byte1986). Thus,

there is incentive in developing a dose calculation algorithm which can inherit all the

advances made in image processing technology - both hardware and software.

We now look at the convolution kernels in detail.

3.3 The Kernel Data Base

Many of the assumptions of section §3.2 are not obviously acceptable. A spatially-variant Green's function of the form G($\rho(r')$; r,r') is required, rigorously speaking. However, this is currently impractical. Instead, a set of invariant Green's functions; G(r,r'), have been generated with the expectation that the variant Green's function can be approximated from this set.

The Green's functions which serve as convolution kernels were generated using Monte Carlo techniques (Mackie et.al.1987b, Nelson et.al. 1985, Ford et.al. 1978). The data base consists of a set of 23 kernels, for mono-energetic & mono-directional photon pencil beams in the energy range of 0.10 to 50.0 Mev incident on water. Approximately, one million incident photons were "forced" to interact in the center of a sphere of water with a radius of 60 cm, and the energy deposited by charged particles was separated according to the category of the photon which set the charged particles in motion. The photon categories are:

- a primary photon,
- a 'once-scattered' photon,
- a 'twice-scattered' photon,
- a 'more than twice-scattered' photon,
- a photon generated by bremsstrahlung or positron annihilation.

The energy deposited was 'binned' in a spherical coordinate system, consisting of 48 equal angular increments covering 180 degrees, and 24 radial increments from 0.05 to 60.0 cm (see Figure 3.7).

The separation into the five categories of photons was done to study the physics of radiation transport in detail. In a homogeneous medium, this information is useful in deciding the frequency of occurence and spatial influence of these interaction processes. In a heterogeneous medium, each category will be affected differently by tissue boundaries and this separation is therefore essential.

These kernels were generated originally on a Digital Equipment Corporation (DEC) VAX-11/780 computer and more recently on an IBM computer. Typical computing times on the VAX-11/780 computer ranged from about 30,000 histories per CPU hour at 0.1 MeV to 1600 histories at 50 MeV. The latest generation of the kernel data base required the equivalent of one half year of VAX-11/780 CPU time (Bielajew, private communication)! The storage requirements for the complete data base written as binary data is about 0.5 Mbytes. For this work, the data files have been re-written in ASCII for ease of data extraction which increases the storage requirements to 1.4 Mbytes.

180°

Radii	
0.05	3.0
0.1	4.0
0.15	5.0
0.2	6.0
0.3	8.0
0.4	10.0
0.5	15.0
0.6	20.0
0.8	30.0
1.0	40.0
1.5	50.0
2.0	60.0

spherical voxel

0°

3.75°
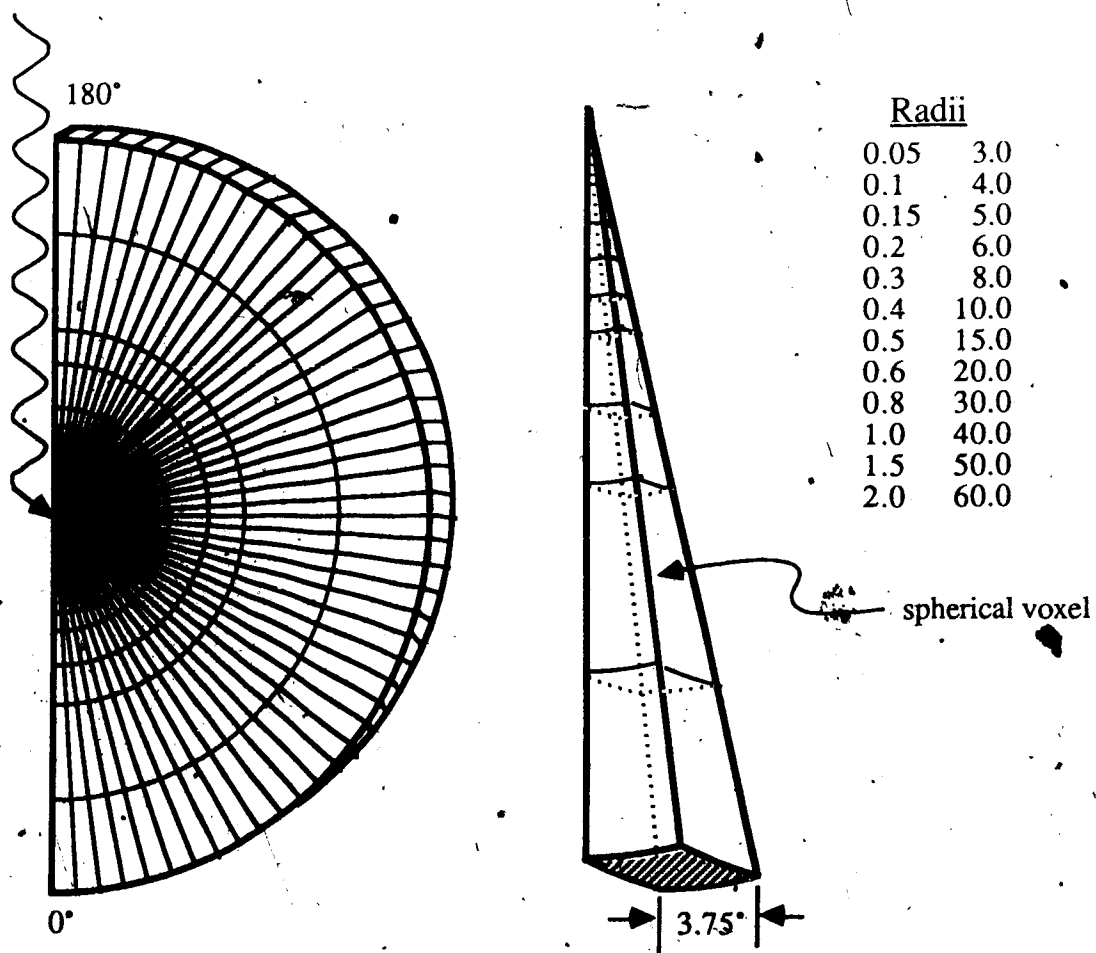
Figure 3.7. Spherical coordinate system used in the kernel generation.

3.3.1 Physical Interpretation of the Spherical Kernels

Table 3.2 shows the primary kernel for 1.25 MeV photons (representing Cobalt-60 radiation) and Table 3.3 shows the primary kernel for 5.0 MeV photons (representing 15 MV X-rays). The number in each bin represents the fraction of the incident photon energy deposited in the bin by a photon interacting at the origin. For example, the spherical bin at a mean radius of 0.175 cm and a mean angle of 50.63 degrees for 1.25 MeV photons contains a value of 3.147E-03 which means that 3.934 KeV ($3.147 \times 10^{-3} \times 1.25$MeV) is deposited in that voxel when a single 1.25 MeV photon interacts in the center of the water sphere.

We see for the 1.25 MeV primary kernel that no energy is deposited in any direction beyond a mean radius of 0.45 cm. Similarly, no energy is deposited beyond a larger mean radius of 2.5 cm for the 5.0 MeV primary kernel. This is consistent with the mean stopping power of 2 MeV/cm (§2.1.2.3). If a 1.25 MeV photon transfers all its energy to an electron, and assuming continuous slowing down, that electron would travel 0.625 cm. Similarly, an electron receiving all the energy from a 5.0 MeV photon would travel 2.5 cm. Electrons are not however continuously slowed down at a fixed rate: they slow down more quickly as they lose energy. Hence, energy from electrons is not visible beyond a radius 0.45 cm for 1.25 MeV incident photons, and beyond 2.5 cm for 5.0 MeV.

The sum of all voxels in kernel of category 'i' gives the total energy deposited by charged particles set in motion by photons which have scattered precisely 'i' times. Table 3.4 summarizes the total energy deposited by each kernel category according to the incident photon energy.

MEAN Angle (degrees)	MEAN Radius (cm)						
	0.025	0.075	0.125	0.175	0.250	0.350	0.450
1.88	2.304E-03	1.132E-03	8.718E-04	6.960E-04	9.755E-04	3.836E-04	1.412E-05
5.63	3.917E-03	3.238E-03	2.541E-03	2.013E-03	2.837E-03	1.112E-03	4.381E-05
9.38	5.415E-03	4.881E-03	3.947E-03	3.202E-03	4.565E-03	1.746E-03	6.643E-05
13.13	5.948E-03	5.871E-03	4.972E-03	4.126E-03	6.010E-03	2.281E-03	8.392E-05
16.88	6.061E-03	6.341E-03	5.656E-03	4.792E-03	7.107E-03	2.683E-03	9.172E-05
20.63	5.997E-03	6.374E-03	5.916E-03	5.194E-03	7.859E-03	2.935E-03	8.898E-05
24.38	5.866E-03	6.173E-03	5.887E-03	5.376E-03	8.213E-03	3.035E-03	8.546E-05
28.13	5.680E-03	5.817E-03	5.684E-03	5.364E-03	8.360E-03	3.003E-03	7.464E-05
31.88	5.474E-03	5.361E-03	5.343E-03	5.162E-03	8.141E-03	2.830E-03	6.599E-05
35.63	5.200E-03	4.908E-03	4.931E-03	4.837E-03	7.714E-03	2.593E-03	5.252E-05
39.38	4.913E-03	4.456E-03	4.484E-03	4.458E-03	7.131E-03	2.366E-03	3.706E-05
43.13	4.576E-03	4.005E-03	4.022E-03	4.038E-03	6.448E-03	1.956E-03	2.742E-05
46.88	4.203E-03	3.605E-03	3.575E-03	3.582E-03	5.703E-03	1.623E-03	2.053E-05
50.63	3.816E-03	3.200E-03	3.184E-03	3.147E-03	4.908E-03	1.323E-03	1.351E-05
54.38	3.399E-03	2.821E-03	2.792E-03	2.732E-03	4.207E-03	1.032E-03	8.302E-06
58.13	3.021E-03	2.481E-03	2.422E-03	2.331E-03	3.485E-03	7.973E-04	4.197E-06
61.88	2.643E-03	2.154E-03	2.070E-03	1.968E-03	2.876E-03	6.171E-04	4.388E-06
65.63	2.305E-03	1.870E-03	1.782E-03	1.668E-03	2.308E-03	4.446E-04	2.498E-06
69.38	2.015E-03	1.625E-03	1.522E-03	1.391E-03	1.859E-03	3.359E-04	1.457E-06
73.13	1.712E-03	1.396E-03	1.280E-03	1.127E-03	1.447E-03	2.343E-04	9.447E-07
76.88	1.426E-03	1.185E-03	1.062E-03	9.362E-04	1.145E-03	1.609E-04	2.862E-07
80.63	1.192E-03	9.874E-04	8.845E-04	7.490E-04	8.721E-04	1.191E-04	2.868E-07
84.38	1.019E-03	8.347E-04	7.275E-04	5.997E-04	6.615E-04	8.764E-05	7.455E-08
88.13	8.510E-04	7.035E-04	5.873E-04	4.769E-04	5.022E-04	5.827E-05	6.615E-08
91.88	7.065E-04	5.841E-04	4.828E-04	3.678E-04	3.678E-04	4.041E-05	0.000E+00
95.63	5.854E-04	4.718E-04	3.849E-04	2.918E-04	2.780E-04	2.790E-05	0.000E+00
99.38	4.828E-04	3.832E-04	3.043E-04	2.243E-04	2.035E-04	2.200E-05	0.000E+00
103.13	3.955E-04	3.081E-04	2.458E-04	1.757E-04	1.548E-04	1.516E-05	0.000E+00
106.88	3.221E-04	2.525E-04	1.978E-04	1.351E-04	1.184E-04	1.169E-05	0.000E+00
110.63	2.640E-04	2.044E-04	1.548E-04	1.127E-04	9.076E-05	8.711E-06	0.000E+00
114.38	2.093E-04	1.679E-04	1.262E-04	9.065E-05	6.976E-05	7.471E-06	0.000E+00
118.13	1.707E-04	1.370E-04	9.893E-05	6.971E-05	5.517E-05	5.153E-06	6.932E-08
121.88	1.391E-04	1.116E-04	8.185E-05	5.617E-05	4.424E-05	3.123E-06	0.000E+00
125.63	1.138E-04	8.684E-05	6.882E-05	4.385E-05	3.667E-05	3.384E-06	0.000E+00
129.38	8.863E-05	7.106E-05	5.512E-05	3.326E-05	2.868E-05	1.499E-06	0.000E+00
133.13	7.180E-05	5.680E-05	4.307E-05	2.665E-05	2.038E-05	2.040E-06	0.000E+00
136.88	5.830E-05	5.004E-05	3.703E-05	2.501E-05	1.668E-05	1.767E-06	1.490E-07
140.63	4.917E-05	4.061E-05	3.054E-05	2.120E-05	1.430E-05	1.209E-06	9.776E-08
144.38	3.894E-05	3.465E-05	2.480E-05	1.723E-05	1.288E-05	1.216E-06	0.000E+00
148.13	3.274E-05	2.771E-05	2.120E-05	1.297E-05	1.166E-05	5.156E-07	0.000E+00
151.88	2.618E-05	2.371E-05	1.689E-05	9.977E-06	8.279E-06	1.202E-06	0.000E+00
155.63	2.170E-05	1.921E-05	1.339E-05	8.271E-06	7.016E-06	7.541E-07	0.000E+00
159.38	1.699E-05	1.555E-05	1.146E-05	7.580E-06	5.556E-06	1.105E-06	0.000E+00
163.13	1.220E-05	1.112E-05	7.793E-06	5.110E-06	3.567E-06	1.711E-07	0.000E+00
166.88	9.340E-06	8.924E-06	5.016E-06	3.814E-06	3.166E-06	1.726E-07	0.000E+00
170.63	6.976E-06	6.084E-06	3.708E-06	2.694E-06	2.210E-06	1.435E-07	0.000E+00
174.38	3.879E-06	3.821E-06	1.822E-06	1.505E-06	1.353E-06	1.739E-07	0.000E+00
178.13	1.243E-06	1.188E-06	5.467E-07	5.924E-07	3.553E-07	0.000E+0	0.000E+00

Table 3.2. ENERGY deposited by electrons set-in-motion by PRIMARY 1.25 MeV photons. The total energy deposited in this sphere of 60 cm radius is 0.469 MeV.

MEAN Angle	MEAN Radius (cm)						
(degrees)	0.025	0.075	0.125	0.175	0.250	0.350	0.450
1.88	1.798E-03	1.815E-03	1.576E-03	1.365E-03	2.277E-03	1.855E-03	1.549E-03
5.63	4.717E-03	3.725E-03	3.314E-03	3.051E-03	5.421E-03	4.656E-03	4.017E-03
9.38	2.451E-03	3.028E-03	3.144E-03	3.140E-03	6.060E-03	5.630E-03	5.147E-03
13.13	1.817E-03	2.218E-03	2.436E-03	2.545E-03	5.239E-03	5.243E-03	5.106E-03
16.88	1.440E-03	1.681E-03	1.855E-03	1.968E-03	4.167E-03	4.362E-03	4.430E-03
20.63	1.166E-03	1.336E-03	1.451E-03	1.535E-03	3.259E-03	3.463E-03	3.609E-03
24.38	9.685E-04	1.096E-03	1.162E-03	1.213E-03	2.578E-03	2.767E-03	2.910E-03
28.13	8.163E-04	8.960E-04	9.299E-04	9.700E-04	2.044E-03	2.192E-03	2.356E-03
31.88	6.933E-04	7.340E-04	7.585E-04	7.821E-04	1.664E-03	1.778E-03	1.897E-03
35.63	5.900E-04	6.070E-04	6.199E-04	6.382E-04	1.349E-03	1.452E-03	1.541E-03
39.38	5.010E-04	5.016E-04	5.080E-04	5.260E-04	1.109E-03	1.184E-03	1.256E-03
43.13	4.273E-04	4.140E-04	4.231E-04	4.382E-04	9.224E-04	9.847E-04	1.019E-03
46.88	3.648E-04	3.434E-04	3.554E-04	3.667E-04	7.649E-04	8.128E-04	8.405E-04
50.63	3.053E-04	2.860E-04	2.970E-04	3.078E-04	6.403E-04	6.732E-04	7.004E-04
54.38	2.565E-04	2.418E-04	2.520E-04	2.587E-04	5.356E-04	5.536E-04	5.772E-04
58.13	2.155E-04	2.032E-04	2.111E-04	2.165E-04	4.467E-04	4.654E-04	4.678E-04
61.88	1.810E-04	1.707E-04	1.768E-04	1.815E-04	3.679E-04	3.819E-04	3.777E-04
65.63	1.500E-04	1.459E-04	1.493E-04	1.538E-04	3.086E-04	3.172E-04	3.150E-04
69.38	1.271E-04	1.224E-04	1.238E-04	1.298E-04	2.631E-04	2.565E-04	2.587E-04
73.13	1.050E-04	1.046E-04	1.056E-04	1.065E-04	2.172E-04	2.125E-04	2.045E-04
76.88	8.702E-05	8.883E-05	8.944E-05	9.036E-05	1.808E-04	1.713E-04	1.629E-04
80.63	7.103E-05	7.288E-05	7.469E-05	7.491E-05	1.484E-04	1.378E-04	1.307E-04
84.38	5.967E-05	6.117E-05	6.175E-05	6.214E-05	1.204E-04	1.122E-04	1.051E-04
88.13	5.021E-05	5.104E-05	5.218E-05	5.143E-05	9.705E-05	9.082E-05	8.200E-05
91.88	4.161E-05	4.330E-05	4.332E-05	4.171E-05	7.786E-05	7.238E-05	6.555E-05
95.63	3.398E-05	3.619E-05	3.497E-05	3.484E-05	6.458E-05	5.745E-05	5.051E-05
99.38	2.865E-05	2.905E-05	2.881E-05	2.831E-05	5.395E-05	4.632E-05	3.927E-05
103.13	2.345E-05	2.395E-05	2.428E-05	2.286E-05	4.271E-05	3.749E-05	3.183E-05
106.88	1.931E-05	2.043E-05	1.842E-05	1.913E-05	3.412E-05	3.096E-05	2.693E-05
110.63	1.601E-05	1.593E-05	1.462E-05	1.473E-05	2.814E-05	2.335E-05	2.131E-05
114.38	1.300E-05	1.350E-05	1.282E-05	1.215E-05	2.320E-05	1.894E-05	1.776E-05
118.13	1.072E-05	1.020E-05	9.802E-06	9.101E-06	1.896E-05	1.611E-05	1.507E-05
121.88	8.797E-06	8.537E-06	7.976E-06	8.068E-06	1.436E-05	1.294E-05	1.174E-05
125.63	6.863E-06	7.035E-06	6.832E-06	6.075E-06	1.174E-05	1.131E-05	9.510E-06
129.38	5.576E-06	5.421E-06	4.778E-06	5.081E-06	9.528E-06	9.597E-06	7.590E-06
133.13	4.587E-06	4.330E-06	4.638E-06	3.980E-06	8.009E-06	7.385E-06	6.638E-06
136.88	3.606E-06	3.436E-06	3.500E-06	3.527E-06	6.687E-06	6.293E-06	5.582E-06
140.63	2.793E-06	2.981E-06	2.830E-06	3.180E-06	5.996E-06	5.447E-06	4.276E-06
144.38	2.511E-06	2.511E-06	2.692E-06	3.039E-06	4.457E-06	4.309E-06	3.965E-06
148.13	2.175E-06	2.350E-06	2.111E-06	2.108E-06	3.663E-06	3.056E-06	3.281E-06
151.88	1.730E-06	1.765E-06	1.617E-06	1.762E-06	3.370E-06	2.608E-06	2.445E-06
155.63	1.321E-06	1.364E-06	1.542E-06	1.290E-06	2.927E-06	2.061E-06	2.102E-06
159.38	9.895E-07	9.893E-07	1.018E-06	1.022E-06	2.039E-06	2.033E-06	1.891E-06
163.13	8.515E-07	8.226E-07	7.473E-07	8.134E-07	1.657E-06	1.625E-06	1.436E-06
166.88	6.443E-07	4.631E-07	7.053E-07	7.052E-07	1.163E-06	1.147E-06	1.066E-06
170.63	3.477E-07	3.349E-07	5.368E-07	6.062E-07	9.359E-07	7.733E-07	6.810E-07
174.38	1.728E-07	1.831E-07	2.540E-07	2.051E-07	5.006E-07	7.249E-07	5.657E-07
178.13	3.219E-08	5.265E-08	9.816E-08	3.982E-08	1.763E-07	1.965E-07	1.960E-07

Table 3.3. ENERGY deposited by electrons set-in-motion by PRIMARY 5.0 MeV photons. The total energy deposited in this sphere of 60 cm is 0.631.

MEAN Angle	MEAN Radius (cm)						
(degrees)	0.550	0.700	0.900	1.250	1.750	2.500	3.500
1.88	1.305E-03	2.112E-03	1.624E-03	2.737E-03	1.419E-03	2.843E-04	0.000E+00
5.63	3.512E-03	5.766E-03	4.547E-03	7.870E-03	4.071E-03	7.994E-04	0.000E+00
9.38	4.680E-03	8.074E-03	6.633E-03	1.185E-02	6.316E-03	1.209E-03	0.000E+00
13.13	4.871E-03	8.891E-03	7.696E-03	1.444E-02	7.901E-03	1.482E-03	0.000E+00
16.88	4.422E-03	8.529E-03	7.842E-03	1.554E-02	8.849E-03	1.647E-03	0.000E+00
20.63	3.707E-03	7.497E-03	7.296E-03	1.551E-02	9.071E-03	1.618E-03	0.000E+00
24.38	3.043E-03	6.336E-03	6.413E-03	1.451E-02	8.726E-03	1.497E-03	0.000E+00
28.13	2.468E-03	5.233E-03	5.459E-03	1.291E-02	7.950E-03	1.276E-03	0.000E+00
31.88	1.999E-03	4.258E-03	4.553E-03	1.108E-02	6.966E-03	1.035E-03	0.000E+00
35.63	1.617E-03	3.450E-03	3.716E-03	9.326E-03	5.782E-03	7.761E-04	0.000E+00
39.38	1.322E-03	2.809E-03	3.026E-03	7.612E-03	4.658E-03	5.617E-04	0.000E+00
43.13	1.070E-03	2.283E-03	2.438E-03	6.135E-03	3.636E-03	3.990E-04	0.000E+00
46.88	8.814E-04	1.858E-03	1.963E-03	4.833E-03	2.708E-03	2.620E-04	0.000E+00
50.63	7.266E-04	1.492E-03	1.536E-03	3.742E-03	1.987E-03	1.705E-04	0.000E+00
54.38	5.855E-04	1.212E-03	1.219E-03	2.877E-03	1.391E-03	1.107E-04	0.000E+00
58.13	4.766E-04	9.683E-04	9.681E-04	2.181E-03	9.650E-04	6.834E-05	0.000E+00
61.88	3.894E-04	7.716E-04	7.531E-04	1.621E-03	6.732E-04	3.998E-05	0.000E+00
65.63	3.095E-04	6.126E-04	5.734E-04	1.190E-03	4.612E-04	2.556E-05	0.000E+00
69.38	2.512E-04	4.742E-04	4.439E-04	8.592E-04	3.040E-04	1.482E-05	0.000E+00
73.13	2.000E-04	3.698E-04	3.378E-04	6.296E-04	2.065E-04	1.064E-05	0.000E+00
76.88	1.596E-04	2.937E-04	2.560E-04	4.609E-04	1.345E-04	5.357E-06	0.000E+00
80.63	1.238E-04	2.327E-04	1.972E-04	3.329E-04	9.231E-05	4.361E-06	0.000E+00
84.38	9.549E-05	1.730E-04	1.478E-04	2.458E-04	5.997E-05	2.368E-06	0.000E+00
88.13	7.688E-05	1.352E-04	1.115E-04	1.814E-04	4.515E-05	2.388E-06	0.000E+00
91.88	6.026E-05	1.047E-04	8.270E-05	1.308E-04	3.629E-05	1.667E-06	0.000E+00
95.63	4.691E-05	7.762E-05	6.196E-05	9.906E-05	2.462E-05	7.530E-07	0.000E+00
99.38	3.712E-05	6.020E-05	4.825E-05	6.758E-05	1.755E-05	4.904E-07	0.000E+00
103.13	3.015E-05	4.758E-05	3.561E-05	5.713E-05	1.402E-05	5.827E-07	0.000E+00
106.88	2.469E-05	3.643E-05	3.074E-05	4.755E-05	9.758E-06	5.196E-07	0.000E+00
110.63	1.951E-05	3.202E-05	2.327E-05	3.121E-05	8.146E-06	2.983E-07	0.000E+00
114.38	1.468E-05	2.534E-05	1.927E-05	2.787E-05	6.765E-06	2.407E-07	0.000E+00
118.13	1.135E-05	1.818E-05	1.680E-05	2.418E-05	5.814E-06	3.424E-07	0.000E+00
121.88	1.115E-05	1.471E-05	1.283E-05	1.977E-05	4.648E-06	2.760E-07	0.000E+00
125.63	8.783E-06	1.205E-05	1.166E-05	1.539E-05	3.731E-06	3.224E-07	0.000E+00
129.38	6.966E-06	1.112E-05	9.272E-06	1.454E-05	3.112E-06	2.361E-07	0.000E+00
133.13	5.520E-06	1.009E-05	8.009E-06	1.211E-05	2.243E-06	1.121E-07	0.000E+00
136.88	5.548E-06	8.394E-06	6.780E-06	8.298E-06	2.285E-06	3.343E-08	0.000E+00
140.63	5.188E-06	6.790E-06	5.271E-06	6.991E-06	1.078E-06	9.058E-08	0.000E+00
144.38	3.644E-06	4.891E-06	4.863E-06	5.424E-06	5.440E-07	1.538E-07	0.000E+00
148.13	2.627E-06	4.297E-06	4.367E-06	6.220E-06	1.274E-06	2.762E-08	0.000E+00
151.88	1.877E-06	3.493E-06	3.187E-06	5.749E-06	7.279E-07	5.038E-08	0.000E+00
155.63	2.212E-06	2.760E-06	2.289E-06	3.065E-06	6.797E-07	9.094E-08	0.000E+00
159.38	1.945E-06	2.781E-06	1.951E-06	2.697E-06	5.463E-07	9.023E-08	0.000E+00
163.13	1.136E-06	2.469E-06	2.169E-06	2.269E-06	4.661E-07	0.000E+00	0.000E+00
166.88	1.034E-06	2.239E-06	1.861E-06	2.075E-06	4.894E-07	0.000E+00	0.000E+00
170.63	7.955E-07	1.400E-06	1.198E-06	1.275E-06	3.632E-07	0.000E+00	0.000E+00
174.38	4.320E-07	8.052E-07	3.944E-07	1.228E-06	7.473E-07	6.176E-08	0.000E+00
178.13	9.613E-08	1.290E-07	9.970E-08	3.968E-08	2.324E-07	0.000E+00	0.000E+00

Table 3.3.(cont.) ENERGY deposited by electrons set-in-motion by PRIMARY 5.0 MeV photons.

Kernel Category	Energy of Incident Photon (MeV)			
	1.25	(100%)	5.00	(100%)
Primary	0.586	(46.9%)	3.154	(63.1%)
First scatter	0.260	(20.8%)	0.844	(16.9%)
Second scatter	0.127	(10.2%)	0.263	(5.3%)
Multiple scatter	0.234	(18.7%)	0.263	(5.3%)
Brem & Annihilation	0.003	(0.3%)	0.158	(3.2%)
Total	1.210	(96.9%)	4.682	(93.8%)

Table 3.4. Total energy deposited by kernel category in a sphere of radius 60 cm.

These numbers indicate which interactions are more important for various energies, and the extent of energy escaping beyond the water sphere of 60 cm radius. As expected, there is more energy leakage at 5 MeV than at 1.25 MeV.

For 1.25 MeV photons the following comments are appropriate.

- The total energy deposited by the primary kernel corresponds to the average energy absorbed (E_{ab}). From Johns and Cunningham (1983), $E_{ab} = 0.586$ MeV which corresponds extremely well to the total energy deposited by the primary kernel.

- The primary kernel accounts for 47% of the incident energy deposited.

- The scatter kernels account for 49% of the incident energy deposited. The first scatter kernel (21%) contains less energy than the higher order scatter kernels combined (29%).

- Bremsstrahlung and annihilation radiation is negligible. It accounts for only 0.0032 MeV (0.3%) of the incident energy. The amount of bremsstrahlung energy is given by $E_{tr} - E_{ab}$. The predicted value from Johns and Cunningham data is 0.588-0.586=0.002 MeV (0.2%). Therefore up to 0.2% (if all bremsstrahlung radiation was reabsorbed) of the total bremsstrahlung and annihilation kernel can be explained by bremsstrahlung. The balance (0.1%) is

contributed by annihilation events (which are very minimal for 1.25 MeV photons).

- 3% of the incident photon energy escapes from the sphere of water.

For 5.0 MeV photons the following should be noted:

- From Johns and Cunningham, E_{ab} = 3.16 MeV in excellent agreement with the kernel value of 3.154 MeV.

- The primary kernel is most important contributing 63% of the incident energy.

- The total of all the scatter kernels accounts for only 27% of the incident energy. The second and multiple scatter kernel contain approximately the same amount of energy, and the first scatter kernel contains about 50% more energy than the higher order scatter kernels combined.

- Bremsstrahlung and annihliation radiation account for 3% of the incident energy. Johns and Cunningham yields a value of 3.21-3.16=0.05 MeV (1%) for bremsstrahlung radiation. The remaining 2% is attributed to annihilation radiation which is more prevalent for 5.0 MeV photons.

- 6% of the incident photon energy escapes from the sphere of water.

As the incident photon energy increases, the fractional amount of energy transferred to the primary scattered electron also increases. This is evidenced by the percentage of the energy contained by the primary kernel: 63% for 5.0 MeV photons, and 47% for 1.25 MeV photons.

We have noted that the total energy deposited by the sum of all kernels is less than unity (100%). The difference from unity (i.e. 6% for a 5 MeV photon) is the fractional energy escaping from the sphere of water of radius 60 cm. Let us verify that the 6% of the incident photon energy leaving a water sphere of radius 60 cm is reasonable. All incident photons are forced to interact at the center of a water sphere, yielding an average energy of

E_0-E_{tr}=1.79 MeV for the first scattered photon. The fraction of first scattered photons escaping from the water sphere of radius 60 cm is given by: $\Phi/\Phi_0 = e^{-\mu x}$. This amounts to 4.16% of the 1.8 MeV photons ($\mu \approx 0.053$ cm^{-1}) which corresponds to an energy leakage of 0.0416 x 1.79 MeV = 74.5 keV (i.e. 1.5% of the incident 5.0 MeV photon energy). The average energy of the second scattered photon is 1.8 - 0.9=0.9Mev. Assuming the second scattering occured at a distance of one mean free path away from the first scattering, then the location of the second scatter event will be 60-13=47 cm from the edge of the water sphere. 2.9% of the 0.9 MeV photons would escape from the water sphere carrying with them 0.5% of the incident 5 MeV photon energy. Thus, first and second scatter events account for a loss of 2% of the incident energy. This does not appear to agree all that well with the kernel losses of 6%. If the above calculation is performed with the most probable energy of the scattered photon instead of the mean energy, we find that the energy loss from first scatter events alone amounts to 10% of the incident energy. The true energy loss will lie somewhere in between our calculated values of 2% and 10% loss; thus the kernel value of 6% seems reasonable.

Repeating the above calculations for incident 1.25 MeV photons we find the energy loss using mean scattered photon energies for first and second scatter events is 0.5%. Using the most probable energy of the first scattered photon, the energy loss is 1.2% for first scattered photon only. Including the contribution from second scattered photons, the energy loss is about 2.2% which is approaching the kernel value of 3%. More scattered photons need to be followed in the case of 1.25 MeV photons because the scattered photons carry away a larger fraction of the incident energy than do the scattered 5.0 MeV photons.

Using the primary kernel, the sum of the energy deposited in bins along a ray yields the electron energy deposited along a particular direction. Figure 3.8 plots the scattered electron energy as a function of angle. Comparison with results of Compton theory

(Figure 2.6) should not yield precise agreement since Compton theory determines the

scattered electron energy launched at the site of the initial Compton interaction. On the

other hand, Figure 3.8 shows the energy deposited by the transport of electrons in the

phantom after slowing down and multiple scattering away from the primary interaction site.

If all electrons were transported along a straight-line ray from the interaction point, then the

two results would be identical. However, this is not the case and we expect Figure 3.8 to

be a 'blurred' image of the Compton theory graph, because of the electron multiple

scattering.
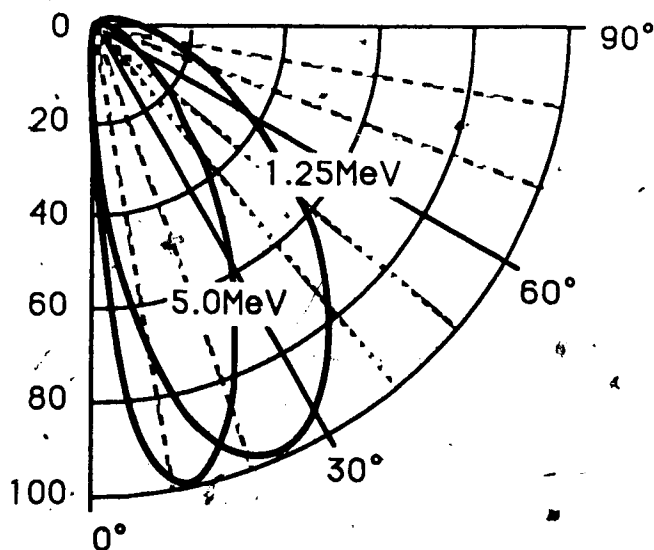
Figure 3.8. Angular distribution of the energy from the primary kernels for 1.25 and 5.0 MeV incident photons.

3.3.2 Conversion to a Cartesian Coordinate System

As previously mentioned, the kernels are specified in a spherical coordinate system. The symmetry of this system greatly reduces the computer time required to generate the kernels. However, the spherical coordinate system causes two problems:

1) The primary photon fluence is generally calculated from a series of CT scans which are based on a Cartesian coordinate system. This author is not

aware of any direct techniques for convolving a kernel represented in a
spherical coordinate system with an impulse function represented in a
Cartesian coordinate system.

2) Graphical display of the kernel on a raster graphics device requires a
Cartesian coordinate system.

Thus, for simplicity in both calculation and display, the spherical kernels need to be converted to a Cartesian geometry. A program written by T.R. Mackie and R. Andrews and Mackie (1986) has been modified by this author to convert the spherical kernels to an equivalent three-dimensional Cartesian kernel. The number and size of kernel voxels in the Cartesian system determines the spatial resolution of dose, the spatial extent of energy deposition, and the speed of the convolution calculation. Indeed, the ability to change these for specific dose calculation requirements is an inherent advantage of the convolution approach.

Figure 3.9 illustrates the Cartesian kernel geometry. The number of voxels comprising the kernel is characterized by three parameters: top, bottom and edge. 'Top' specifies the number of voxels in the kernel above the interaction voxel; 'bottom' specifies the number of voxels below the interaction voxel; and 'edge' specifies the number of voxels lateral to the interaction voxel. The Cartesian coordinate system has its origin located in the center of the interaction voxel, with the Z axis in the direction of the incident photon. The indices i,j,k refer to the pixel location from the origin in the x,y,z direction respectively. The voxel indices (i,j,k) thus range from (-edge:edge, -edge:edge, top:bottom).

The computing time (VAX-11/780 CPU seconds) required to perform the spherical to Cartesian conversion is shown in Table 3.5. These conversion times are not negligible, so it is beneficial to pre-store kernels for 'standard' Cartesian voxel sizes, commensurate with the desired spatial resolutions in the dose distribution.
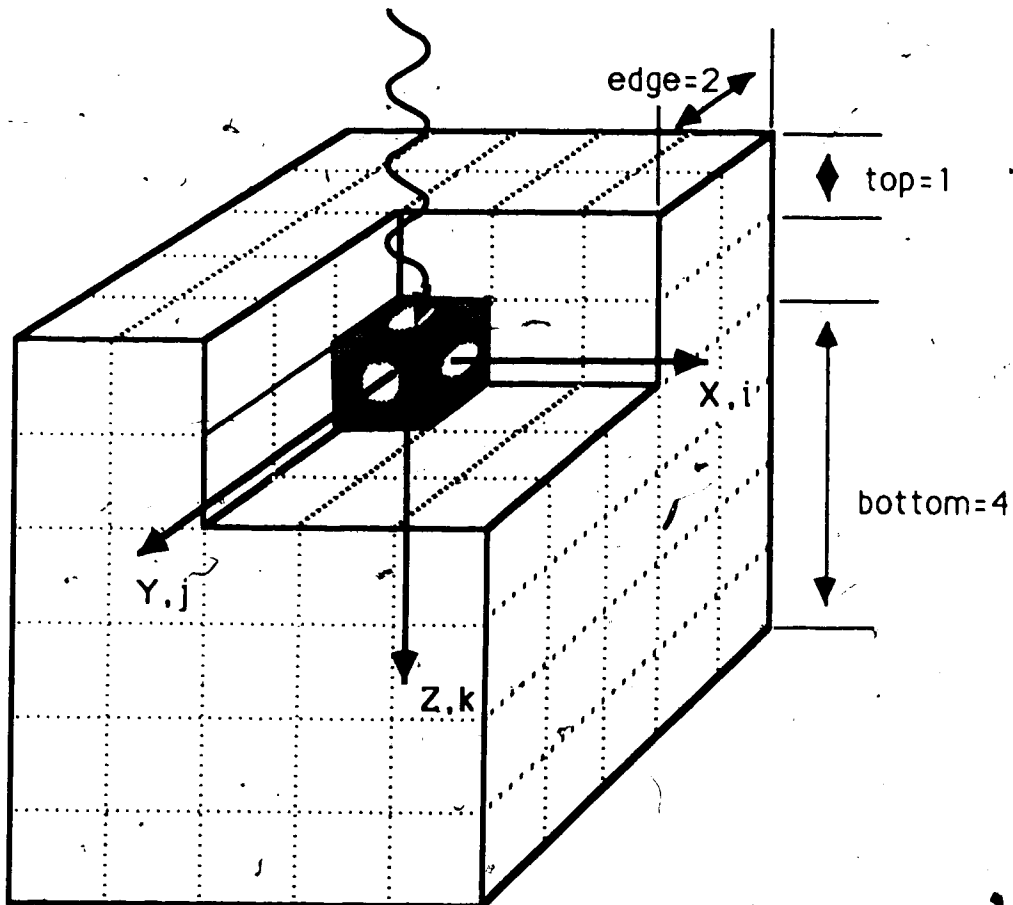
Figure 3.9. Illustration of a 3D Cartesian kernel.

Kernel Dimension			Calculation Time
top	bottom	edge	(CPU seconds)
-15	47	31	242
-13	50	28	143
-10	36	15	68
-3	12	7	24

Table 3.5. Calculation times on a VAX 11/780 computer for kernel conversion from a spherical geometry to a 3D Cartesian geometry.

➤ Table 3.6 shows the primary kernel in a Cartesian geometry for 1.25 MeV photons (3.6a) and 5.0 MeV photons (3.6b). The voxel size in this example is 1cm^3. The values of top, bottom, and edge are -3,3,3, respectively, which means the dimensions of the kernel are (-3:3, -3:3, -3:3). A four-fold symmetry exists (i.e. the voxel value in planes at

j=±n, i=±n are identical). Thus, only one quadrant of the kernel has been presented. As in the spherical kernel, the values in each voxel represent the fraction of the incident photon energy deposited in that voxel. The 'total energy' is the fraction of the total incident energy deposited in the complete plane (not just the half-plane). Adding all the planes together we can determine the total energy deposited in a region covered by the extent of the primary kernel (i.e. a cube with edge dimension of 7 cm). The total is 0.631 (i.e. 63.1%) for 5.0 MeV incident photons. This value agrees with that obtained from the spherical primary kernel (Table 3.3), so we are assured that the extent of the primary kernel is large enough to receive all the energy deposited by electrons set-in-motion by the primary photon. If the kernel extent is too small, then energy will artifically 'escape'. This situation is definitely to be avoided for the primary kernel, since the bulk of the energy is deposited in the primary interaction (at 5 MeV).

When a Cartesian kernel extent is specified which is the same or larger than a 60 cm sphere, the total energy contained in the Cartesian kernel should be identical to the energy contained in the spherical kernel. Otherwise, energy has not been conserved in the spherical to Cartesian conversion process.

The primary kernel for 1.25 MeV incident photons (Table 3.6a) contains zero's everywhere except at the interaction voxel (0,0). For this voxel size (1cm³), the primary energy is deposited 'on-the-spot' because of the reduced range of the ejected electrons (0.45cm). The value of this element (0.469%) agrees with the total energy deposited in the primary spherical kernel. As will be seen, if we were examining kernels other than the primary kernel, this agreement would not be as good since a (7cm)³ cube is not large enough to contain all the energy deposited by the first scatter, second scatter, multiple scatter or bremsstrahlung and annihilation processes.

Max value: 4.69E-01 Total: 4.69E-01
***** J = 0*****

k \ i	0±1	±2	±3	
-3				
-2				
-1				
0	4.69E-01			
1				
2				
3				

Max value: 0.00E-00 Total: 0.00E-00
***** J = ±1*****

k \ i	0	±1	±2	±3
-3				
-2				
-1				
0				
1				
2				
3				

Table 3.6a. 2D planes through the 3D Cartesian primary kernel for 1.25 MeV photons.

Max value: 2.31E-01 Total: 5.44E-01
***** J = 0*****

k \ i	0±1	±2	±3	
-3	9.85E-12	3.26E-13		
-2	1.98E-06	3.52E-07	2.33E-10	
-1	8.40E-05	3.63E-05	1.54E-06	8.79E-13
0	2.22E-01	2.89E-03	4.37E-05	4.86E-11
1	2.31E-01	2.16E-02	1.64E-04	8.34E-12
2	2.96E-02	5.85E-03	6.31E-07	
3	3.63E-08	8.28E-10		

Max value: 2.16E-02 Total: 4.30E-02
***** J = ±1*****

k \ i	0	±1	±2	±3
-3	3.26E-13	4.02E-14		
-2	3.52E-07	9.12E-08	3.72E-11	
-1	3.63E-05	1.42E-05	3.60E-07	3.51E-14
0	2.89E-03	6.23E-04	1.02E-05	4.91E-16
1	2.16E-02	4.60E-03	2.45E-05	2.63E-13
2	5.85E-03	1.05E-03	4.83E-06	
3	8.29E-10	2.73E-11		

Max value: 1.64E-04 Total: 2.80E-04
***** J = ±2*****

k \ i	0±1	±2	±3	
-3				
-2	2.33E-10	3.72E-11	1.88E-20	
-1	1.54E-06	3.60E-07	1.43E-11	
0	4.37E-05	1.02E-05	2.35E-09	
1	1.64E-04	2.45E-05	1.41E-10	
2	6.31E-07	4.83E-08	3.18E-20	
3				

Max value: 4.86E-11 Total: 5.84E-11
***** J = ±3*****

k \ i	0	±1	±2	±3
-3				
-2				
-1	8.79E-13	3.49E-14		
0	4.86E-11	4.91E-16		
1	8.33E-12	2.48E-13		
2				
3				

Table 3.6b. 2D planes through the 3D Cartesian primary kernel for 5.0 MeV photons.

3.3.3 Kernel Compression

In an effort to reduce the data storage, it is sometimes appropriate to compress the 3D kernel to a 2D or 1D kernel. This is useful if a 2D or 1D convolution may be used to determine the dose in a plane or along a line only (i.e. a profile). However, this "shortcut" is permissable only if we assume: a uniform fluence across the incident beam (in the compression direction), the radiation field size is wide enough (in the compression direction) to achieve lateral electronic equilibrium, and the irradiated system is homogeneous. This compression can be performed as follows:

compression to a 2-D kernel:

$$G_2(i,k) = \sum_{j=-edge}^{edge} G(i,j,k)$$ (3.7a)

$$= G(i,0,k) + \sum_{j=1}^{edge} 2 \times G(i,j,k)$$ (3.7b)

compression to a 1-D kernel:

$$G_1(k) = \sum_{i=-edge}^{edge} G_2(i,k)$$ (3.8a)

$$= G_2(0,k) + \sum_{i=1}^{edge} 2 \times G_2(i,k)$$ (3.8b)

$$= G_2(0,k) + \sum_{i=1}^{edge} 2 \times \left[G(i,0,k) + \sum_{j=1}^{edge} 2 \times G(i,j,k) \right]$$ (3.8c)

$$= G(0,0,k) + 2 \sum_{i=1}^{edge} G(i,0,k) + 4 \sum_{i=1}^{edge} \sum_{j=1}^{edge} G(i,j,k)$$ (3.8d)

Table 3.7 illustrates the compressed 2D and 1D versions of the primary 5.0 MeV kernel of Table 3.6b.

Max value: 2.75E-01 Total: 6.31E-01
***** Compressed in J*****

k \ i	0	±1	±2	±3
-3	1.05E-11	4.06E-13		
-2	2.68E-06	5.34E-07	3.07E-10	
-1	1.60E-04	6.55E-05	2.26E-06	9.49E-13
0	2.28E-01	4.15E-03	6.41E-05	4.86E-11
1	2.75E-01	3.08E-02	2.13E-04	8.86E-12
2	4.13E-02	7.96E-03	7.28E-07	
3	3.80E-08	8.83E-10		

a)

Max value: 3.37E-01
Total: 6.31E-01
Compressed in J and I

k	0
-3	1.13E-11
-2	3.75E-06
-1	2.96E-05
0	2.36E-01
1	3.37E-01
2	5.72E-02
3	3.98E-08

b)

Table 3.7. Compressed kernel for 5.0 MeV incident photons.
a) 2D compressed kernel
b) 1D compressed kernel

3.3.4 Physical Interpretation of the Cartesian Kernels

The primary kernels used in section §3.3.2 spanned a very limited spatial extent, only covering a volume $(7cm)^3$. In order to accurately represent the first-scatter, second scatter, multiple scatter, and bremsstrahlung and annihilation kernels a much larger kernel extent is required. Cartesian kernels were generated with a voxel size of $1cm^3$ and dimensions of top= 10, bottom=40, edge=26. Compressed 2D kernels are shown as pictures in Figures 3.10, 3.11, and 3.12, in which the picture intensity is modulated by kernel values. These pictures were generated by self-normalizing the kernels to their respective maxima and then mapping the kernel information to an image consisting of 256x256 picture elements (pixels). Depending upon the kernel extent, one kernel voxel was mapped to either 4 or 16 pixels. This magnifies the kernel in an effort to make it more visible. In some cases, the logarithm of the kernel data was also taken to expand its range of visibility.

To the right of each kernel in Figures 3.10-3.12 is the legend indicating the kernel values associated with each colour. For example, violet represents those pixels which received 95% or higher of the energy deposited in the 'hottest' pixel. Red represents a value of 75% to 95% of the maximum pixel energy and so on until we get to dark blue which represents a value of 1-2% of the hottest pixel. Pixels containing less than 1% are black.

The amount of energy contained in the hottest pixel of each kernel is displayed in Table 3.8, relative to the hottest pixel in the total kernel. Table 3.4 (presented earlier) shows the relative amount of energy deposited in the *complete kernel*, whereas Table 3.8 shows the relative amount of energy deposited in the *hottest pixel*. Table 3.8 is used only to relate the true relative intensity of the images in Figure 3.11.

THE QUALITY OF THIS MICROFICHE
IS HEAVILY DEPENDENT UPON THE
QUALITY OF THE THESIS SUBMITTED
FOR MICROFILMING.

UNFORTUNATELY THE COLOURED
ILLUSTRATIONS OF THIS THESIS
CAN ONLY YIELD DIFFERENT TONES
OF GREY.

LA QUALITE DE CETTE MICROFICHE
DEPEND GRANDEMENT DE LA QUALITE DE LA
THESE SOUMISE AU MICROFILMAGE.

MALHEUREUSEMENT, LES DIFFERENTES
ILLUSTRATIONS EN COULEURS DE CETTE
THESE NE PEUVENT DONNER QUE DES
TEINTES DE GRIS.

	Maximum pixel values (MeV) for:			
kernel type	1.25 MeV photons		5.0 MeV photons	
total	0.600	(100%)	1.405	(100%)
primary	0.586	(97.7%)	1.375	(97.9%)
1st scatter	0.00128	(2.1%)	0.0262	(1.9%)
2nd scatter	0.000759	(0.13%)	0.000745	(0.053%)
multiple scatter	0.000220	(0.037%)	0.000171	(0.12%)
bremsstrahlung & annihilation	0.00265	(0.011%)	0.00261	(0.19%)

Table 3.8. Comparison of the 'hottest' pixel values for each kernel category.'
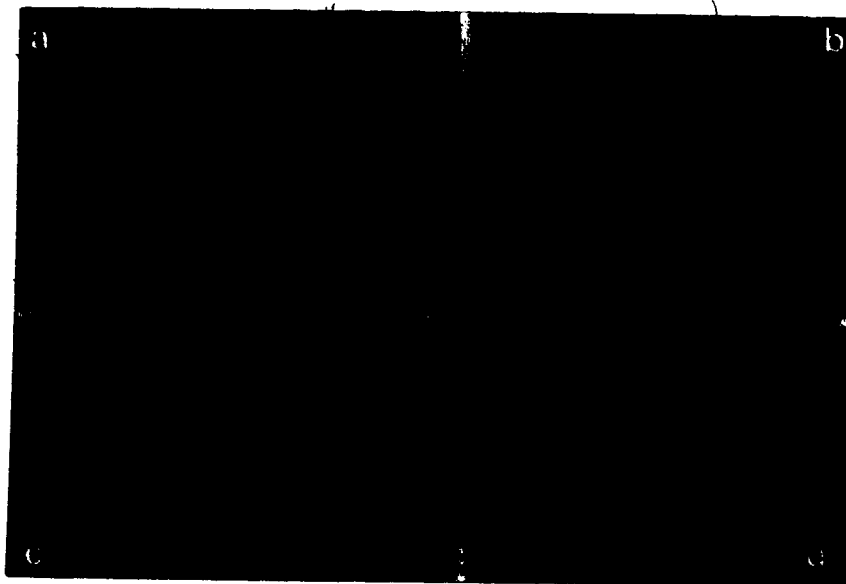
Figure 3.10. Total and primary kernels for 1.25 and 5.0 MeV photons. A voxel size of 1.0 cm^3 and dimensions of top=-10, bottom=40, and edge is 26 were used.
a) 1.25 MeV total   b) 5.0 MeV total
c) 1.25 MeV primary   d) 5.0 MeV primary

Figure 3.11. First and second scatter kernels for 1.25 and 5.0 MeV photons.
a) 1.25 MeV first scatter   b) 5.0 MeV first scatter
c) 1.25 MeV second scatter   d) 5.0 MeV second scatter

Figure 3.12. Multiple-scatter and bremsstrahlung & annihilation kernels for 1.25 and 5.0 MeV photons.
a) 1.25 MeV multiple scatter   b) 5.0 MeV multiple scatter
c) 1.25 MeV brem & annih   d) 5.0 MeV brem & annih

3.3.4.1   Total Kernel

The total kernel represents the energy deposited by charged particles which have

been set in motion by primary photons and their subsequent shower of secondary photons.

The total kernel is computed from the individual kernels by simple summation:

$$G_{tot}(i,k) = \sum_{l=0}^{4} G_l(i,k) \tag{3.9}$$

where

> G_0 represents the primary kernel. G_1 the first-scatter kernel. G_2 the second-scatter. G_3 the multiple-scatter. and G_4 the bremsstrahlung and annihilation kernel

The total kernel for incident photons of 1.25 MeV (Figure 3.10a) spreads energy

over a region 1 pixel wide and 2 pixels large (1cm x 2cm), indicating very localized energy

deposition for this energy.

For the case of 5.0 MeV incident photons (Figure 3.10b), energy is spread 2 pixels

downstream, 1 pixel upstream, and 1 pixel laterally, covering a total area of 7 cm^2. The

hottest pixel for the 5.0 MeV is not the interaction site, but the first pixel downstream of the

interaction site.

3.3.4.2   Primary Kernel

The primary kernel for incident photons of 1.25 MeV (Figure 3.10c) is zero

everywhere except at the interaction pixel, as is to be expected by the analysis in §3.3.2.

Comparison with the total kernel (Figure 3.10a) indicates that scattered photons have

carried energy from the interaction pixel to the pixel immediately downstream.

In contrast, the 5.0 MeV primary kernel (Figure 3.10d) appears identical to the 5.0

MeV total kernel (Figure 3.10b). This indicates that the scattered photon kernels (and

bremsstrahlung and annihilation kernel) contribute minimal energy to the pixels in the total

kernel. This should not be interpreted to mean that scattered photons are unimportant! As seen in §3.2, the primary kernel contains 63% of the incident energy, while the scatter kernels contain another 27% of the incident energy. The energy contained in the primary kernel is spread over a few pixels (7), so that each pixel receives a 'large' amount of energy. However, there are a vast number of pixels in the scatter kernels which contribute small amounts of energy per pixel, with the net result that the total contribution from the scatter kernels can be significant (27%).

3.3.4.3 First Scatter Kernel

The first scatter kernel for incident 1.25 MeV photons (Figure 3.11a) is completely contained within the selected extent (i.e. 1 cm pixels, top=-10, bottom=40, edge=26). However, the 5.0 MeV kernel (Figure 3.11b) is just 'clipped' in the forward direction, indicating the 'bottom' parameter is not quite large enough to encompass the downstream extent of the first scatter events.

In this work, all the kernels were obtained by Monte Carlo techniques. It is also possible to obtain the first scatter kernel analytically by convolving the primary kernel with first scattered photon fluence as suggested by Boyer (1984).

3.3.4.4 Second Scatter Kernel

The second scatter kernel for incident 1.25 MeV photons (Figure 3.11c) is truncated in the forward direction at the 5% level, while the 5.0 MeV kernel (Figure 3.11d) is truncated in the forward direction at the 25% level. Comparing the primary, first-scatter, and second-scatter kernels, we see the pixel of maximum energy deposition is moving farther downstream from the interaction pixel, with the increasing order of scatter. The shape of the second scatter component is very similar to the first scatter component as has been contended by Wong and Henkelman (1983).

3.3.4.5 Multiple Scatter Kernel

The multiple scatter kernel for incident photons of 1.25 MeV (Figure 3.12a) appears almost isotropic. The position of maximum energy deposition has moved downstream even more that for the second scatter kernel as this component "builds up" with depth. The multiple scatter kernel is clipped in the forward and backward direction at the 25% level and laterally at the 5% level.

The 5.0 MeV kernel (Figure 3.12b) is more forward peaked and is clipped in the forward direction at the 50% level, in the backwards direction at the 25% level, and laterally at the 10% level. This clipping appears serious, but recall that this kernel's total energy content is only 5% of the incident energy (Table 3.3).

3.3.4.6 Bremsstrahlung and Annihilation Kernel

This kernel scores the energy deposited by electrons which have been set in motion by bremsstrahlung or annihilation radiation (independent of the order of photon scattering). The Bremsstrahlung and Annihilation kernel (B&A) deposits most of its energy just downstream of the interaction pixel; but, there is a fairly large region over which a small amount of energy is deposited.

The contribution to the 1.25 MeV B&A kernel (Figure 3.12c) from annihilation radiation is negligible, since this energy is close to the threshold for pair production (i.e. 1.02 MeV, see §2.1.1.5). In the case of the 5.0 MeV kernel, (Figure 3.12d) both annihilation and bremsstrahlung radiation are more prevalent. It has been stated (Fitzgerald et.al. 1967) that for low energy electrons, most bremmstrahlung photons are emitted at right angles to the incident electron. As the electron energy goes up, the direction of the emitted photon moves forward. Thus, for high energy electrons (i.e. the 5.0 MeV kernel), the photon fluence from bremmstrahlung radiation is more forward peaked, as seen in Figure 3.12d.

3.3.5 Energy Loss versus Spatial Extent

Figure 3.13 shows the relative physical sizes of three different kernels. The vertical arrow represents a pencil beam of photons which is forced to interact at the tip of the arrow. The circle represents the sphere used to score the energy deposited in the Monte Carlo generation of the kernels. The rectangles represent the spatial extent of two Cartesian kernels, denoted as 'small' and 'medium'. The kernel pixel size, kernel dimensions (top,bottom,edge), and spatial extent are shown in Table 3.9.

incident photon beam

60 cm water sphere

0.1 cm small

1.0 cm medium
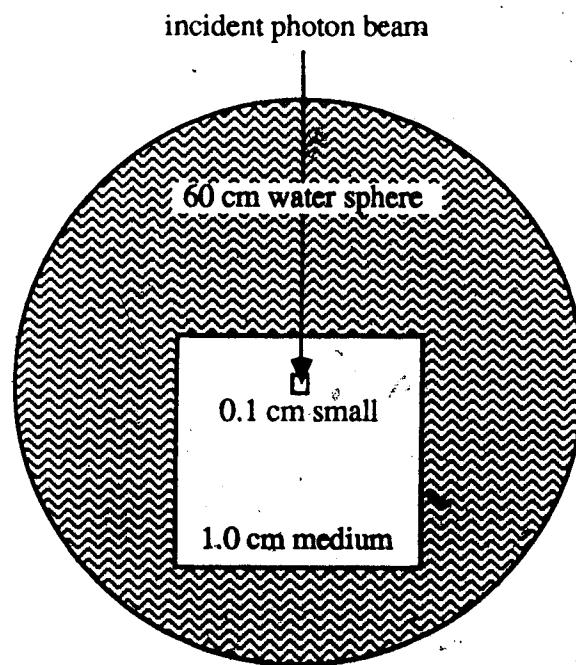
Figure 3.13. Spatial extent of small and medium Cartesian kernels, relative to the spherical kernel.

	pixel size (cm)	dimensions (pixels)	spatial extent (cm)
small	0.1 (cartesian)	-5, 20, 13	-0.5, 2, ±1.3
medium	1.0 (cartesian)	-10, 40, 26	-10, 40, ±26
large	variable (spherical)	sphere of radius 60 cm	

Table 3.9. Kernel dimensions and extents.

Figure 3.14 shows the total energy deposited within the six kernel categories (total, primary, first-scatter, second-scatter, multiple-scatter, and B&A) as a function of kernel size for monoenergetic photon beams of 1.25 Mev (Figure 3.14a) and 5.0 Mev (Figure 3.14b). These data may be used to determine the percentage of energy deposited by the various orders of scattered photon as a function of the physical scope of the kernel. We suggest that energy losses should be kept as low as is reasonably achievable (ALARA), in order to accurately represent the energy spread, while achieving acceptable dose calculation times. As suggested by Mackie (1984), it may be beneficial to use different kernel extents for the different kernel types. It may be faster to do several convolutions at moderate spatial resolution than to do a single convolution at fine resolution.
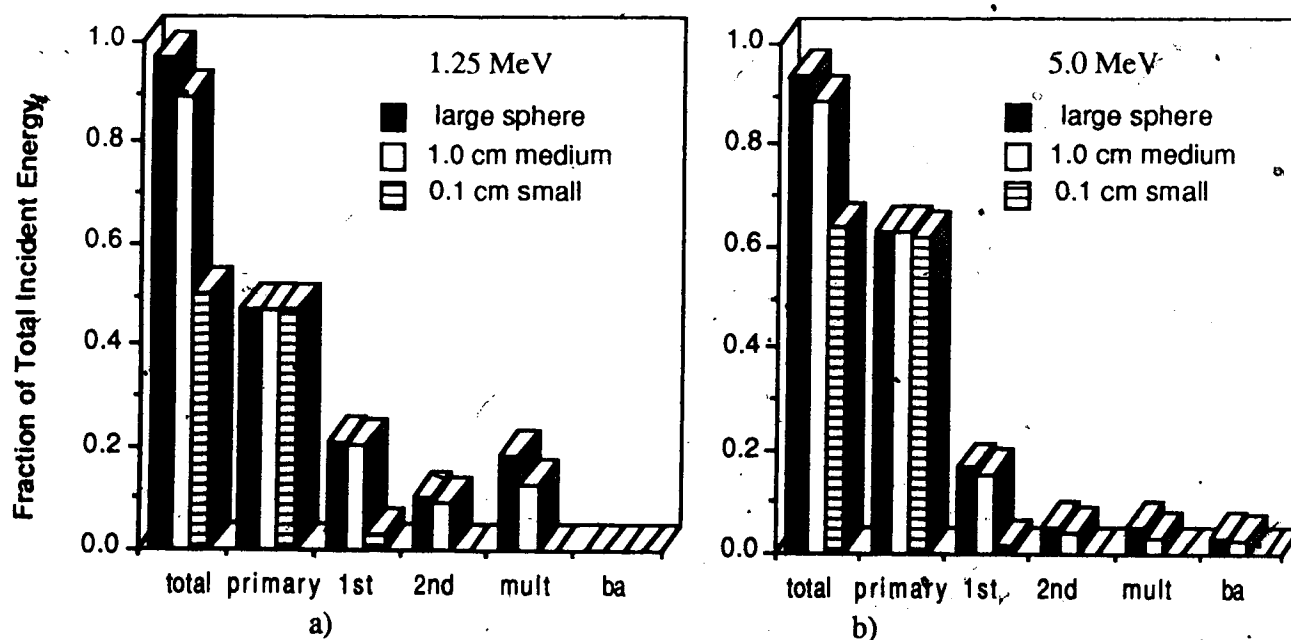
Figure 3.14. Percentage of incident photon energy deposited versus kernel size for (a) 1.25 Mev photons, and (b) 5.0 Mev photons.

The energy escaping from each kernel extent is summarized in Table 3.10 for both 1.25 Mev and 5.0 MeV incident photons.

	incident photon energy	
kernel size	1.25 MeV	5.0 MeV
small	49.9%	36.8%
medium	11.2%	11.7%
large	3.1%	6.2%

Table 3.10. Percentage of incident energy loss as a function of kernel extent.

To be 'conservative', we can recommehd the following kernel extents in order to model the deposition of energy in a water medium.

	Incident Photon Energy	
kernel type	1.25 MeV	5.0 MeV
primary	small	small to medium
first-scatter	medium	medium
second-scatter	medium	medium
multiple-scatter	medium large	medium
brem&annih	ignore	medium

Table 3.11. Recommended kernel extents to minimize energy loss.

In some specific situations, greater energy leakage from a specific kernel type may be tolerable, depending on its relative contribution to the total dose in a particular region of interest (see section §4.2 where an accurate dose calculation is performed in the "build-up" region despite significant energy loss.)

3.3.6, Spatial Resolution versus Voxel Size

Once the kernel extent has been set, the selection of the voxel size determines the number of kernel voxels required. The spatial resolution required depends upon the situation being modelled. In regions of large dose gradients (e.g. the 'build-up region' of megavoltage photon beams), it will be necessary to use a smaller voxel size than in regions of low dose gradients.

Figure 3.15 illustrates how the details contained in the 5.0 MeV total kernel are affected by the kernel voxel size. The black and white images displayed in Figure 3.15 do not have the colour legend indicating relative pixel values. These figures were generated instead by using a "window" and "level" approach. The "window" defines the total range of values over which the entire gray scale will be mapped and the level indicates the intensity value corresponding to the middle of the window. For example, if an image has values which range from -1000 to +2000 (as CT images do), and the level and window were set to 0 and 1000 respectively, then pixels with a value of 500 and above would be pure white and pixels with a value of -500 or less would be black. All the other possible shades of gray would be evenly distributed from -500 to 500. In this work, the level and window settings will be indicated by L/W. The range of values for all black and white images in this work are -1000 to +2000.
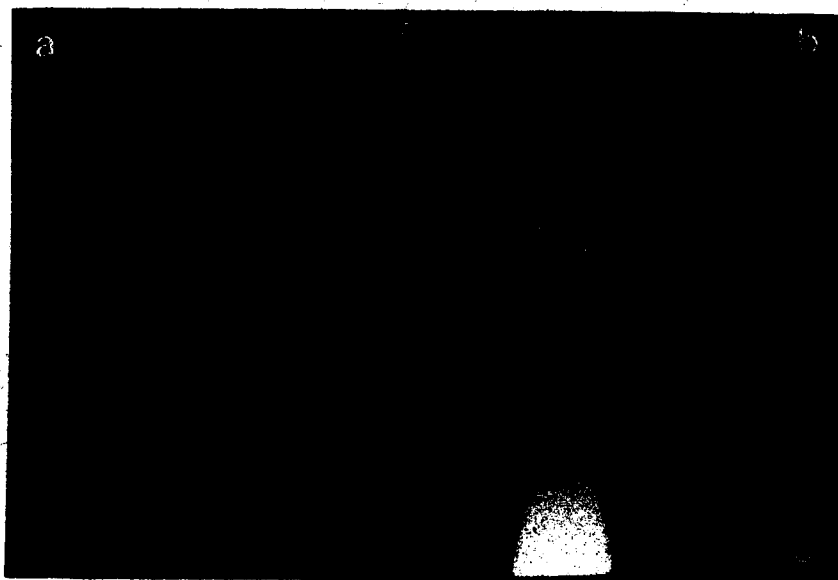
Figure 3.15. Variation of the details of 5.0 MeV total kernel with voxel size
a) 1 cm voxel edge length (L/W = -1000/70)
b) 0.1 cm voxel edge length (L/W = -1000/70)
c) 0.01 cm voxel edge length (L/W = -1000/70)

3.4 Discrete Convolutions and the Reciprocity Theorem

This section expresses the convolution integral in two forms suitable for numerical

evaluation: as a summation, and as a matrix operation. A reciprocity relationship is

discussed as it relates to the evalution of these two representations.

3.4.1 Discrete Convolutions

Replacing the integration over s (i.e. the spatial extent of the kernel) in equation

3.5b with an appropriate summation, we can write the continuous convolution integral as a

discrete 3D summation:

$$
D(n_1,n_2,n_3) = \sum_{m_1=-edge}^{edge} \sum_{m_2=-edge}^{edge} \sum_{m_3=top}^{bottom} \Phi(n_1-m_1,n_2-m_2,n_3-m_3)\, G(m_1,m_2,m_3)
$$

$$(3.10)$$

where

- $D(n_1,n_2,n_3)$ is the dose to the pixel located at (n_1,n_2,n_3) with respect to the phantom origin
- $\Phi(n_1,n_2,n_3)$ is the fluence at the pixel located at (n_1,n_2,n_3) with respect to the phantom origin
- $G(m_1,m_2,m_3)$ is the kernel representing the energy distribution relative to the kernel origin per incident photon

The fluence and kernel must be selected for the same incident photon energy. The voxel size for the fluence, kernel, and dose elements must also be the same.

Using a kernel compressed to 2D and 1D, equation 3.10 reduces to equations 3.11a

and 3.11b,respectively.

$$
D(n_1,n_3) = \sum_{m_1=-edge}^{edge} \sum_{m_3=top}^{bottom} \Phi(n_1-m_1,n_3-m_3)\, G(m_1,m_3) \qquad (3.11a)
$$

$$
D(n_3) = \sum_{m_3=top}^{bottom} \Phi(n_3-m_3)\, G(m_3) \qquad (3.11b)
$$

As a simple example, let us calculate the dose along the central axis of a uniform

broad beam irradiating an infinite homogeneous medium. Assume, that a 1D kernel with

dimensions top=-1 and bottom=2 is adequate to model the situation, and that we would like

the dose to four points. The components of the dose, fluence, and kernel arrays are shown

in Figure 3.16. Note that the fluence must be known at points upstream from the dose

points.

$$\Phi(n) \ \& \ D(n) \qquad\qquad G(m)$$
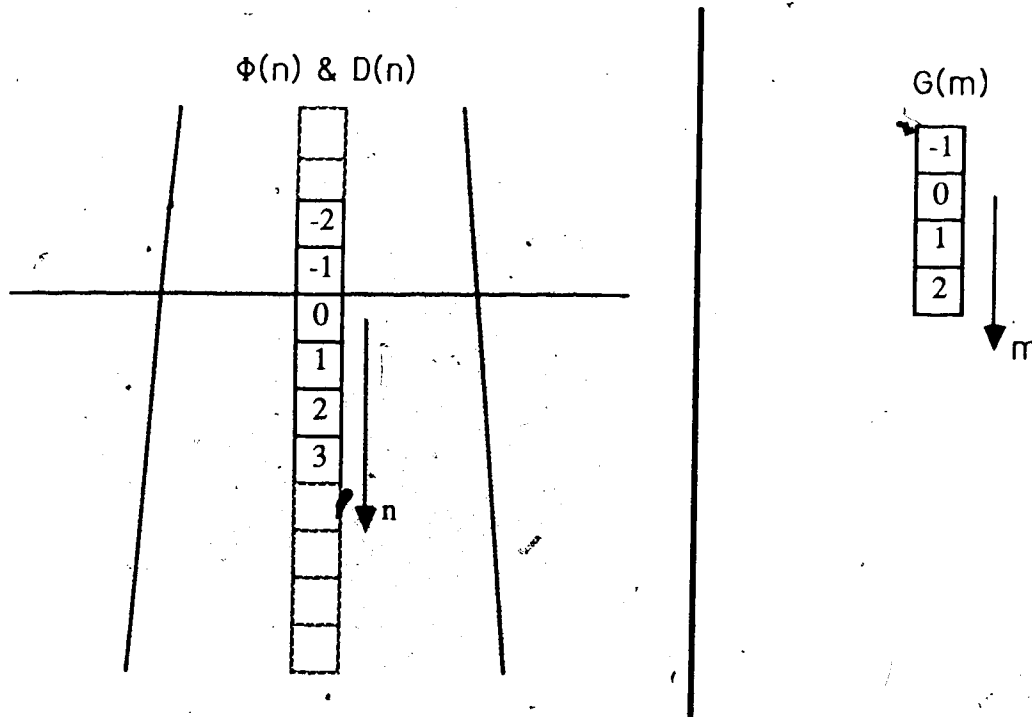
Figure 3.16. Representation of $D(n_3)$, $\Phi(n_3)$, and $G(m_3)$.

Substituting the values for 'top' and 'bottom' in equation 3.11b we can determine

the dose to the four points as shown below.

$$D(n_3) = \sum_{m_3=-1}^{2} \Phi(n_3-m_3)\, G(m_3) \qquad\qquad (3.12)$$

$$
\begin{aligned}
D(0) &= \Phi(1)G(-1) + \Phi(0)G(0) + \Phi(-1)G(1) + \Phi(-2)G(2)\\
D(1) &= \Phi(2)G(-1) + \Phi(1)G(0) + \Phi(0)G(1) + \Phi(-1)G(2)\\
D(2) &= \Phi(3)G(-1) + \Phi(2)G(0) + \Phi(1)G(1) + \Phi(0)G(2)\\
D(3) &= \Phi(4)G(-1) + \Phi(3)G(0) + \Phi(2)G(1) + \Phi(1)G(2)
\end{aligned}
$$

These equations can be interpreted from two viewpoints: the energy distribution (or 'pitcher') point of view, or the energy reception (or 'catcher') point of view (Mackie 1984). The connection between these two view points is a consequence of the reciprocity theorem of radiation transport.

3.4.2 The Reciprocity Theorem

The reciprocity theorem (which is exact only in an infinite homogeneous medium) states that for the attenuation of radiation, "reversing the positions of a point detector and point source does not change the amount of radiation detected" (Attix 1986, pg 55). This is illustrated in Figure 3.17. If media I and II are identical, then switching the location of the point source and the particle detector will NOT alter the number, direction , or energy of any of the particles detected.

If media I and II differ, switching the detector and source will not alter the *primary particles* detected since the overall attenuation along the path has not changed. However, the *scattered particles* reaching the detector may change. Even though the reciprocity theorem is not exact for an inhomogeneous medium, it is still useful if the primary radiation dominates, or if the transport of secondary particles does not vary greatly in the different media.
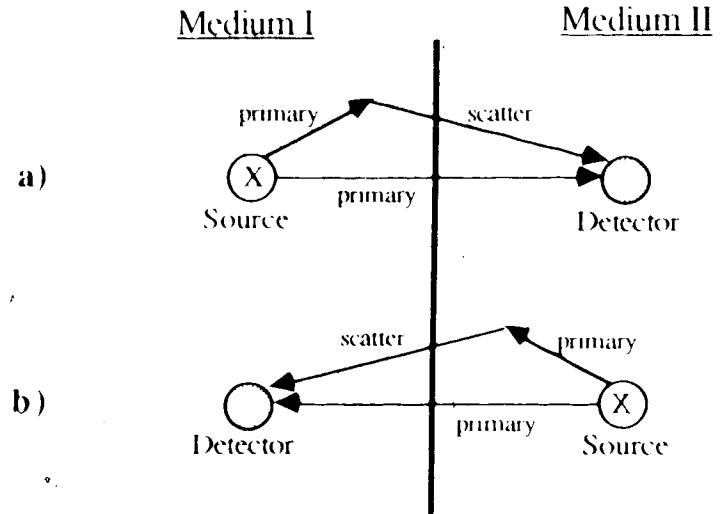
Figure 3.17. The reciprocity theorem.

In our present case of an infinite homogeneous medium, the reciprocity theorem applies and suggests that an interaction voxel and an energy deposition voxel may have their roles reversed. Previously, all kernels were illustrated with one interaction pixel and many energy deposition pixels. By reciprocity, the kernels also represent how a unit impulse of primary photons at each of the 'deposition' voxels deposit energy in the 'interaction' voxel.

We now return to the interpretation of equation 3.12 and the 'catcher' and 'pitcher' point of view. From the pitcher's point of view (see Figure 3.17) we imagine a primary photon impulse at the interaction voxel (G(0) in the kernel) causing energy to be distributed 'mainly downstream' to dose deposition voxels. The energy deposited is weighted according to the "intensity" of the incident primary photon fluence. The kernel is shifted downstream so that G(0) lands on all interaction sites. For each interaction site, the kernel is reweighted according to the intensity of the primary photon fluence at the interaction site, and the energy is distributed to each destination voxel (i.e. a dose point). Once the kernel element G(0) has 'landed' on all possible interaction voxels, the energy distribution process is complete. Figure 3.18 illustrates this for determining the dose to one voxel.

Fluence   Kernel   Dose point

X ——— G(-1)
Φ(n-2) ——— X ——— G(0)
Φ(n-1)   X ——— G(1)
Φ(n)   X ——— G(2) ——— ▶ D(n)
Φ(n+1)

1st contribution to D(n):
Φ(n-2) G(2)

Φ(n-2)   X ——— G(-1)
Φ(n-1) ——— X ——— G(0)
Φ(n)   X ——— G(1) ——— ▶ D(n)
Φ(n+1)   X ——— G(2)

2nd contribution to D(n):
Φ(n-1) G(1)

Φ(n-2)
Φ(n-1)   X ——— G(-1)
Φ(n) ——— X ——— G(0) ——— ▶ D(n)
Φ(n+1)   X ——— G(1)
          X ——— G(2)

3rd contribution to D(n):
Φ(n) G(0)

Φ(n-2)
Φ(n-1)
Φ(n)   X ——— G(-1) ——— ▶ D(n)
Φ(n+1) ——— X ——— G(0)
          X ——— G(1)
          X ——— G(2)

4th contribution to D(n):
Φ(n+1) G(-1)
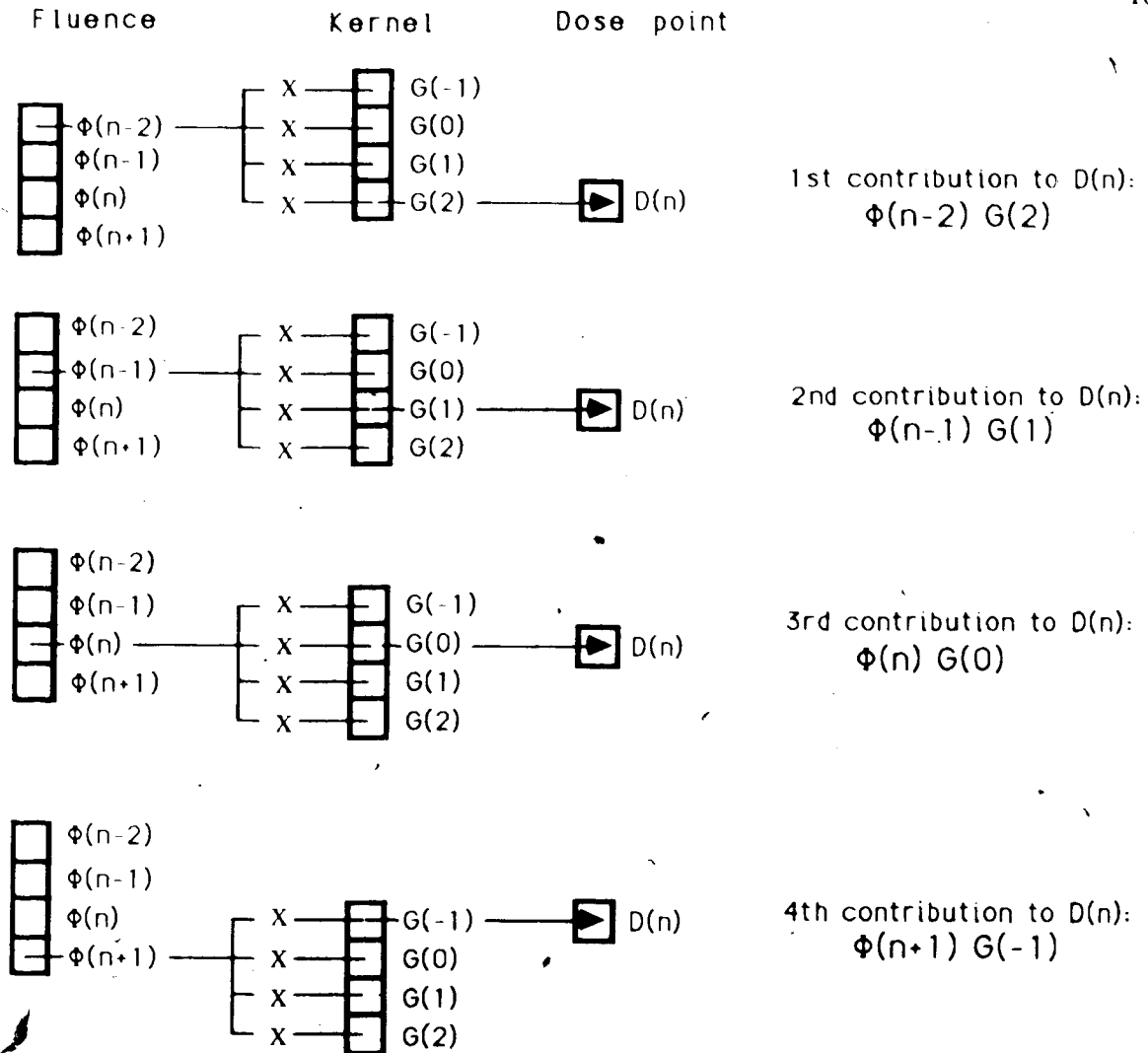
$$D(n) = \sum_{m=-1}^{2} \Phi(n-m)\, G(m)$$

Fix m, cycle n, repeat

Figure 3.18. The "pitcher" representation of convolution. The kernel shifts downward so that G(0) lands on each impulse point (Φ). The dose is received in an incremental fashion at D.

From the catcher's point of view (Figure 3.19), we look mainly 'upstream' to see which interaction sites can contribute dose to the voxel of interest. This retroviewing

requires inverting the kernel $(z \rightarrow -z)$ to determine which voxels are "within range" of

contributing. Again, the contribution is weighted according to the primary photon fluence

at each contributing interaction point. From a mathematical viewpoint, reciprocity is simply

a consequence of the commutative properties of multiplication and addition (Equation

3.12).

,Dose point	Inverted Kernel		Fluence	'	Contribution
	G(2) —— X		$\Phi(n-2)$		$G(2)\Phi(n-2)$
	G(1) —→ X		$\Phi(n-1)$		$G(1)\Phi(n-1)$
D(n)	G(0) —— X		$\Phi(n)$	·	$G(0)\Phi(n)$
	G(-1) —— X		$\Phi(n+1)$		$G(-1)\Phi(n+1)$

$$D(n) = \sum_{m=-1}^{2} G(m)\, \Phi(n-m)$$

fix n, cycle m
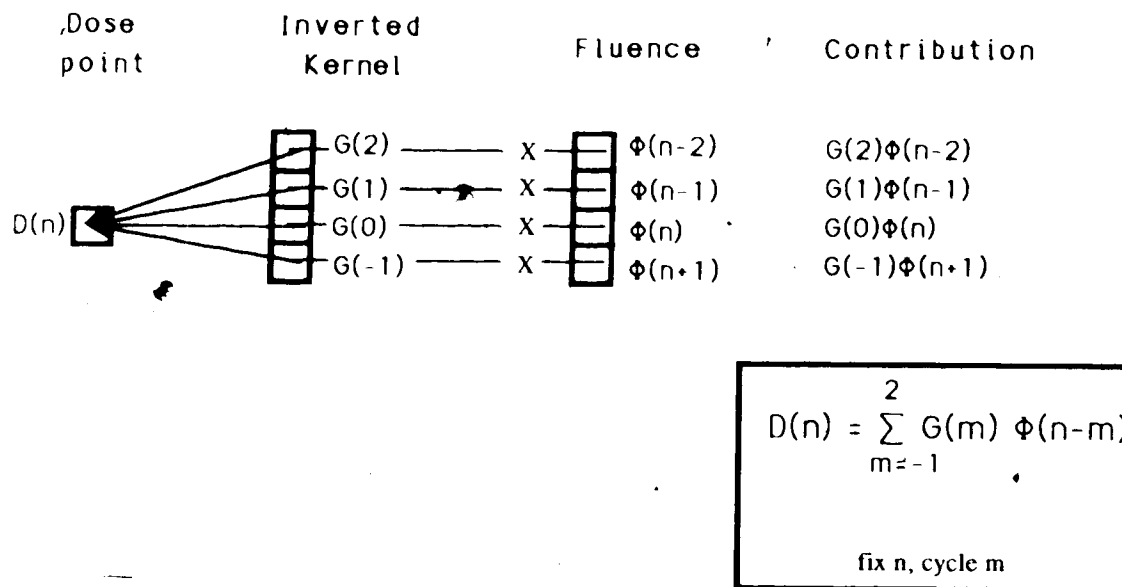
Figure 3.19. The "catcher" representation of convolution. The kernel is inverted and G(0) placed on the dose point (D). The kernel - fluence values are multiplied in pairs to yield the dose at D directly.

The pitcher's forward approach builds up the dose to all dose points in an

incremental fashion; while the catcher's reverse approach determines the total dose to a

single point directly. In either representation, the resulting complete dose distribution will

be identical in a homogeneous infinite medium.

An interesting physical interpretation links the reciprocity theorem and dose

measurement. If we are interested in calculating the dose along the central axis for a broad

beam then we can perform the calculation in one of two manners. We can perform a full

3D convolution (using the pitcher approach) and then extract dose along the central axis; or

we can use the catcher approach and determine the dose along the central axis. This is

analogous to measuring an identical dose for either a small detector in a broad beam or a

'pancake' detector in a pencil beam as illustrated in Figure 3.20 (Nahum 1986).
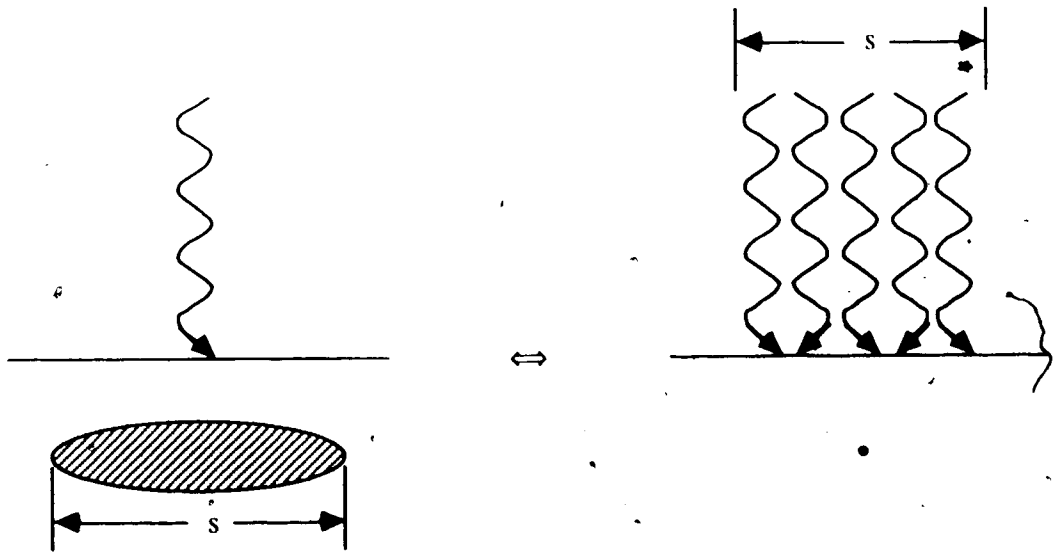
Figure 3.20. The Reciprocity theorem in action.

3.4.3 A Matrix Representation

Another method of determining a dose distribution is through a matrix

multiplication[6].

$$[D] = [G] [\Phi] \qquad\qquad (3.13)$$

where

    [D] is an N element column matrix representing the dose to N points

    [G] is an N x M matrix representing the kernel

    [Φ] is an M element column matrix representing the fluence

---

[6]A similar matrix formalism is used routinely in deconvolving measured spectral distributions to obtain the

true spectrum (Skarsgard et.al., 1961)

Using the previous 1D example, the matrix contents are written in detail to illustrate the matrix formalism.

$$
\begin{bmatrix} D(0) \\ D(1) \\ D(2) \\ D(3) \end{bmatrix} = \begin{bmatrix} G(2) & G(1) & G(0) & G(-1) & 0 & 0 & 0 \\ 0 & G(2) & G(1) & G(0) & G(-1) & 0 & 0 \\ 0 & 0 & G(2) & G(1) & G(0) & G(-1) & 0 \\ 0 & 0 & 0 & G(2) & G(1) & G(0) & G(-1) \end{bmatrix} \begin{bmatrix} \Phi(-2) \\ \Phi(-1) \\ \Phi(0) \\ \Phi(1) \\ \Phi(2) \\ \Phi(3) \\ \Phi(4) \end{bmatrix}
$$

(3.14)

The dose matrix consists of all those points in the dose distribution. The fluence matrix is established by considering the dimensions of both the kernel and the dose matrix (since the fluence must be known at points upstream of the dose points). In this example, the kernel dimensions are top=-1 and bottom=2, and the dose matrix dimensions range from 0 to 3. Using the catchers point of view, we see that the elements required in the fluence matrix range from 'bottom' pixels upstream of D(0) to '-top' pixels downstream of D(3); that is $\Phi(-2)$ to $\Phi(4)$. The determination of the kernel matrix is a little more difficult. The number of rows in the kernel matrix matches the number of rows in the dose matrix; the number of columns in the kernel matrix matches the number of rows in the fluence matrix. The elements making up the kernel matrix can be interpreted in two manners, again through the reciprocity theorem.

From the 'pitchers' viewpoint, the *columns* of the kernel matrix represent the energy deposited by a primary photon impulse at an interaction site. The first column of the kernel matrix represents the first contribution from any interaction site to one of the dose points in question. The second column contains the kernel shifted one voxel downstream from the interaction pixel of the first column. The kernel is shifted downstream until it no longer contributes energy to the selected dose points. The locations

of the interaction sites for each column given in the fluence coordinate system are: $\Phi(-2)$, $\Phi(-1)$, $\Phi(0)$, $\Phi(1)$, $\Phi(2)$, $\Phi(3)$, $\Phi(4)$.

From the 'catchers' viewpoint, the *rows* of the kernel matrix represent the inverted kernel. The first row contains a left justified inverted kernel. The second row contains the kernel shifted one voxel to the right. This process is carried out until the kernel reaches the right limit. In matrix multiplication, a row from the kernel matrix is multiplied by the column of the fluence matrix and this yields the total dose to one voxel - the catcher!

In this example, we saw that a 1D dose distribution required a 2D kernel matrix. It can be shown that a 2D dose distribution requires a 4D kernel matrix, and a 3D dose distribution requires a 6D kernel matrix! Much of the information in the kernel matrix is redundant (one row contains the same information as the next except for shifting one position). Thus, the convolution formalism is a more concise method of expressing the same mathematical operations.

Now that we have the basics of the convolution method, Chapter 4 will present results of 2D convolutions.

Chapter 4

Convolutions

Man is a tool-using animal...

Without tools he is nothing, with tools he is all.

Anonymous

4.0   Convolutions

In this chapter we will actually calculate dose distributions by evaluating the convolution integral in both real space and Fourier space. Section §4.1 will calculate, in real space, a central axis depth dose curve (1D) and a planar dose distribution (2D) for a broad beam of incident photons. Section §4.2 will briefly explain Fourier transforms, fast Fourier transforms (FFTs) and use these to calculate the dose resulting from the same beam of incident photons. Section §4.3 will examine the accuracy and speed of the convolutions, in real and Fourier space. Each of the assumptions required by the convolution method are individually discussed in section §4.4 and possible 'work-arounds' are explored.

4.1   Real Space Convolutions

Figure 4.1 illustrates the steps required to perform a convolution in real space. As mentioned previously (§3.3.2), the preliminary steps of reading a spherical kernel and

```
┌─────────────────────────┐
│   Read Spherical Kernel  │
└─────────────────────────┘
            │
            ▼
┌─────────────────────────┐        ┌─────────────────────────┐
│ Generate Cartesian Kernel│        │   Calculate Fluence      │
└─────────────────────────┘        └─────────────────────────┘
            │                                   │
            ▼                                   ▼
   ████████████████████████████████████████████████
   █   Perform a Real Space Convolution           █
   ████████████████████████████████████████████████
                        │
                        ▼
                  ⎛   Dose      ⎞
                  ⎝ Distribution⎠
```
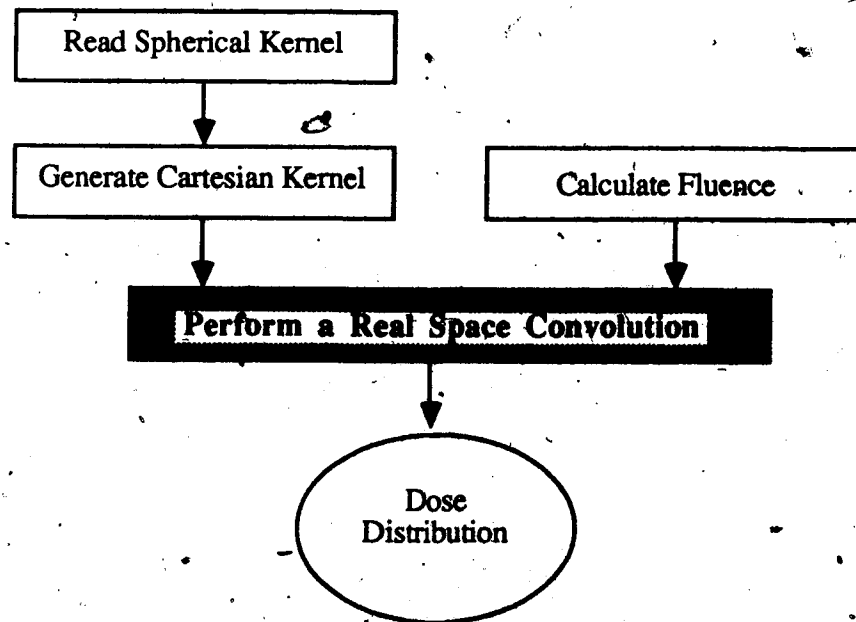
Figure 4.1. Steps involved in real space convolutions.

generating the Cartesian kernel could be done in advance and stored for anticipated voxel sizes. The fluence is calculated as described in section §3.2.4 and the real space convolution is then performed.

The real space convolution calculation time is proportional to the number of multiplications performed, which is determined by the kernel and fluence array sizes. The 3D convolution of a kernel of size $(M_1.M_2.M_3)$, with a fluence of size $(N_1.N_2.N_3)$ results in a dose array size $(M_1+N_1-1, M_2+N_2-1, M_3+N_3-1)$ (as depicted in Figure 4.2 for the 2D case). Every element in the kernel is multiplied by every element in the fluence matrix; therefore $M_1M_2M_3N_1N_2N_3$ multiplications are performed. The 3D convolution calculation time is thus proprotional to $M_1M_2M_3N_1N_2N_3$. Similarly, 2D convolution calculation times are proprotional to $M_1M_2N_1N_2$; and 1D convolution times are proportional to M_1N_1.
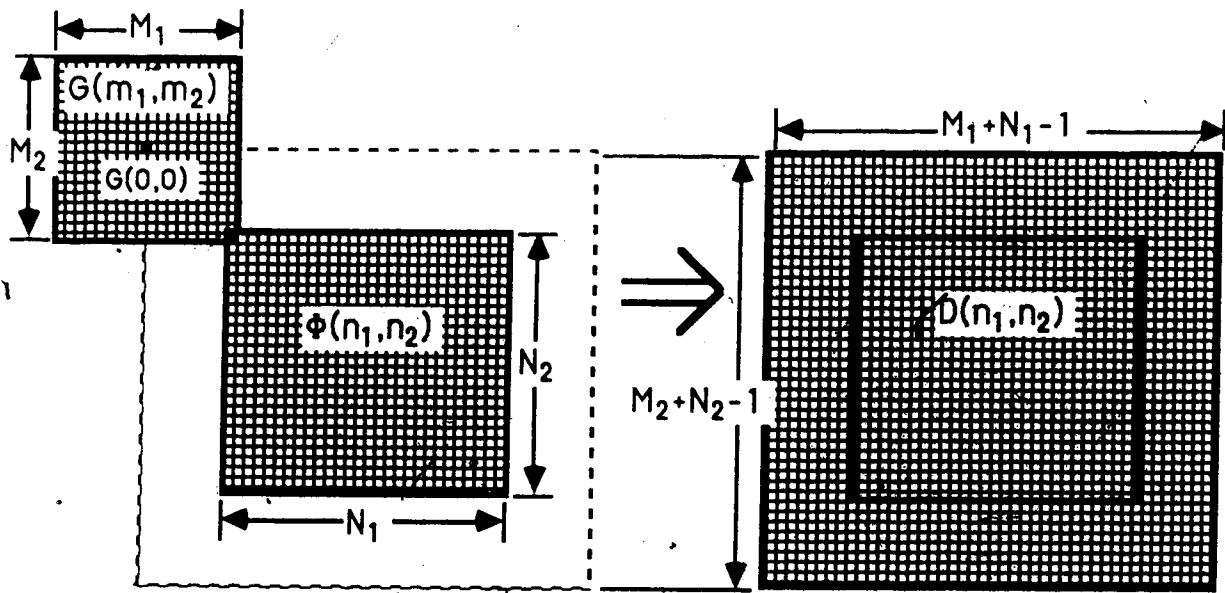
Figure 4.2. The dependence of the dose matrix size on the fluence and kernel matrices.

As a simple example of a 2D convolution, consider the two arrays depicted in Figure 4.3. Evaluation of equation 3.11 yields the result as shown.

$$\Phi(n_1,n_2)= \begin{bmatrix} 1 & 0 \\ 2 & 1 \end{bmatrix} \ ; \quad G(m_1,m_2)= \begin{bmatrix} 1 & 0 \\ 1 & 1 \end{bmatrix} \ ; \quad \Phi(n_1,n_2) \circledast G(m_1,m_2) = \begin{bmatrix} 1 & 0 & 0 \\ 3 & 2 & 0 \\ 2 & 3 & 1 \end{bmatrix}$$

Figure 4.3. Numerical example of a 2D convolution in real space.

In practice, there are other considerations which also influence the overall calculation time.

- the computer address space may limit the array size which can be used at any one time. Fragmentation of large arrays may be needed (e.g 16 bit computers).

- the mechanism for addressing computer memory may become a significant factor. For example, on a "virtual address" processor (e.g. DEC's VAX), access to "pages" of memory on disk may require significant time. To minimize this, it may be necessary to "lock pages in memory".

The above indentify time penalties, but time savings are also possible:

- if the dose is to be computed everywhere in a patient, then the fluence array size can match the dose array size (i.e. patient size). This means that those steps of the convolution process which deposit energy outside the patient can be eliminated. This may amount to significant time savings (see Appendix A).

4.1.1 A One Dimensional Example

As a simple example of the convolution algorithm, let us calculate the central axis depth dose curve resulting from a beam of 1.25 MeV photons for a field size of 10x10 cm^2. We wish to calculate the dose to the center of each voxel whose edge length is 0.1 cm

in order to resolve the "build-up" portion of the curve. The primary photon fluence (Figure 4.4a) at the centre of each voxel is calculated from

$$\Phi(n) = \Phi_0 \, e^{-0.1\mu(n+1/2)}$$ (4.1)

where

μ is 0.0632 cm^{-1} for 1.25 MeV photons

$\Phi(n)$ appears linear over our depth range of interest since $e^x \approx 1 + x$, for small x values. In our case, x ranges from only -0.00316 to -0.06004, making $\Phi(k)$ appear linear in Figure 4.4a.

A Cartesian kernel was generated which contained cubic voxels of linear dimensions 0.1 cm and kernel dimensions of: top=-5, bottom=20, edge=50. The 1D kernel shown in Figure 4.4b was obtained from a compression of the 3D total kernel (section §3.3.3). The total of all the element values in this kernel is 0.493, i.e. 49.3% of the incident 1.25 MeV photon energy is deposited within the spatial extent of this small kernel. This value is only marginally larger than the contribution from the primary kernel (46.9% - see section §3.3.1) because the secondary radiation deposit dose well beyond the extent of this kernel. This is one situation in which a large energy leakage does not affect the accuracy of the calculated result, since the leaked energy does not contribute much to the point of interest (i.e. in the build-up region). If the dose at larger depths is of interest, then this energy leakage will affect the accuracy of the calculated result.

Assuming that all conditions are met to allow the use of the convolution technique (§3.2.4), equation 3.11b can be used to perform the convolution. The resultant "build up" curve is shown in Figure 4.4c. Voxel number 4, which corresponds to a mean depth of 4.5 mm, contains the maximum dose. This corresponds well with the "standard" depth of maximum dose of 5.0 mm for Cobalt-60 radiation. This is good agreement considering the incident spectrum of photons and contaminant electrons were ignored (Mackie 1984, Leung et.al. 1976). Measured data from Leung et.al. (1976) is shown for comparison (the dashed line).

0.997	Φ(0)
0.991	Φ(1)
0.984	Φ(2)
0.978	Φ(3)
0.972	Φ(4)	a)
0.966	Φ(5)
0.960	Φ(6)
0.954	Φ(7)
0.948	Φ(8)
0.942	Φ(9)

$\otimes$

.0030	G(-1)
.1413	G(0)
.1852	G(1)
.1109	G(2)
.0370	G(3)
.0050	G(4)	b)
.0021	G(5)
.0020	G(6)
.0020	G(7)
.0020	G(8)
.0020	G(9)

=

measured
calculated

0.305	D(0)
0.695	D(1)
0.924	D(2)
0.996	D(3)
1.000	D(4)	c)
0.999	D(5)
0.998	D(6)
0.996	D(7)
0.995	D(8)
0.987	D(9)
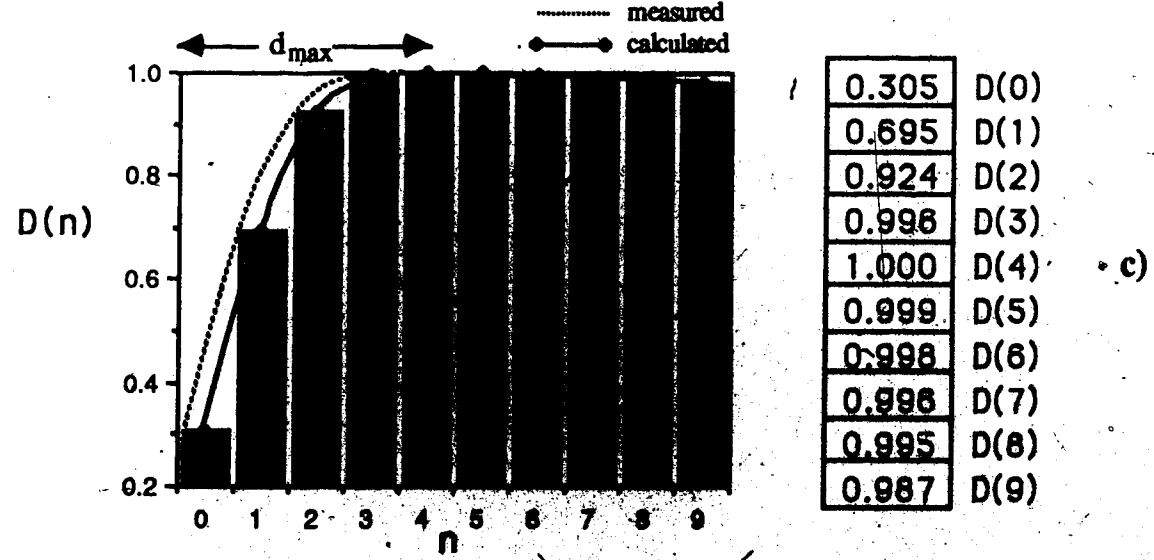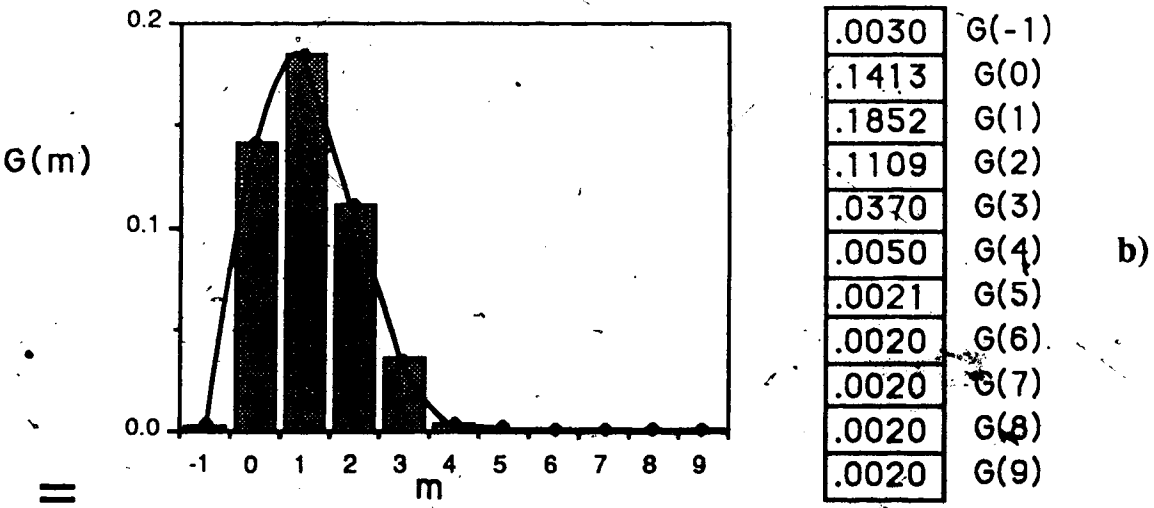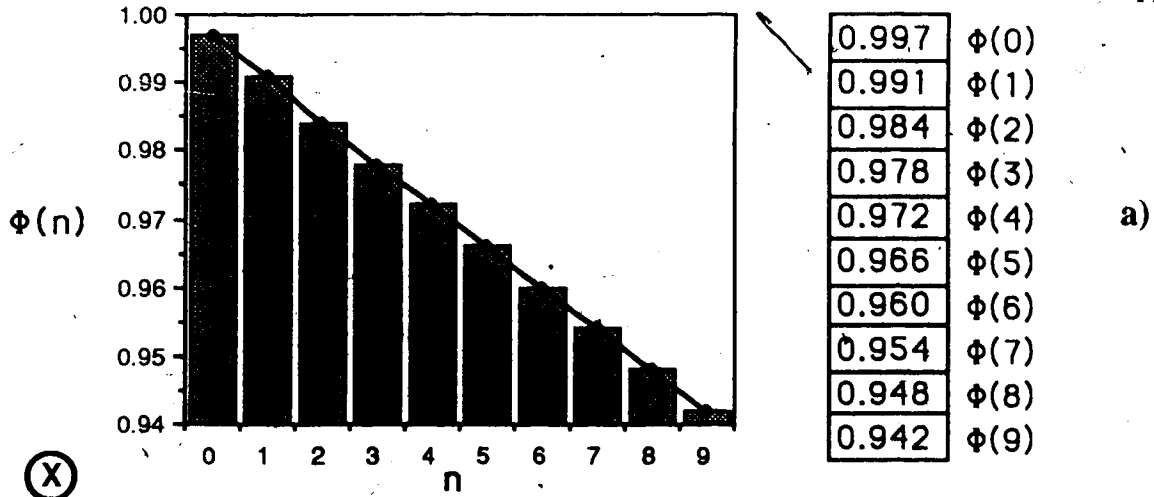
Figure 4.4. A 1D dose distribution calculated in real space for a 1.25 MeV photon beam.
a) Primary Photon Fluence   b) Convolution Kernel   c) Depth Dose Curve

4.1.2   A Two Dimensional Example

The one dimensional example just completed is instructive but we are generally

more interested in calculating the dose to a two dimensional area or a three dimensional

volume. This section deals with the calculation of a 2D dose distribution resulting from a

5.0 MeV incident photon beam for a field size of 10x10 cm^2. The kernel used in the

calculation contained cubic voxels of linear size 0.5 cm and dimensions of top=-10,

bottom=40, and edge=26 . The convolution and kernel compression assumptions have

been met which allows us to perform a 2D convolution. Figure 4.5 shows the kernel

(4.5a), fluence (4.5b), and the resultant dose distribution (4.5c).

Figure 4.5. A 2D dose distribution calculated in real space for a 5.0 MeV photon beam.
a) 5.0 MeV total kernel   b) 5.0 MeV primary fluence   c) resulting dose distribution

The calculation times required to perform these convolutions determine the clinical

applicability of this algorithm. A series of 2D convolutions were performed with various

dose matrix sizes and various kernel sizes (see Table 4.1). Figure 4.6 summarizes the

calculation times required to perform these 2D convolutions. Dose was calculated only in

the area covered by the fluence array (i.e. energy was not deposited beyond the phantom where we don't require a knowledge of the dose).

Dose and Fluence Array Size
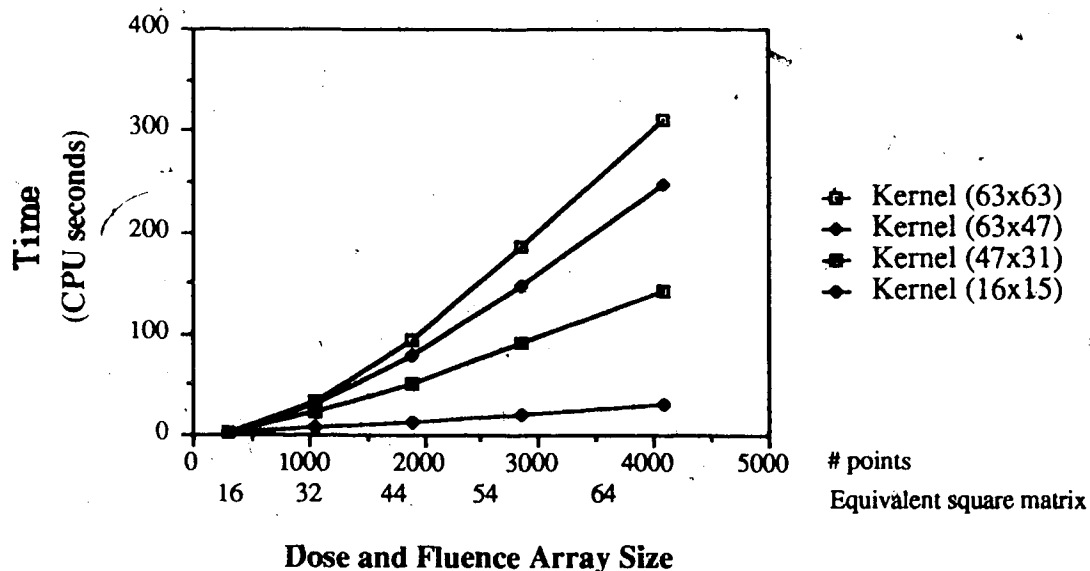
Figure 4.6. Calculation times for real space 2D convolutions. The dose and fluence matrices are of identical size, and the kernel matrix size varies. The times to convert from a spherical kernel to a Cartesian kernel have *not* been included in these times (see §3.3.2).

Using Appendix A, we can determine the reduction in the number of multiplications achieved by this "constrained convolution" as compared to a "full" convolution. Table 4.1 incorporates this reduction in the number of multiplications and shows the average CPU time taken to compute the energy contribution from each kernel voxel to each dose point. This calculation time should remain constant (ignoring "page faults"). This is seen to be the case, and the average calculation time per kernel point per dose point on a VAX-11/780 is 36.6 CPU μseconds. This value can be used to determine the real space calculation time as a function of kernel and fluence matrix size.

Kernel Size (pixels)	top (pixels)	bottom (pixels)	edge (pixels)	time / point (CPU μseconds)
63x63	-15	47	31	36.7
63x47	-13	50	23	37.3
47x31	-10	36	15	35.9
16x15	-3	12	7	36.5

Table 4.1. Average calculation time per kernel point per dose point for a 64^2 matrix.

4.2 Fourier Space

In an effort to reduce calculation times for the convolution algorithm, it has been suggested (Ahnesjö 1984, Boyer 1984, Mackie 1984, Mohan and Chui 1987), that transform techniques be applied to the dose calculation problem. A transformation to another space often simplifies solutions (e.g. logarithm space reduces multiplication to addition). Fourier transformations are appropriate in our case since a convolution in real space is equivalent to a multiplication in Fourier space. Before dealing with convolutions in Fourier space (§4.3), let us first examine:

- the Fourier transforms of some basic 1D functions (§4.2.1)
- the Discrete Fourier Transform (DFT) (§4.2.2)
- the Fast Fourier Transform (FFT) method of evaluating a DFT (§4.2.3)

4.2.1 Continuous Fourier Transforms (1D)

In this work, the functions dealt with are functions of spatial location (e.g. a kernel function $K(m_1,m_2)$ describes the energy deposited in the voxel located m_2 pixels downstream of and m_1 pixels lateral to the interaction site). The following section will deal exclusively with functions of time and their corresponding transforms (functions of frequency), because of the ease in developing and explaining the Fourier transform. The following discussions apply equally well to functions of spatial location and their corresponding transforms, which are functions of spatial frequency (e.g. the Fourier transform of the spatial function, $K(m_1,m_2)$, represents the kernel information in terms of the spatial superposition of sinusoidal variations in energy deposition). Now let us turn our attention to real space time functions, and Fourier space frequency functions.

The Fourier transform of a continuous function, $\mathcal{F}\{ h(t) \}$, is defined in equation 4.2a; the inverse transform, $\mathcal{F}^{-1}\{ H(f) \}$, is defined by equation 4.2b.

$$\mathcal{F}\{h(t)\} = H(f) = \int_{-\infty}^{\infty} h(t)\, e^{-j2\pi ft}\, dt \qquad (4.2a)$$

$$\mathcal{F}^{-1}\{H(f)\} = h(t) = \int_{\infty}^{\infty} H(f)\, e^{j2\pi ft}\, df \qquad (4.2b)$$

$$h(t) \Longleftrightarrow H(f)$$

where

$$j = \sqrt{-1}$$

and the symbol "$\Longleftrightarrow$" denotes h(t) and H(f) as being a Fourier transform pair

We see that the Fourier transform H(f), a function of frequency, represents a function of time, h(t), in terms of the sinusoidal functions of appropriate frequency and amplitude. In general, both 'odd' and 'even' sinusoids will be required to generate h(t) since $e^{j2\pi ft} = \cos(2\pi ft) + j\sin(2\pi ft)$. The 'even' sinusoids are represented by the 'real' component of $e^{j2\pi ft}$ (i.e. real$\{e^{j2\pi ft}\}=\cos\{2\pi ft\}$) and the 'odd' sinusoids are represented by the 'imaginary' component of $e^{j2\pi ft}$ (i.e. img$\{e^{j2\pi ft}\}=j\sin\{2\pi ft\}$). The amplitude of the sinusoids are determined by H(f), also a complex quantity in general:

$$H(f) = R(f) + jI(f) = \|H(f)\|\, e^{j\theta(f)} \qquad (4.3)$$

where

R(f) is the real part of the Fourier transform
I(f) is the imaginary part of the Fourier transform
$\|H(f)\|$ is the amplitude of the Fourier "spectrum" given by $\sqrt{R^2+I^2}$
θ(f) is the phase angle of the Fourier transform and is given by
$\tan^{-1}[I(f)/R(f)]$

As an introduction, let us examine the Fourier transforms of some simple functions.

4.2.1.1 Fourier Transform of Sine and Cosine functions

Let us calculate the Fourier transform of h(t) = $A\sin(2\pi f_0 t)$. $A\sin(2\pi f_0 t)$ may be written as $jA/2\ [e^{-j2\pi f_0 t} - e^{j2\pi f_0 t}]$, then the frequency components of $e^{j2\pi ft}$

required to represent h(t) are located at $-f_0$ and $+f_0$ with imaginary amplitudes of $jA/2$ and $-jA/2$ respectively. This is shown graphically in Figure 4.7a.

Mathematically,

$$\mathcal{F}\{\,h(t)\,\} \quad = H(f) = \int_{-\infty}^{\infty} A\sin(2\pi f_0 t)\, e^{-j2\pi f t}\, dt \qquad (4.4a)$$

$$= \int_{-\infty}^{\infty} jA/2 \,[e^{-j2\pi f_0 t} - e^{j2\pi f_0 t}]\, e^{-j2\pi f t}\, dt \qquad (4.4b)$$

$$= jA/2 \left[\int_{-\infty}^{\infty} e^{-j2\pi(f+f_0)t}\, dt - \int_{-\infty}^{\infty} e^{-j2\pi(f-f_0)t}\, dt \right] \qquad (4.4c)$$

$$= jA/2 \,[\,\delta(f+f_0) - \delta(f-f_0)\,] \qquad (4.4d)$$

Here we have made use of the delta (or impulse) function (Brigham 1974).

$$\delta(f) = \int_{-\infty}^{\infty} e^{j2\pi f t}\, dt \qquad (4.5)$$

In Figure 4.7a, the delta function signifies the "ultra purity" of the sinusoidal function of a single frequency.

Does the inverse transform of H(k) (equation 4.4d) yield the original h(t)? The inverse transform is given by,

$$\mathcal{F}^{-1}\{\,H(f)\,\} \quad = h(t) = jA/2 \int_{-\infty}^{\infty} [\delta(f+f_0) - \delta(f-f_0)]\, e^{j2\pi f t}\, dt \qquad (4.6a)$$

$$= jA/2 \,[e^{-j2\pi f_0 t} - e^{j2\pi f_0 t}] \qquad (4.6b)$$

$$= jA/2 \,[-2j\sin(2\pi f_0 t)\,] \qquad (4.6c)$$

$$= A \sin(2\pi f_0 t) = h(t) \qquad (4.6d)$$

as expected. The transform pairs are represented by

$$h(t) = A\sin(2\pi f_0 t) \quad \Longleftrightarrow \quad H(f) = jA/2 \,[\delta(f+f_0) - \delta(f-f_0)] \qquad (4.7)$$

Similarily, we can find the transform pairs for the cosine function (Figure 4.7b) given by:

$$h(t) = A\cos(2\pi f_0 t) \qquad \Longleftrightarrow \qquad H(f) = A/2 \ [\delta(f + f_0) + \delta(f - f_0)] \qquad (4.8)$$

As expected, the even cosine function has purely real components; and the odd sine function has purely imaginary components.

An interesting feature of the Fourier transform is that the amplitude of the transform describes the 'shape' of the function while the phase describes the temporal positioning of the structure. For example, the amplitude of the transforms of both the sine and cosine function are identical, $\|H(f)\| = A/2[\delta(f + f_0) + \delta(f - f_0)]$. The phase for the sine function however is $\theta(f_0) = -90$, $\theta(-f_0) = 90$; and for the cosine function the phase factors are $\theta(f_0) = \theta(-f_0) = 0$. Thus, the shape of the sine and cosine functions are identical but the phase factor serves to shift the position of the waveforms appropriately in time (see §4.2.1.4 Time shifting).
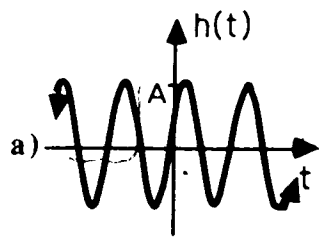
$$h(t) = A\sin(2\pi f_0 t)$$
$$\Longleftrightarrow$$
$$I(f) = A/2 \ [\delta(f + f_0) - \delta(f - f_0)]$$
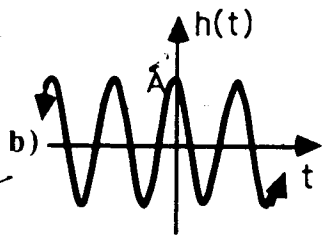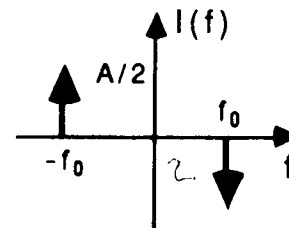
$$h(t) = A\cos(2\pi f_0 t)$$
$$\Longleftrightarrow$$
$$R(f) = A/2 \ [\delta(f + f_0) + \delta(f - f_0)]$$
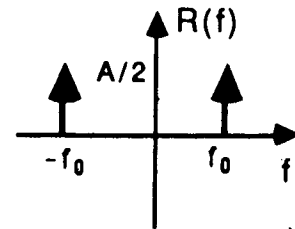
Figure 4.7. Fourier tranform of the sine (a) and cosine (b) functions.

4.2.1.2　Fourier Transform of the Impulse and Constant Functions

Let us now determine the Fourier transform of the impulse function (equation 4.5).

One property of the impulse function is that

$$\int_{-\infty}^{\infty} \delta(t-t_0)\, x(t)\, dt = x(t_0)$$

(4.9)

where

$x(t)$ is an arbitrary function continuous at t_0

The Fourier transform of $h(t) = K\delta(t)$ is easily determined from equations 4.2a and 4.9.

$$H(f) = \int_{-\infty}^{\infty} K\delta(t)\, e^{-j2\pi ft}\, dt = Ke^0 = K$$

(4.10)

This is interpreted to mean that an impulse function in real space is made up of equal contributions from all even sinusoids (cosine) in Fourier space (see Figure 4.8a). Thus the tranform pair for the impulse function is

$$h(t) = K\delta(t) \quad \Longleftrightarrow \quad H(f) = K$$

(4.11)

Let us now examine the Fourier transform of a constant, $h(t) = K$.

$$H(f) = \int_{-\infty}^{\infty} K\, e^{-j2\pi ft}\, dt = K\delta(f)$$

(4.12)

Similarly, this is interpreted to mean that a uniform pattern in real space is represented by sinusoids of zero frequency in Fourier space (Figure 4.8b) since the function is not changing in time. This transform pair is given by:

$$h(t) = K \quad \Longleftrightarrow \quad H(f) = K\delta(f)$$

(4.13)

Note the reciprocity between equations 4.11 and 4.13.

$h(t) = K\delta(t)$

$\Longleftrightarrow$

$H(f) = K$

a)

$h(t) = K$

$\Longleftrightarrow$

$H(f) = K\delta(f)$

a)   b)
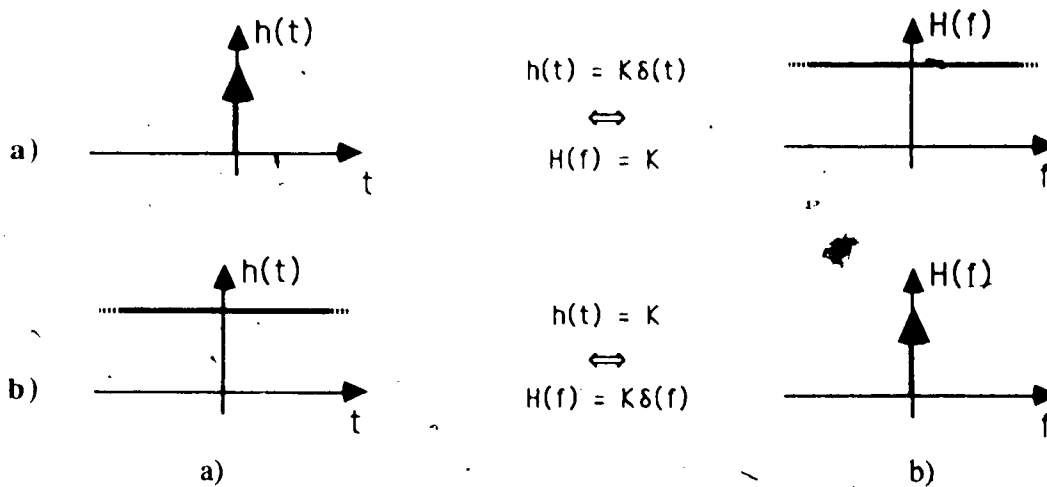
Figure 4.8. Fourier tranform of the impulse (a) and constant (b) functions.

4.2.1.3   Fourier Transform of the Step Function

The last transform to be examined is for the step function, a constant function over a finite time period,

$$h(t) = \begin{cases} A & \|t\| < T_0 \\ A/2 & \|t\| = T_0 \\ 0 & \|t\| > T_0 \end{cases}$$

(4.14)

The Fourier transform is given by

$$H(f) = \int_{-T_0}^{T_0} A\, e^{-j2\pi ft}\, dt$$

(4.15a)

$$= A \int_{-T_0}^{T_0} \cos(2\pi ft)\, dt \;-\; jA \int_{-T_0}^{T_0} j\sin(2\pi ft)\, dt$$

(4.15b)

$$= \frac{A}{2\pi f} \sin(2\pi ft) \Big|_{-T_0}^{T_0}$$

(4.15c)

$$= \frac{2A}{2\pi f} \sin(2\pi f T_0)$$

(4.15d)

$$= 2AT_0 \ \frac{\sin(2\pi f T_0)}{2\pi f T_0} \qquad\qquad (4.15e)$$

Notice that H(f) is purely real and has negative and zero amplitudes at certain "cross-over" frequencies (see Figure 4.9).

$$h(t) \quad =A \quad |t| < T_0$$
$$=A/2 \quad |t| = T_0$$
$$=0 \quad |t| > T_0$$

$$\Longleftrightarrow$$

$$H(f) = 2AT_0 \ \frac{\sin(2\pi T_0 f)}{2\pi T_0 f}$$
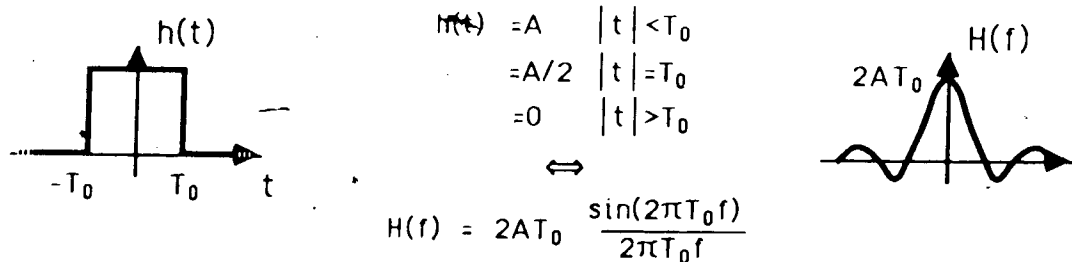
Figure 4.9. Fourier transform of the step function.

4.2.1.4 Properties of the Fourier Transform

The properties of Fourier transforms are well known(Brigham 1974 31-49) and will only be stated here.

	Real domain		Fourier domain	
Linearity	$h(t) + g(t)$	$\Longleftrightarrow$	$H(f) + G(f)$	(4.16a)
Symmetry	$H(t)$	$\Longleftrightarrow$	$h(-f)$	(4.16b)
Time Scaling	$h(kt)$	$\Longleftrightarrow$	$\dfrac{1}{\|k\|} H\left[\dfrac{f}{k}\right]$	(4.16c)
Frequency Scaling	$\dfrac{1}{\|k\|} h\left[\dfrac{t}{k}\right]$	$\Longleftrightarrow$	$H(kf)$	(4.16d)
Time Shifting	$h(t-t_0)$	$\Longleftrightarrow$	$H(f)e^{-j2\pi f t_0}$	(4.16e)
Frequency Shifting	$h(t)e^{-j2\pi f_0 t}$	$\Longleftrightarrow$	$H(f-f_0)$	(4.16f)
Convolution	$h(t) \circledast g(t)$	$\Longleftrightarrow$	$H(f)G(f)$	(4.16g)

4.2.2   Discrete Fourier Transforms

The Fourier transform discussion to this point has only considered continuous 1D functions. In this work, we deal with sampled (or discrete) functions. The procedure of forming a sampled function from a continuous function consists of several intermediate steps (Dudgeon and Mersereau 1984, Brigham 1974) and is briefly summarized here.

Consider a continuous function, $h(t)$, with a corresponding Fourier transform $H(f)$ (Figure 4.10a). Also consider an infinite 'sampling' function ($\Delta_0(t)$), as a series of δ functions with sampling period T [7], and its corresponding Fourier transform (Figure 4.10b). By multiplying the continous function with the sampling function, we can produce a 'sampled' function (see Figure 4.10c). The product, $h(t)\Delta_0(t)$, in real space corresponds to a convolution in Fourier space (Figure 4.10c).

The transform pair of figure 4.10c is not amenable to digital computation since the product $h(t)\Delta_0(t)$ containes a infinite number of samples. A step function or "window" can be used for truncation to a finite series of samples (Figure 4.10d). Multiplication of this step function with $h(t)\Delta_0(t)$ in real space again corresponds to a convolution in Fourier space (Figure 4.10d). This truncation step in real space introduces 'ripples' in the Fourier transform. Making the step function wider (i.e. less truncation) suppresses the ripples in the Fourier space convolution to an acceptable level.

This transform pair is still not useful for digital computation since the transform is continuous. The frequency domain is now sampled with a function as illustrated in Figure 4.10f. The multiplication of this sampling function in Fourier space corresponds to a

---

[7]The Nyquist theory states that a continuous function is uniquely determined by its sampled values, when the waveform is sampled at least twice the maximum frequency contained in the original function, thus preserving the "fidelity" of the transformation.
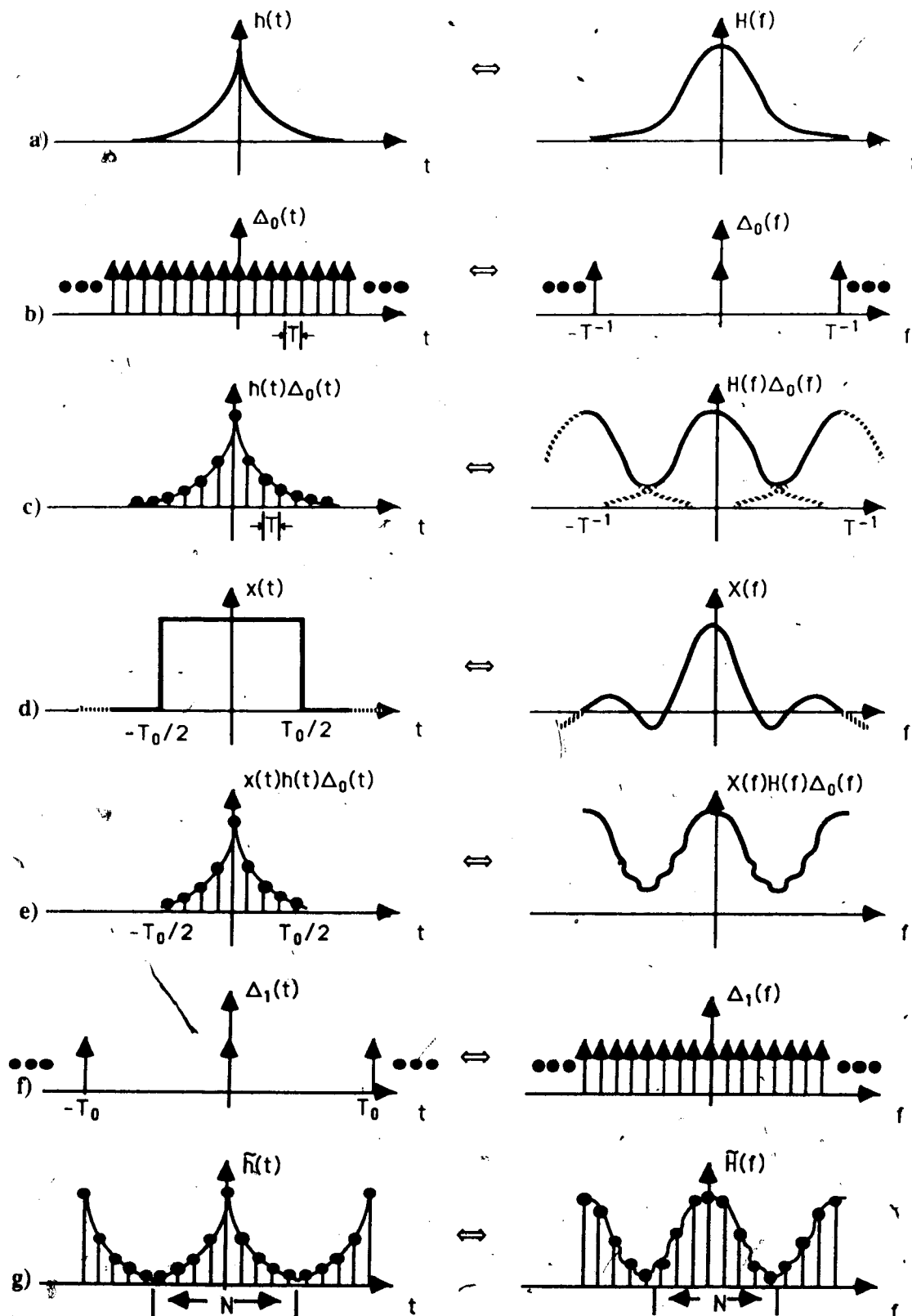
Figure 4.10. Derivation of the Discrete Fourier Transform pair.

convolution in real space which replicates the sampled truncated original function (Figure 4.10g). This transform pair is called a Discrete Fourier transform pair and is amenable to digital computations. As illustrated, the original function and its transform are represented by N discrete samples. For the discrete transform pair to be used, the original function must artificially be rendered periodic.

The net result of the sampling procedure sketched in Figure 4.10g is that the 1D discrete Fourier transform and its inverse are related by equation 4.17.

$$H(k) = \sum_{n=0}^{N-1} h(n)\, W_N^{nk} \; ; \qquad 0 \leq k \leq N-1 \qquad (4.17a)$$

$$h(n) = \sum_{k=0}^{N-1} H(k)\, W_N^{-nk} \; ; \qquad 0 \leq n \leq N-1 \qquad (4.17b)$$

where

$h(n)$ is a sampled periodic function in real space
$H(k)$ is the Discrete Fourier transform of $h(n)$
N is the number of samples
W_N is a shorthand notation for $e^{-2\pi j/N}$

The corresponding 2D and 3D transforms are given by

$$H(k_1,k_2) = \sum_{n_1=0}^{N_1-1} \sum_{n_2=0}^{N_2-1} h(n_1,n_2)\, W_{N_1}^{n_1 k_1}\, W_{N_2}^{n_2 k_2} ; \qquad (4.18a)$$

$$0 \leq k_1 \leq N_1-1 \text{ and } 0 \leq k_2 \leq N_2-1$$

$$h(n_1,n_2) = \sum_{k_1=0}^{N_1-1} \sum_{k_2=0}^{N_2-1} H(k_1,k_2)\, W_{N_1}^{-n_1 k_1}\, W_{N_2}^{-n_2 k_2} ; \qquad (4.18b)$$

$$0 \leq n_1 \leq N_1-1 \text{ and } 0 \leq n_2 \leq N_2-1$$

$$H(k_1,k_2,k_3) = \sum_{n_1=0}^{N_1-1} \sum_{n_2=0}^{N_2-1} \sum_{n_3=0}^{N_3-1} h(n_1,n_2,n_3)\, W_{N_1}^{n_1 k_1}\, W_{N_2}^{n_2 k_2}\, W_{N_3}^{n_3 k_3} ; \qquad (4.18c)$$

$$0 \leq k_1 \leq N_1-1, \; 0 \leq k_2 \leq N_2-1, \text{ and } 0 \leq k_3 \leq N_3-1$$

$$h(n_1,n_2,n_3) = \sum_{k_1=0}^{N_1-1} \sum_{k_2=0}^{N_2-1} \sum_{k_3=0}^{N_3-1} H(k_1,k_2,k_3) \; W_{N_1}^{n_1 k_1} \; W_{N_2}^{n_2 k_2} \; W_{N_3}^{n_3 k_3} ; \qquad (4.18d)$$

$$0 \leq n_1 \leq N_1 - 1, \quad 0 \leq n_2 \leq N_2 - 1, \quad \text{and} \quad 0 \leq n_3 \leq N_3 - 1$$

The same periodicity requirements are made on 2D discrete functions as were made on 1D discrete functions. The original base portion of a discrete function is uniquely defined for N samples, from 0 to N-1. Beyond this range the discrete function is artificially replicated. For example, consider a 2D step function shown in Figure 4.11a and artificial replication in Figure 4.11b. The discrete function is defined mathematically as

$$h(n_1, \ldots) = \begin{cases} \quad & n_1 = 0,1 \text{ and } n_2 = 0,1 \quad ; N_1 = 4, \; N_2 = 3 \qquad (4.19) \\ \quad & n_1 = 2,3 \text{ and } n_2 = 2 \end{cases}$$
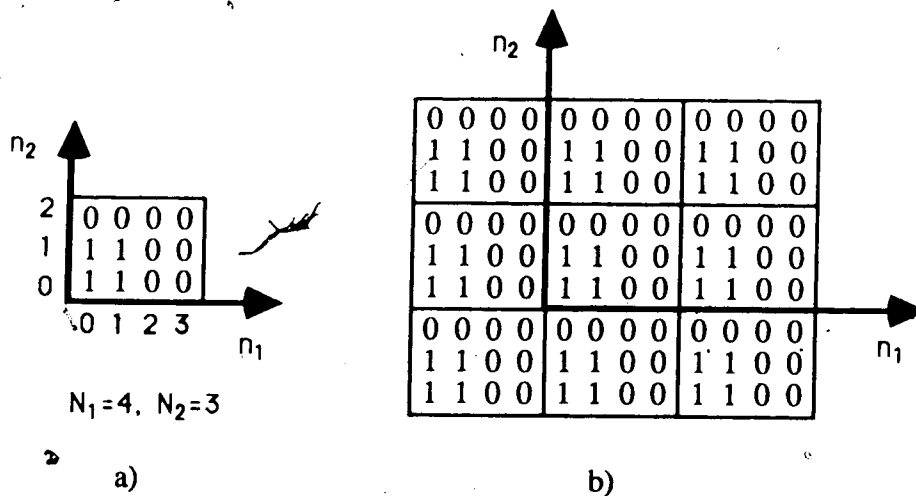
Figure 4.11. The periodicity requirement imposed by the sampling procedure.
a) Fundamental Portion of a 2D function   b) Periodic Nature of a 2D function

Let us now examine the evaluation of the discrete Fourier transform through the Fast Fourier transform algorithm.

4.2.3 Fast Fourier Transforms (1D)

We shall examine the FFT by looking at the development of the 1D algorithm. If the W_N^{nk}'s of equation 4.16 are precomputed and stored, then the direct evaluation of a 1D Fourier transform N elements long would require N^2 multiplications of complex numbers. Since the direct evaluation of the convolution summation (equation 3.11) requires only N^2 multiplications of real numbers, the use of Fourier space to accelerate convolution calculations seems pointless. However, the Fast Fourier Transform (FFT) (Cooley Tukey 1965, Cochran et.al.1967) is an algorithm that can compute the Discrete Fourier Transform (DFT) very efficiently. The FFT achieves its computational efficiency through a "divide and conquer" strategy, which will be briefly explained.

Let us assume a 1D array, h(n), containing N elements (where N is a power of 2). Separate h(n) into 2 parts, using even and odd indices: $S_0(k)$, and $S_1(k)$ such that

$$S_0(k) = \sum_{m=0}^{N/2-1} h(2m)\, W_N^{2mk} \; ; \qquad m=0,1,2,....N/2-1 \qquad (4.20a)$$

$$S_1(k) = \sum_{m=0}^{N/2-1} h(2m+1)\, W_N^{2mk} \; ; \qquad m=0,1,2,....N/2-1 \qquad (4.20b)$$

then using equation 4.17a we find

$$H(k) = S_0(k) + S_1(k)\, W_N^{k} \; ; \qquad k=0,1,2,....N/2-1 \qquad (4.21)$$

Let us examine the value of $W_N^{2mk'}$ and $W_N^{k'}$ when $k'=k+N/2$, then

$$W_N^{2mk'} = W_N^{2m(k+N/2)} = W_N^{2mk}\, W_N^{mN} = W_N^{2mk} \; \text{since} \; W_N^{mN}=1.0 \quad (4.22a)$$

thus

$$W_N^{2m(k+N/2)} = W_N^{2mk}$$

and similarly

$$W_N^{k+N/2} = -W_N^{k} \qquad\qquad (4.22b)$$

Using the identities of equation 4.22 and evaluating equation 4.20 at k+N/2 we find repeat

values. i.e.

$$S_0(k+N/2) = S_0(k) \; ; \; \text{and} \quad S_1(k+N/2) = S_1(k) \tag{4.23}$$

Using these identities in equation 4.21 we find H(k+N/2) becomes

$$H(k+N/2) = S_0(k) + (-W_N^k)S_1(k) \tag{4.24}$$

- Thus, for a particular value of k, 2 points of the Discrete Fourier Transform (H(k)

and H(k+N/2)) can be computed from the odd and even components ($S_0(k)$ and $S_1(k)$).

This computational unit is the basic building block of the FFT, and is called a "Radix (2)

butterfly", as shown in Figure 4.12. Equations 4.21 and 4.24 are evaluated by this

"butterfly" structure, which really stems from the symmetry of sinusoidal functions.
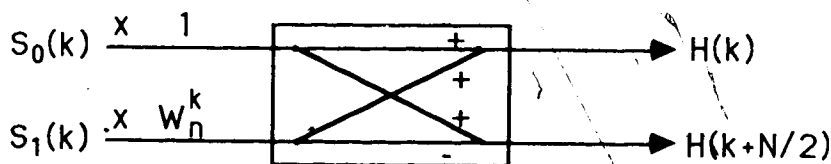
Figure 4.12. The basic building block of the FFT: a Radix (2) Butterfly.

In the definition of $S_0(k)$ and $S_1(k)$, the elements resulting from the first "division"

can now be renumbered from 0 to N/2, and the S's can become two discrete Fourier

transforms each of N/2 points.

$$S_0(k) = \sum_{m=0}^{N/2-1} h(2m) \, W_N^{2mk} \quad = \quad \sum_{n=0}^{N/2-1} h_0^*(n) \, W_{N/2}^{nk} \tag{4.25a}$$

$$S_1(k) = \sum_{m=0}^{N/2-1} h(2m+1) \, W_N^{2mk} \quad = \quad \sum_{n=0}^{N/2-1} h_1^*(n) \, W_{N/2}^{nk} \tag{4.25b}$$

where ,

the h^* sub-arrays contain only the even elements ($h_0^*(n)$) and only
    the odd elements ($h_1^*(n)$)

These new arrays can again be divided into odd and even sub-arrays and the division process continued until eventually only a 2 element DFT need be performed. At this terminal stage, the 2 element DFT is simply

$$H(k) = \sum_{n=0}^{1} h(n) \, W_2^{nk} \qquad (4.26a)$$

where
$$W_2^0 = 1 \text{ and } W_2^1 = e^{-j2\pi/2} = -1$$

then
$$H(0) = h(0) + h(1) \qquad (4.26b)$$
$$H(1) = h(0) - h(1)$$

The FFT procedure is straightforward, the only difficulty being the repetitive re-arranging of h(t) into odd and even sub-arrays. There is, however, a very efficient means of doing this. For example, in order to transform an 8 point sample, we would write the indices in binary with 3 bits ($2^3 = 8$), reverse the bits (from low to high order), and then re-order h(t) according to this new index. Table 4.2 demonstrates this process and Figure 4.13 shows the flow of values toward the resulting 8 point FFT. Note that this algorithm efficiently computes the entire Fourier transform. If only one point of the discrete Fourier transform was desired, it would be more efficient to evaluate the DFT directly.

initial array index	octal	reverse bits	re-ordered array index
0	000	000	0
1	001	100	4
2	010	010	2
3	011	110	6
4	100	001	1
5	101	101	5
6	110	011	3
7	111	111	7

Table 4.2. Partitioning of h(t) into groups containing odd and even indices.

Re-ordered
Array

Resultant
Transform

h(0) $\quad$ x 1 $\qquad$ x 1 $\qquad$ x 1 $\qquad$ H(0)

h(4) $\quad$ x W_2^0 $\qquad$ x 1 $\qquad$ x 1 $\qquad$ H(1)

h(2) $\quad$ x 1 $\qquad$ x W_4^0 $\qquad$ x 1 $\qquad$ H(2)

h(6) $\quad$ x W_2^0 $\qquad$ x W_4^1 $\qquad$ x 1 $\qquad$ H(3)

h(1) $\quad$ x 1 $\qquad$ x 1 $\qquad$ x W_8^0 $\qquad$ H(4)

h(5) $\quad$ x W_2^0 $\qquad$ x 1 $\qquad$ x W_8^1 $\qquad$ H(5)

h(3) $\quad$ x 1 $\qquad$ x W_4^0 $\qquad$ x W_8^2 $\qquad$ H(6)

h(7) $\quad$ x W_2^0 $\qquad$ x W_4^1 $\qquad$ x W_8^3 $\qquad$ H(7)
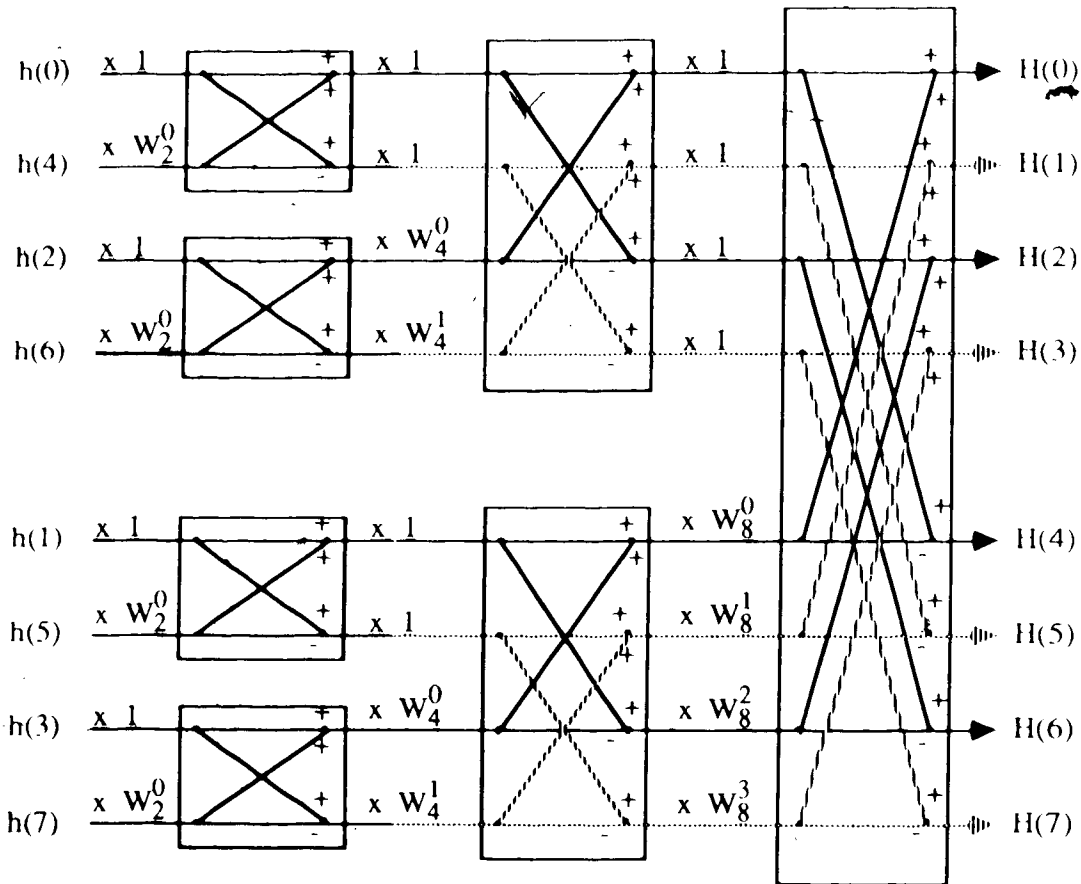
Figure 4.13. Illustration of an 8 point 1D FFT.

With N elements in h(k), N/2 butterflies are required at each stage of the decimation. There are $\log_2(N)$ stages of decimation, therefore the total number of butterflies evaluated is $N/2 \ \log_2(N)$. Since each radix (2) butterfly requires 1 complex multiplication and 2 complex additions, the total number of complex multiplications and additions is $N/2 \ \log_2(N)$ and $N \ \log_2(N)$, respectivley. This can be quite a computational savings compared to N^2 multiplications and additions required for the direct evaluation of the DFT.

4.2.4   Fast Fourier Transforms (2D)

The 1D FFT has been developed, but we are more interested in 2D and 3D convolutions and hence 2D and 3D FFTs. How does the 1D FFT help in this regard? A 2D Fourier transform (equation 4.18) can be evaluated in a number of ways. The direct evaluation requires $N_1{}^2N_2{}^2$ complex multiplications. Equation 4.18a can alternately be rewritten as

$$H(k_1,k_2) = \sum_{n_1=0}^{N_1-1} \left[\sum_{n_2=0}^{N_2-1} h(n_1,n_2)\, W_{N_2}^{n_2 k_2} \right] W_{N_1}^{n_1 k_1}; \tag{4.27a}$$

which can be written as a pair of 1D FFTs

$$G(n_1,k_2) = \sum_{n_2=0}^{N_2-1} h(n_1,n_2)\, W_{N_2}^{n_2 k_2} \tag{4.27b}$$

$$H(k_1,k_2) = \sum_{n_1=0}^{N_1-1} G(n_1,k_2)\, W_{N_1}^{n_1 k_1} \tag{4.27c}$$

Thus, a 2D FFT can be decomposed into a 1D FFT of the columns followed by a 1D FFT of the rows. If the 1D DFT is evaluated directly, the $N_1 N_2$ values of $G(n_1,k_2)$ each require N_2 complex multiplications for a total of $N_1 N_2{}^2$ multiplications. The $N_1 N_2$ values of $H(k_1,k_2)$ each require N_1 multiplications for a total of $N_1{}^2 N_2$ multiplications for $H(k_1,k_2)$, and a grand total of $N_1 N_2(N_1+N_2)$ multiplications for the complete 2D DFT. If a 1D FFT is used, this is reduced to N_1 $(N_2/2\log_2(N_2))$ multiplications for $G(n_1,k_2)$, N_2 $(N_1/2\log_2(N_1)$) for $H(k_1,k_2)$, for a grand total of $1/2$ $N_1 N_2 \log_2(N_1 N_2) = N^2\log_2(N)$ (if $N_1=N_2=N$). It can be shown (Dudgeon 1984, pg76) that a 2D FFT using a (2X2) vector radix butterfly reduces the number of multiplications to $3/4$ $N^2\log_2(N)$. Thus a further 25% can be saved by the use of a direct 2D FFT compared with the row/column decomposition method using 1D FFTs.

Figure 4.14 supplies two simple examples of 2D Fourier transforms which can be evaluated using equation 4.26 and 4.27.

$$\Phi(n_1, n_2) = \begin{bmatrix} 1 & 0 \\ 2 & 1 \end{bmatrix} \quad ; \quad F\{\Phi\} = \begin{bmatrix} 2 & 0 \\ 4 & 2 \end{bmatrix} \qquad G(m_1, m_2) = \begin{bmatrix} 1 & 0 \\ 1 & 1 \end{bmatrix} \quad ; \quad F\{G\} = \begin{bmatrix} 1 & -1 \\ 3 & 1 \end{bmatrix}$$

Figure 4.14. Numerical examples of 2D fast Fourier transforms.

To illustrate images in Fourier space, FFTs were taken of various images using the row/column decomposition technique[8]. The original image and the magnitude of the Fourier spectrum ($\|H(k_1, k_2)\|$) is shown for a number of images in Figure 4.15, 4.16, 4.17, and 4.18.

The original image in Figure 4.15a is a set of horizontal bars; i.e. the original image, $h(n_1, n_2)$, is constant in the horizontal direction (n_1). It is intended to idealize the photon fluence for an infinitely wide beam (incident from above) on a uniform medium. We know the Fourier transform of a constant (K) to be the delta function ($K\delta(k)$) (section §4.2.1.2), and that is indeed what is observed in the horizontal direction of the transform, $H(k_1, k_2)$. In the vertical direction (n_2), $h(n_1, n_2)$ is a series of step functions. The width of each step is constant, but the height of each step varies. We can break $h(n_1, n_2)$ vertically into a number of sub-images, each one containing a single step function. The height and position of each step varies from one sub-image to the next. The transformed image is then the superposition of the transform of each of these separate images (the linearity property, §4.2.1.4). In Figure 4.15c, $\log[\|H(k_1, k_2)\|]$ is displayed in order to show more details of the transform. Without the logarithm being used, the figure would have contained a single bright pixel. The inverse transform is shown to verify that the loop of performing a transform followed by an inverse transform does indeed yield the original image.

---

[8]FFT algorithm implemented was taken from IEEE transactions on Pattern Analysis & Machine Intelligence (PAMI-3, no6, nov 81, pg 698)

Figure 4.16 contains a fluence distribution for a 10x10 cm² beam of 5.0 MeV photons with an infinite SSD. Its transform is similar to Figure 4.15 except that we observe some "ringing" in the horizontal direction of the Fourier spectrum (Figure 4.16b), due to the finite width.

Figure 4.17 is an image representing the total kernel for 1.25 MeV photons. In real space it is similar to a delta function in the horizontal direction yielding the "broad band" of frequencies in the Fourier domain. The kernel values change less abruptly (a more diffuse delta function) in the vertical direction yielding a narrower band in Fourier space. Similarly, Figure 4.18 illustrates the Fourier transform of the 5.0 MeV kernel.
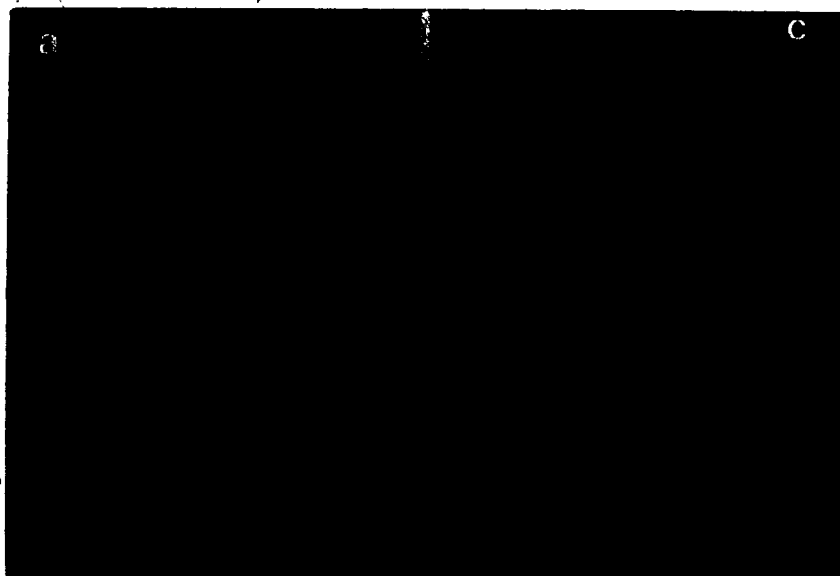
Figure 4.15. The FFT of an idealized fluence of infinite width.
a) original function (L/W = 0/1500)
b) logarithm of the magnitude of the transform spectrum (L/W = 1000/200)
c) inverse transform (L/W = 0/1500)
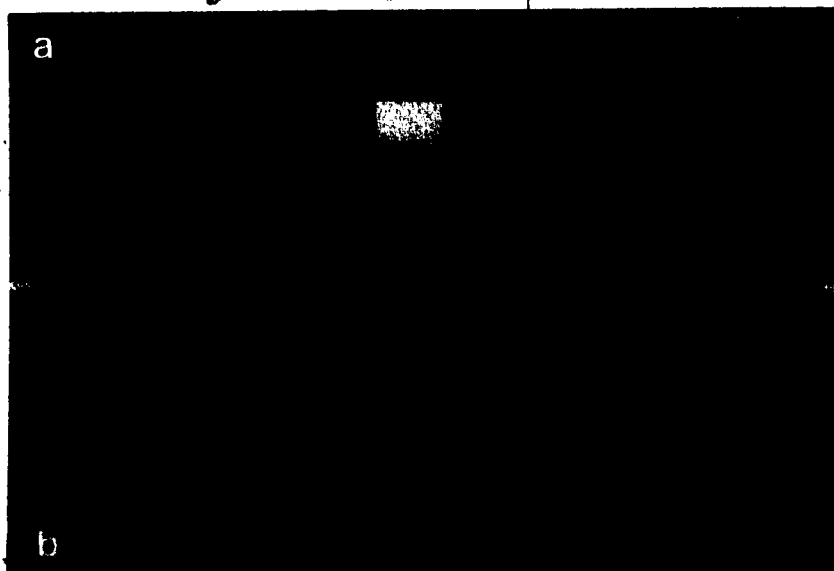
Figure 4.16. The FFT of the fluence computed for a 10x10 cm² beam of 5.0 MeV photons, with an infinite SSD.
a) original function (L/W = 0/3000)
b) magnitude of the transform spectrum (L/W = -800/600)
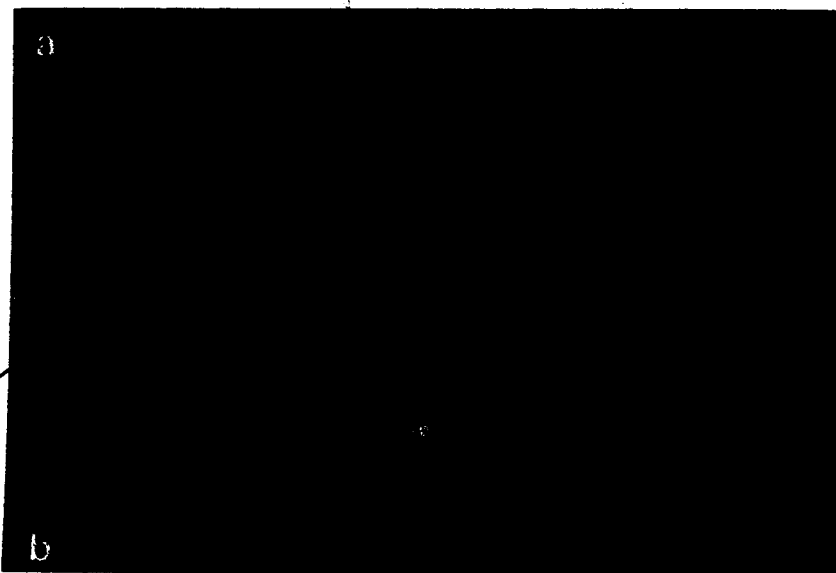
Figure 4.17. The FFT of the total kernel for a 1.25 MeV photon beam.
a) original function (L/W = -1000/50
b) magnitude of the transform spectrum (L/W = 0/1000)
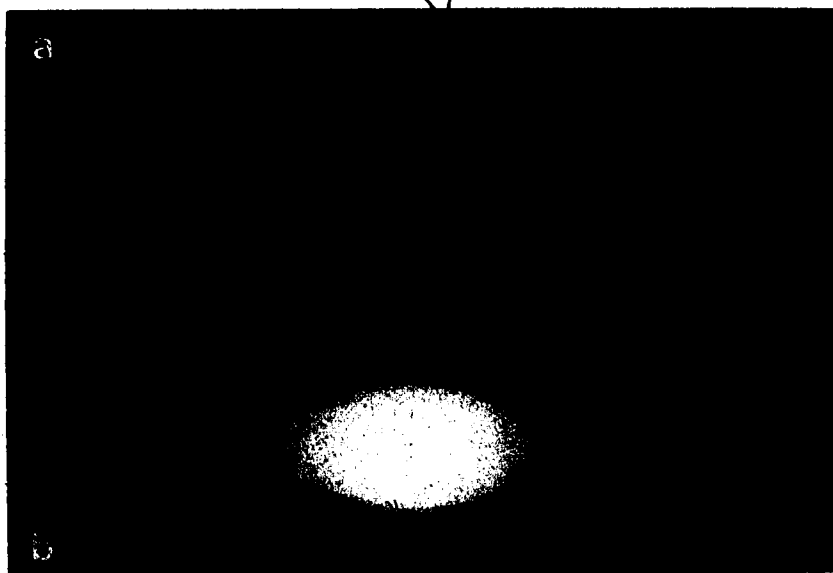
Figure 4.18. The FFT of the total kernel for a 5.0 MeV photon beam.
a) original function (L/W = -1000/50)
b) magnitude of the transform spectrum (L/W = 0/1000)

4.2.4.1   FFT Timings (2D)

· Table 4.3 shows the calculation times required to compute 2D FFT's of various square arrays on a VAX 11/780 computer. The number of butterflies evaluated for each array size $(N^2 \log_2(N))$ is used to determine the average calculation time per butterfly as a function of array size (Table 4.3). We expect the calculation time per butterfly to remain constant. However, this is not the case! The calculation time per butterfly is relatively constant for the three smaller array sizes, but is a factor of four times larger for the largest array size. This is a result of the increased number of "page faults" occurred by the large array size (see section 4.1). A more constant value of the calculation time per butterfly is to be expected if the pages of data are 'locked' in computer memory, avoiding the time penalties of recovering data on disk. Ignoring the effect of "page faults", we find the average time to compute a single butterfly to be 63 μ seconds.

Number of points (N)	Calculation time (CPU seconds)	Calculation time per butterfly (μsec)
32x32	0.32	62.5
64x64	1.5	61.0
128x128	7.5	65.4
256x256	140.0	267.0

Table 4.3. 2D FFT calculation times.

4.3 Convolutions with FFTs

The major advantage of the Fourier transform is that a real space convolution simplifies to an element-by-element multiplication of the two arrays of complex numbers in Fourier space. Thus, the Fourier transformation of a dose distribution (equation 4.29a) yields equation 4.29b. The inverse transformation of equation 4.29b produces a dose distribution in real space (equation 4.29c):

$$D(r) = \int dr' \, \Phi(r') \, G(r-r') = \Phi \otimes G \qquad (4.29a)$$

$$\mathcal{F}\{D\} = \mathcal{F}\{ \Phi \otimes G \} = \mathcal{F}\{\Phi\} \times \mathcal{F}\{G\} \qquad (4.29b)$$

$$D(r) = \mathcal{F}^{-1} [\, \mathcal{F}\{\Phi\} \times \mathcal{F}\{G\} \,] \qquad (4.29c)$$

The steps to solve equation 4.29c are shown as shaded regions in Figure 4.19. In
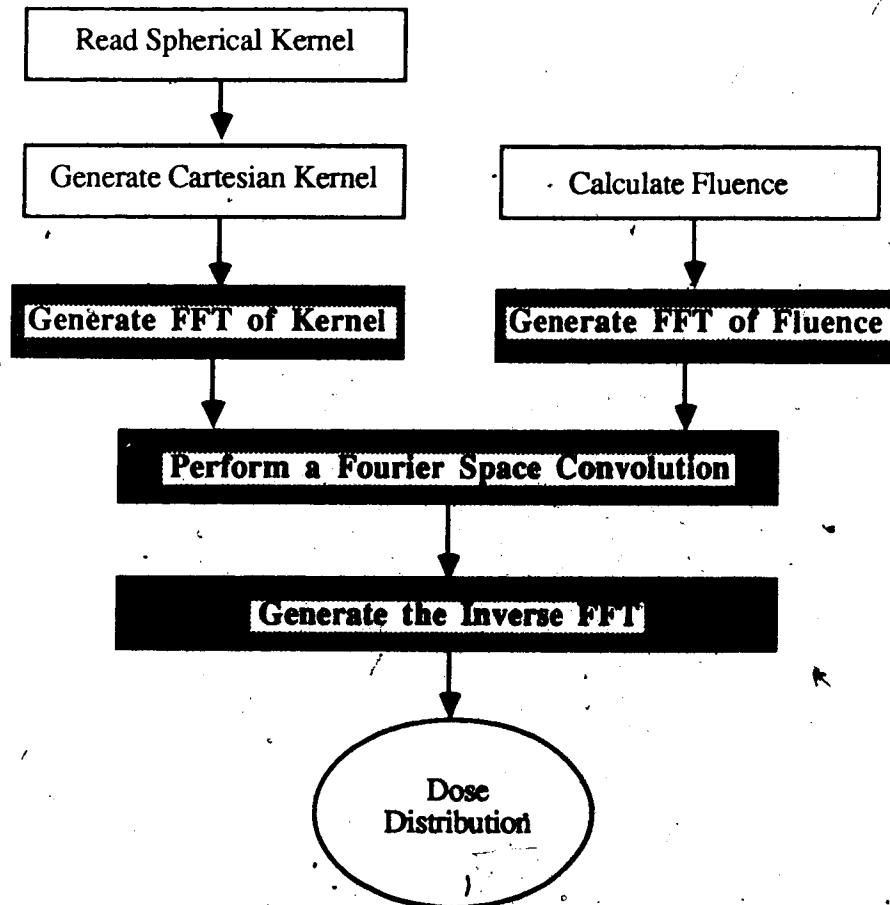
Figure 4.19. Steps involved in Fourier space convolutions.

order to obtain a dose distribution in real space, the convolution method requires that we perform two Fourier transforms, N complex multiplications and finally an inverse Fourier transform. It will be shown that even though more steps are required in the Fourier space convolution than in the real space convolution (recall Figure 4.1), the steps may be performed more quickly.

Section §4.2.2 demonstrated that the discrete Fourier transform had a periodicity restriction imposed upon it. This periodicity requirement causes a slight problem as illustrated in the example of Figure 4.20. As we saw in Figure 4.14, the Fourier transform of a 2x2 image is also a 2x2 image. Thus, when the element by element multiplication is performed in Fourier space, the result is also a 2x2 image. The inverse transform yields a 2x2 image also. However, in real space the result of this convolution would have been a 3x3 image. Comparison with Figure 4.3, shows that the result from Figure 4.20 is an aliased version of the convolution (e.g. the last column and row have been "wrapped-around" and added to the first column and row).

$$\Phi(n_1,n_2)=\begin{bmatrix}1 & 0\\2 & 1\end{bmatrix} \; ; \quad F\{\Phi\}=\begin{bmatrix}2 & 0\\4 & 2\end{bmatrix} \qquad G(m_1,m_2)=\begin{bmatrix}1 & 0\\1 & 1\end{bmatrix} \; ; \quad F\{G\}=\begin{bmatrix}1 & -1\\3 & 1\end{bmatrix}$$

$$F\{\Phi\} \; F\{G\}=\begin{bmatrix}2 & 0\\12 & 2\end{bmatrix} \qquad\qquad F^{-1}\;[\;F\{\Phi\}\;F\{G\}\;]\;=\begin{bmatrix}3 & 2\\4 & 3\end{bmatrix}$$

Figure 4.20. Numerical example of a 2D convolution performed without padding the original functions.

"Padding" the fluence and kernel matrices with zeroes, and then performing the Fourier space convolution yields a 4x4 matrix, but eliminates this "wrap-around" problem as illustrated in Figure 4.21.

$$\Phi(n_1,n_2) = \begin{vmatrix} 0 & 0 & 0 & 0 \\ 0 & 0 & 0 & 0 \\ 1 & 0 & 0 & 0 \\ 2 & 1 & 0 & 0 \end{vmatrix}$$

$$F\{\Phi\} = \begin{vmatrix} 3+j & 2 & 1+j & 2+2j \\ 2 & 1-j & 0 & 1+j \\ 3-j & 2-2j & 1-j & 2 \\ 4 & 3-j & 2 & 3+j \end{vmatrix}$$

$$G(m_1,m_2) = \begin{vmatrix} 0 & 0 & 0 & 0 \\ 0 & 0 & 0 & 0 \\ 1 & 0 & 0 & 0 \\ 1 & 1 & 0 & 0 \end{vmatrix}$$

$$F\{G\} = \begin{vmatrix} 2+j & 1 & j & 1+2j \\ 1 & -j & -1 & j \\ 2-j & 1-2j & -j & 1 \\ 3 & 2-j & 1 & 2+j \end{vmatrix}$$

$$F\{\Phi\}\ F\{G\} = \begin{vmatrix} 5+5j & 2 & -1+j & -2+6j \\ 2 & -1-j & 0 & -1+j \\ 5-5j & -2-6j & -1-j & 2 \\ 12 & 5-5j & 2 & 5+5j \end{vmatrix}$$

$$F^{-1}\ [\ F\{\Phi\}\ F\{G\}\ ] = \begin{vmatrix} 0 & 0 & 0 & 0 \\ 1 & 0 & 0 & 0 \\ 3 & 2 & 0 & 0 \\ 2 & 3 & 1 & 0 \end{vmatrix}$$

Figure 4.21. Numerical example of a 2D convolution performed with padding. Comparison with Figure 4.3 shows the results from the real and Fourier space convolutions are the same.

4.3.1 A Two Dimensional Example

A dose calculation for the same situation as outlined in section §4.1.2 will now be performed in the Fourier domain.. All assumptions required by the convolution technique and permitting the compression of the kernel are met. In addition, the kernel and fluence matrix have been "padded" with zeros to eliminate the "wrap around" problem. ..

Figure 4.22 shows a convolution calculation performed for an incident beam of 5.0 MeV photons. Figure 4.23 shows that the "Fourier" dose distribution is identical to that obtained by a real space calculation, as expected. This confirms the proper functioning of computer programs developed during this work. It is interesting to note that grey scale images (Figure 4.22d) representing dose distributions are not as visually pleasing as the 'colour dose maps' (Figure 4.23) used clinically (Battista et.al. 1984).
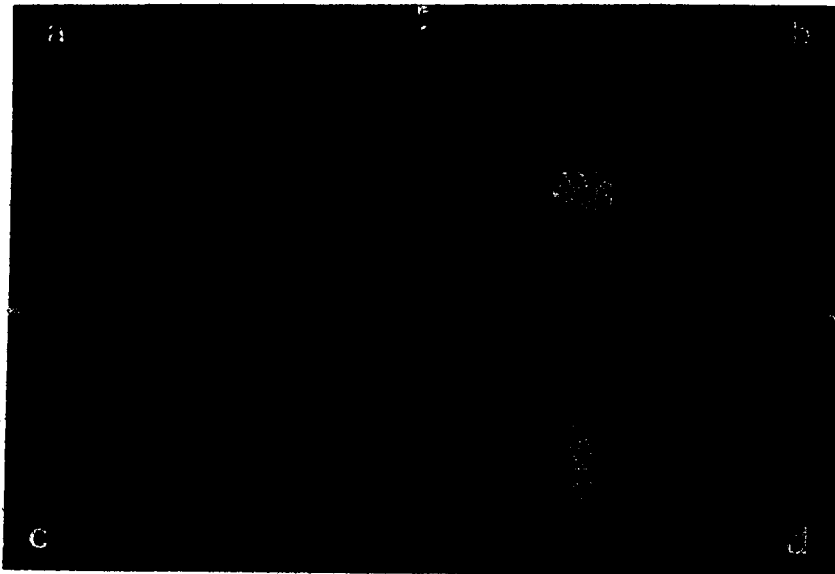
Figure 4.22. A 2D dose distribution calculated in Fourier space for 5.0 MeV photons.
a) Fourier transform of the fluence for a beam of 5.0 MeV photons (L/W = -200/2000)
b) Fourier transform of the total kernel for 5.0 MeV photons (L/W = 1000/2000)
c) The element by element product of a) and b) (L/W = -200/2000)
d) The inverse transform of c) (L/W = 500/2000)
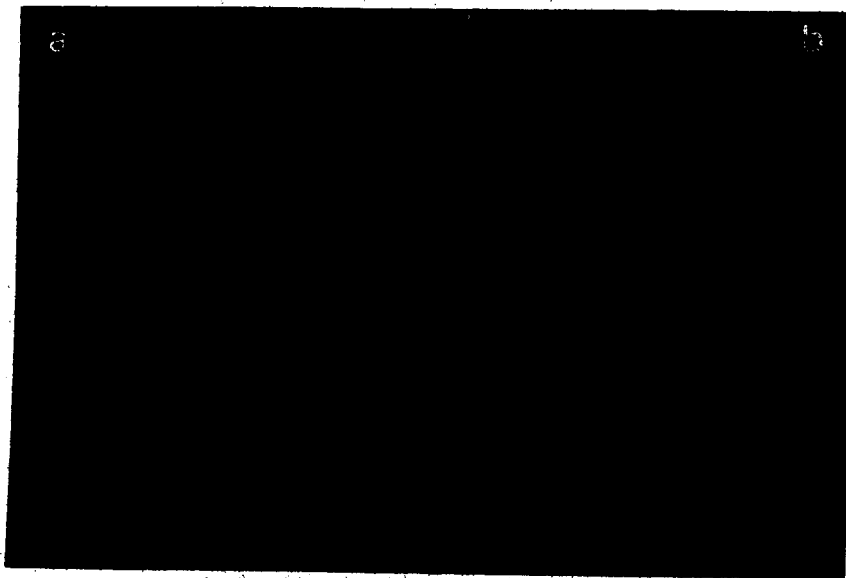
Figure 4.23. Comparison of real space (a) and Fourier space (b) convolutions.

4.3.2 Calculation Time Comparisons Between Real and Fourier Space Convolutions

We have seen that the differences of the dose values calculated by Fourier convolutions and real convolution are negligible. The major advantage of the Fourier route is therefore one of speed[8]. The relative calculation times of convolutions performed in real space to convolutions performed in Fourier space may be determined as follows.

From section §4.1 we determined that the computation time required to perform a convolution in real space is given by

$$\tau_{real} = C_{real} \; N_1N_2 \; M_1M_2 \; CCF \qquad (4.30)$$

where

C_{real} represents the CPU time required to contribute energy from one kernel voxel to one dose point. Section 4.1.2 C_{real} = 36.6 µseconds.

· N_1N_2 represent the size of the fluence matrix

M_1M_2 represent the size of the kernel matrix

CCF is the constrained convolution factor which accounts for a reduction in the number of multiplications by ignoring energy deposition beyond the fluence matrix (see Appendix A).

Assuming square matrices for the kernel and fluence, equation 4.30 becomes

$$\tau_{real} = C_{real} \; N^2 \; M^2 \; CCF \qquad (4.31)$$

From section §4.2.3.1, we determined that the computation time required to perform a single 2D fast Fourier transform[9] was given by

---

[8] Other benefits which have not been discussed include: interpolation by factors of 2, and the ability to apply filters in Fourier space.

[9] This work used the row / column decomposition technique (§4.2.3) to evaluate the 2D FFT. A further gain of 25% could be achieved if a true 2D FFT is used.

$$\tau_{FFT} = C_{FFT}\ N^2\ log_2(N) \qquad\qquad (4.32)$$

where

C_{FFT} represents the CPU time required to calculate one radix (2) a
    butterfly. Section 4.2.3.1 found c_{FFT} = 63.5 μseconds.
N is the linear dimension of the matrix. $N^2\ log_2(N)$ is the number of
    butterflies which need to be evaluated in determining a 2D FFT.

Assuming a 2D kernel of size MxM and and 2D fluence of size NxN, then both the

kernel and fluence arrays must be "padded" with zero values such that they are both of size

$P \geq N+M-1$ and $P=2^Q$, where Q is an integer. If N>M, and $N=2^R$, where R is integer

valued, then P = 2N. i.e. it is neccessary to Fourier transform matrices that are twice as

large as the fluence matrix (if the fluence matrix size is a power of 2). As mentioned

earlier, two forward transformations and one inverse transformation are required (Figure

4.16). We shall ignore the additional complex multiplication per point to actually perform

the convolution in Fourier space. Thus, the total calculation time to perform a Fourier

space convolution may be written as

$$\tau_{Fourier} = 3\ C_{FFT}\ (2N)^2\ log_2(2N) \qquad\qquad (4.33)$$
$$= 12\ C_{FFT}\ N^2\ [\ log_2(N) + 1\ ]$$

What are the expected speed gains for a 2D convolution performed in Fourier

space? Assuming the kernel and fluence matrix sizes are identical, taking the ratio of

equation 4.31 and 4.33 we find

$$\left[\frac{\tau_{real}}{\tau_{Fourier}}\right]_{2D} = \frac{C_{real}\ CCF\ M^2}{12 C_{Fourier}\ [log_2(N)+1]} = \frac{0.048\ CCF\ M^2}{log_2(N)+1} \qquad (4.34a)$$

where the measured values of C_{real} and $C_{Fourier}$ have been substituted. Similarily, the ratio

of calculation times for 1D and 3D are given by

$$\left[\frac{\tau_{real}}{\tau_{Fourier}}\right]_{1D} = \frac{C_{real}\ CCF\ M}{3 C_{Fourier}\ [log_2(N)+1]} = \frac{0.192\ CCF\ M}{log_2(N)+1} \qquad (4.34b)$$

$$\left[\frac{\tau_{real}}{Fourier}\right]_{3D} = \frac{C_{real} \; CCF \; M^3}{36 C_{Fourier} \; [log_2(N) +1]} = \frac{0.004 \; CCF \; M^3}{log_2(N)+1} \qquad (4.34c)$$

Table 4.4 shows the anticipated speed gains when "unconstrained" 1D, 2D, and 3D convolutions are performed (i.e. CCF=1.0) with the same size kernel and fluence matrices (M=N). The calculation speed gains (or losses) to be realized in Fourier space are heavily dependent upon the size of the arrays being transformed and convolved. For a typical dose distribution (N=64), the Fourier route is 1.76 times faster for a 1D convolution, 28 times faster for a 2D convolution, and 150 times faster for a 3D convolution. These ratios should be compared with the more optimistic estimates of Boyer (1984), who ignored some practical considerations (§4.1). Clearly the advantage of Fourier techniques is yet to be explored in 3D dose calculations.

N	1D ratio	2D ratio	3D ratio
4	0.26	0.26	0.09
32	1.02	8.19	21.85
64	1.76	28.09	149.80
128	3.07	98.30	1048.58
256	5.46	349.53	7456.54
1024	17.87	4575.60	390451.57

Table 4.4. Relative calculation speed gains for an "unconstrained" real space calculation with kernel and fluence matrices of the same size, versus a Fourier space convolution.

Figure 4.24 shows the measured calculation times for three algorithms calculating a 2D (64 x 64) dose matrix. The Fourier space calculation is 14 times faster than the real space calculations with a large kernel, but only 1.4 times faster than the real space calculations with a small kernel. The 2D Fourier space calculations are only 3.6 times faster than our current implementation of the "CBEAM" program based on the scatter integration methods of Cunningham (Johns and Cunningham 1983).

How do these speed gains compare with our expectations? For a constrained 2D convolution with kernel and fluence matrices of 64x64 elements, the reduction in the

number of real space operations is 52% (Appendix A). Thus, the ratio of real space

calculation time to the Fourier space calculation time becomes 14.61 (i.e. 28.09 x 0.52),

which is in good agreement with the measured result of 14.
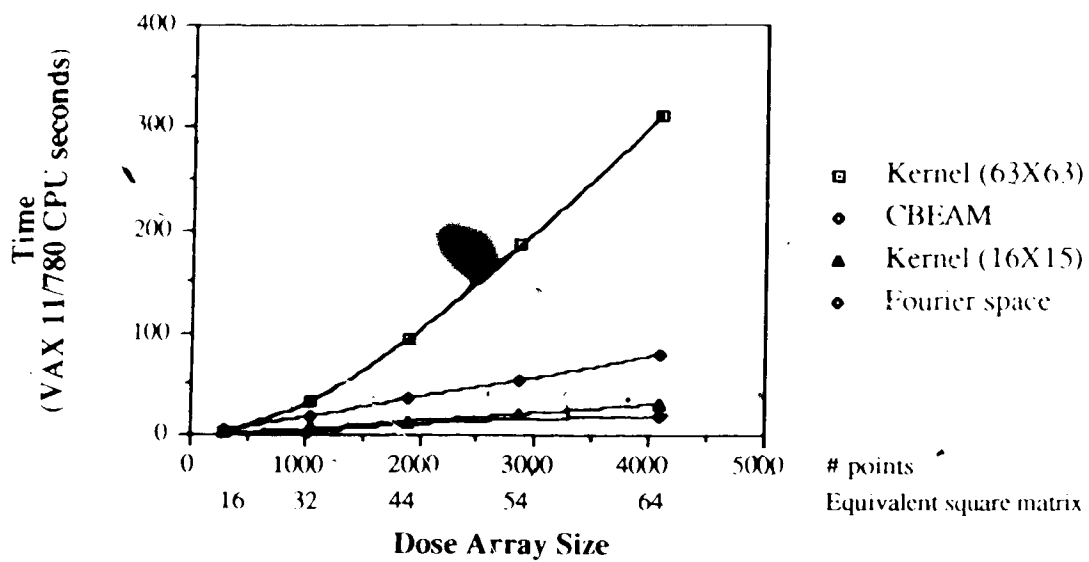
Figure 4.24. Calculation time comparisons.

4.4 Practical Limitations of the Convolution Method

This section deals with the considerations which limit the routine application of the convolution method. The limitations arise because of:

- the fundamental assumptions which led to the convolution integral as outlined in section §3.2.

- the implementation of specific procedures or algorithms

- the practical limitations of current hardware and software.

Thus, the impact of the following-realities will be discussed:-

- energy spectrum of the incident beam

- finite Source to Surface Distance (SSD)

- incident photon source specification

- angular spectrum of the incident beam

- finite heterogeneous phantom

- electron contamination of a photon beam

- restrictions of this convolution implementation

- hardware and software restrictions

4.4.1 Energy Spectrum of the Incident Beam

In the development of the convolution integral, a mono-energetic incident beam was assumed in order to eliminate the integration (or summation) over all incident particle energies. With the inclusion of the energy spectrum, equation 3.5a could have been written

$$D(r) = \sum_{i=1}^{N} \int dr' \ \Phi_{\sigma^0,E_i}(r') \ G_{\sigma^0,\sigma^0>0} \ (E_i, r-r')$$ (4.35)

where

N is the number of components in the energy spectrum
E_i is the energy of the ith spectral component

The incident photon energy is used in equation 4.35 to select both the convolution kernel, and the attenuation coefficient used in the primary fluence calculation. If the incident beam is mono-energetic, then the appropriate mono-energetic kernel and attenuation coefficient are easily selected. If the incident beam is poly-energetic, equation 4.35 shows that N convolutions can be performed to yield the dose distributions for a poly-energetic incident beam. However, this significantly increases the computational burden, depending on the complexity of the energy spectrum. Let us examine a way of avoiding these N convolutions.

If the incident beam is poly-energetic, then it may be possible to model the poly-energetic beam by an "equivalent" mono-energetic beam through the selection of an "effective energy" and an "effective attenuation coefficient" (Mackie 1984, pg 339-343). If this selection accurately models the poly-energetic beam according to the criteria of interest, then we have avoided the calculation of N convolutions. If a single "effective energy or attenuation coefficient" proves to be inadequate, then the energy spectrum incident on the patient surface is indeed required and evaluation of equation 4.35 is unavoidable. An advantage of directly evaluating equation 4.35 is that beam hardening, which is the preferential removal of low energy photons from the beam as it is attenuated, is accurately modelled (Ahnesjö 1987).

Unfortunately, the incident energy spectrum is difficult to determine, and may vary as a function of distance from the central axis of the incident beam (Mohan et.al. 1985). One possible method of determing the incident energy spectrum on the surface of the medium shall now be briefly discussed. The method is based on correlating measured and computed depth dose data. The incident angular spectrum is assumed to be negligible.

Assume that convolution calculations have been performed for an incident narrow "pencil" beam for each energy bin making up the spectrum. The dose distribution of such a measured "pencil" beam can also be derived from measurements (Boyer, 1987). The

measured pencil beam distribution may be related to the calculated mono-energetic *pencil beams* as follows.

$$D(r) = \sum_{i=1}^{N} a_i D_i(r) \qquad (4.36)$$

where

$\quad$ D(r) is the total dose at a depth r along the ray through point on the surface where the energy spectrum is to be determined
$\quad$ N is the total number of energy components
$\quad$ a_i is the weight of the ith energy component
$\quad$ $D_i(r)$ is the dose at depth r from the ith energy component

The weights of the spectral components may be determined by performing a multiple linear regression analysis with the monoenergetic convolution pencil beam doses as the independent variables and the measured pencil beam dose as the dependent variable, as shown in equation 4.37 (Statworks 1985, pg 59)

$$Y_j = \sum_{i=1}^{N} a_i X_{ij} + b + \text{error} \qquad (4.37)$$

where

$\quad$ Y_j is the measured dose at depth 'j'
$\quad$ a_i is the weight of the ith energy component
$\quad$ X_{ij} is the mono-energetic pencil beam dose at depth 'j' delivered by the ith energy component
$\quad$ b is a constant
$\quad$ error is the residual error in the linear relationship

The constant term in equation 4.37 has no physical meaning except to say that there is a uniform background energy deposition independent of depth and incident particle energy. This method of analysis should be used with care, ensuring the coefficients are physically meaningful (i.e. positive), and that the standard errors and confidence levels are acceptable.

$\quad$ We will now investigate the energy spectrum along the central axis of a 15 MV X-ray beam. Dose distributions were calculated for mono-energetic "pencil beams" (i.e. a field size of "0"x"0"cm^2) for incident photon energies of energies 0.5, 1.25, 5.0, and 10.0

MeV for which the kernels were readily available. The Tissue Maximum Ratio (TMR) for a 15 MV X-ray pencil beam is shown in Figure 4.25 along with the four computed mono-energetic pencil beams. The 5.0 MeV mono-energetic kernel reproduces the measured data extremely well at depths below the depth of maximum dose. The poorer agreement at shallower depths is due to electron and low energy photon contamination from the field production sub-system (Mackie 1984). This "effective energy" compares well with the observations of other authors (Mackie 1984).
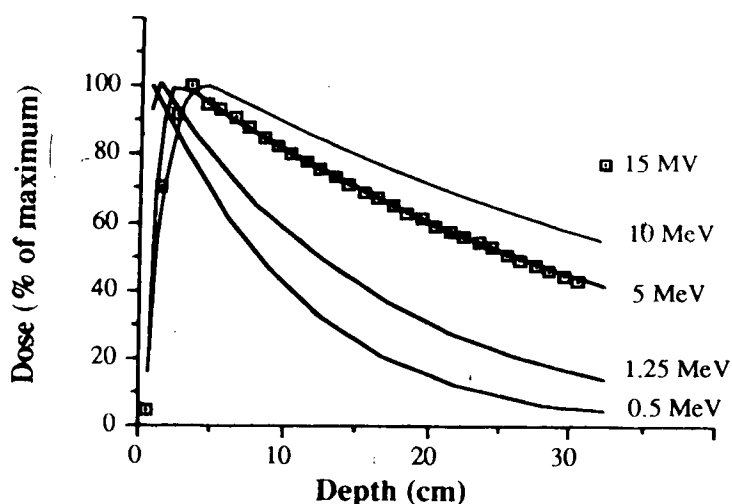
Figure 4.25. Depth dose curves computed for mono-energetic pencil beams of 0.5, 1.25, 5.0, 10 MeV. The 0x0 TMR is also shown for a 15 MV X-ray beam.

A multiple linear regression was also performed with the four mono-energetic pencil beams and the 15 MV X-ray beam. Better fits for the depth dose curve were achieved both in the "build-up" and post "build-up" region, but either negative spectral weights were required or the standard error and confidence level were unacceptable. It appears that additional constraints on the weights are required to determine a physically meaningful spectrum. With such constraints, this approach may indeed be a novel way of determining the energy spectrum for a high energy X-ray beam.

Mohan et.al. (1985) have determined a 32 bin energy spectrum using Monte Carlo techniques. This energy spectrum was then verified by calculating a dose distribution

using the full energy spectrum (Chui et.al. 1984). Excellent agreement was achieved with

a measured dose distribution. Unfortunately, a comparison between dose distributions

calculated using a 32 bin and a 1 bin spectrum were not presented.

Figure 4.26 compares the calculated 2D dose distribution for a mono-energetic 5.0

MeV photon beam with that of a measured 15 MV X-ray beam. The measured dose

distribution was obtained with an automated measurement system developed in this

laboratory (Antolak et.al., in press). Each scan line of the dose distribution is obtained by

driving a p-type diode across the radiation field incident on a water phantom (Therados

RFA-3). Once a scan line is complete, the data is transferred to an IBM PC/XT compatible

computer, the depth of the probe is increased, and the probe is driven back across the

radiation field. Once the scanning process has completed (about one hour) the entire 2D

Figure 4.26. Comparison of dose distributions for a measured 15 MV X-ray beam and
one computed with a mono-energetic 5.0 MeV kernel. The measured and calculated beam
had a field size of 10x10 cm². The measured beam had an SSD of 200 cm, while the
calculated beam had a SSD of infinity.
a) computed 5.0 MeV beam   b) measured 15 MV X-ray beam
c) computed "hotter" than measured   d) computed "colder" than measured

measured dose distribution can be transferred to a treatment planning computer for display and detailed comparison with computed data.

Let us now examine Figure 4.26. As expected, there is a slight discrepancy in the build-up region. The calculated dose is more penetrating than the measured dose. This may be a result of neglecting beam divergence. The measured dose is "hotter" than the calculated dose outside the field edges by 5%. There are some discrepancies near the beam edges, which will now be discussed.

4.4.2 Infinite SSD

In the formulation of the convolution integral, an infinite SSD was assumed in order to force all incoming particles to travel along parallel rays. This allows us to ignore the angular spectrum of the incident particles on the surface of the irradiated system. The infinite SSD assumption also makes the primary fluence calculation trivial. In the absence of field modifying devices, the primary fluence is constant across the field area and zero outside the field.

With the introduction of a finite SSD, these simplifications no longer hold, and the primary fluence needs to be calculated along divergent rays. During the "convolution" step, this in turn requires that the kernels be aligned along these rays prior to the deposition of energy by the kernel. This alignment of the kernels implies that the kernel is no longer spatially invariant and this calculation method is more appropriately called a "superposition" method. Unfortunately, the use of a superposition technique negates the speed gains of Fourier space. So, it is in our best interests (i.e. to reduce calculation time) to try and conserve the spatially invariant kernel.

In the case of a divergent beam, a compromise in which we maintain a spatially invariant kernel, but compute the primary fluence along divergent rays may be acceptable. The error involved in this hybrid approach is dependent upon the beam energy, the field size, the SSD, and the depth within the medium. The literature reports a range of errors for

not tilting the kernel from 7% for a large field of 1.25 MeV photons with a small SSD at medium depth (Ahnesjö 1987, pg 100), to less than 0.5% for a medium field of 4 MV X-ray beam with a medium SSD and medium depth (Mackie et.al. 1987, pg 109). For an incident beam of 5.0 MeV photons, the errors are expected to be larger due to the increased spatial extent of the kernel.

The importance of "tilting" the kernal in terms of the dose deposited to an off-axis point, can be answered using the "catcher's" point of view. The kernel can be centered on the destination voxel in a tilted and untilted manner, and the dose determined to that one point only. Any difference in the dose results is attributable to the kernel tilting. The effect of kernel tilting for higher energy beams has been left for future work. In this work, the kernels were assumed to be spatially invariant.

Figure 4.27 illustrates the fluence calculated for a divergent and non-divergent beam. The non-divergent fluence was used in the calculation of the dose distribution in

Figure 4.27. Beam divergence and the fluence calculation.
Fluence calculated for a non-divergent beam (a) and for a divergent beam (b).

Figure 4.26, and the divergent fluence was used for the calculation of the dose distribution

in Figure 4.28.

Figure 4.28 shows a comparison between the measured 15 Mv X-ray beam and a

dose distribution computed with a divergent fluence calculation. The computed dose

distribution agrees extremely well with the measured one. This measured distribution is the

one which now grows "hotter" with depth as is to be expected due to beam hardening. The

measured distribution still exhibits a 5% dose level well outside the field edges. The slight -

disagreement near the beam edges (3%) may be due to a mismatch in field sizes. As

expected, the most significant area of disagreement is in the "build-up" region. Electron

contamination and the mono-energetic convolution kernel may be responsible for this

disagreement.

Figure 4.28. Comparison of dose distributions for a measured 15 MV X-ray beam and one computed with a mono-energetic 5.0 MeV kernel. Both beams were computed for a field size of 10x10 cm^2, and an SSD of 200 cm. All other convolution assumptions were met.
a) computed 5.0 MeV beam   b) measured 15 MV X-ray beam
c) computed "hotter" than measured   d) computed "colder" than measured

The algorithm currently in clinical use (CBEAM) was also compared to the

measured data in Figure 4.29. We see excellent agreement between the calculated

distribution and the measured distribution everywhere in the field. The measured data still

appears 5% high beyond the field edges, and is much "hotter" at the very surface of the

irradiated system. Such superb agreement is *not* surprising. CBEAM uses measured data

as its data base, and in this situation it is simply reconstructing the measured data

(Cunningham, 1972). A situation requiring both calculation algorithms to be predictive

will be presented next.

Figure 4.29. Comparison of dose distributions for a measured 15 MV X-ray beam and one computed using the CBEAM algorithm. Both beams had a field size of 10x10 cm², and an SSD of 200 cm.
a) measured 15 MV X-ray beam
b) CBEAM computed 5.0 MeV beam
c) measured "hotter" than computed
d) measured "colder" than computed

4.4.3 Incident Photon Source Specification

Another assumption of the convolution algorithm was that all incident particles travel along a 'ray' from a *point* source. This assumption implies that; 1) the source is infinitesimal in size, and 2) photons scattered by the field production and field shaping subsystems are either negligble or to be treated separately as a secondary photon source. This eliminates the angular spread of incident photons at each point on the medium surface, although the angle of incidence will vary from surface point to surface point. In other words, every point on the surface sees particles coming along a single ray from the source.

To overcome the assumption of a single point source, it has been suggested that a normalized Gaussian function be used to model the actual source (Jing and Boyer, 1987). The procedure consists of performing a fluence calculation for a point source, and then performing a 1D convolution of this fluence (a step function) with a gaussian function in the lateral direction. The finite source size is especially important in modelling the beam penumbra (Cunningham CBEAM and IRREG, Mackie 1987 pg 109).

To date, exogenous photon scatter from the field production and field shaping subsystems has not been modelled in convolution methods. Exogenous scatter requires the specification of energy and angular distributions (see section §4.4.4) of the photons incident on the surface of the medium. Retracted "tissue compensators" are an example where inadequate handling of exogenous scatter can account for errors of up to 11% (Robinson and Scrimger 1987). In this work, the exogenous scatter from field modifying devices has been ignored. However, the primary fluence has been attenuated according to the length of the ray-line piercing the field modifying device.

As a practical example, let us compute the dose distribution for a $10 \times 10 \text{ cm}^2$ field when the central axis is occluded by a lead block 8.5 cm thick (i.e. 5 half value layers) which casts a shadow of 1.5 cm.wide at the SSD (Figure 4.30). The bar extended completely across the field in the longitudinal direction. A divergent fluence is calculated

for the effective energy of 5 MeV and subsequently modified to account for the primary

attenuation by the field modifying device. The voxel sizes are $(0.5cm)^3$.

Figure 4.30. Dose calculation for a 5.0 MeV photon beam computed with a divergent fluence and bar occluding the central axis.
a) Fluence calculated on divergent rays   b) 5.0 MeV primary kernel
c) Resulting dose distribution.

The dose at depth of 5 cm has been plotted as a function of distance from central

axis for three dose distributions; one calculated with the convolution method, one calculated

with the program CBEAM, and one which has been measured (Mackie 1984). Figure 4.31

shows these data. We note:

- in the area behind the block, that measured doses are slightly larger (4%) than

  predicted by the convolution method and significantly larger (15%) than

  predicted by CBEAM.

- beyond the block edge, the tables turn, and the measured data is less than

  convolution and much less than CBEAM.

The major reason for the differences between the convolution and CBEAM algorithms is
that the convolution method spreads electron energy under the block, whereas the CBEAM
algorithm assumes on-the-spot energy absorption and hence disallows the spread of energy
to regions under the block.
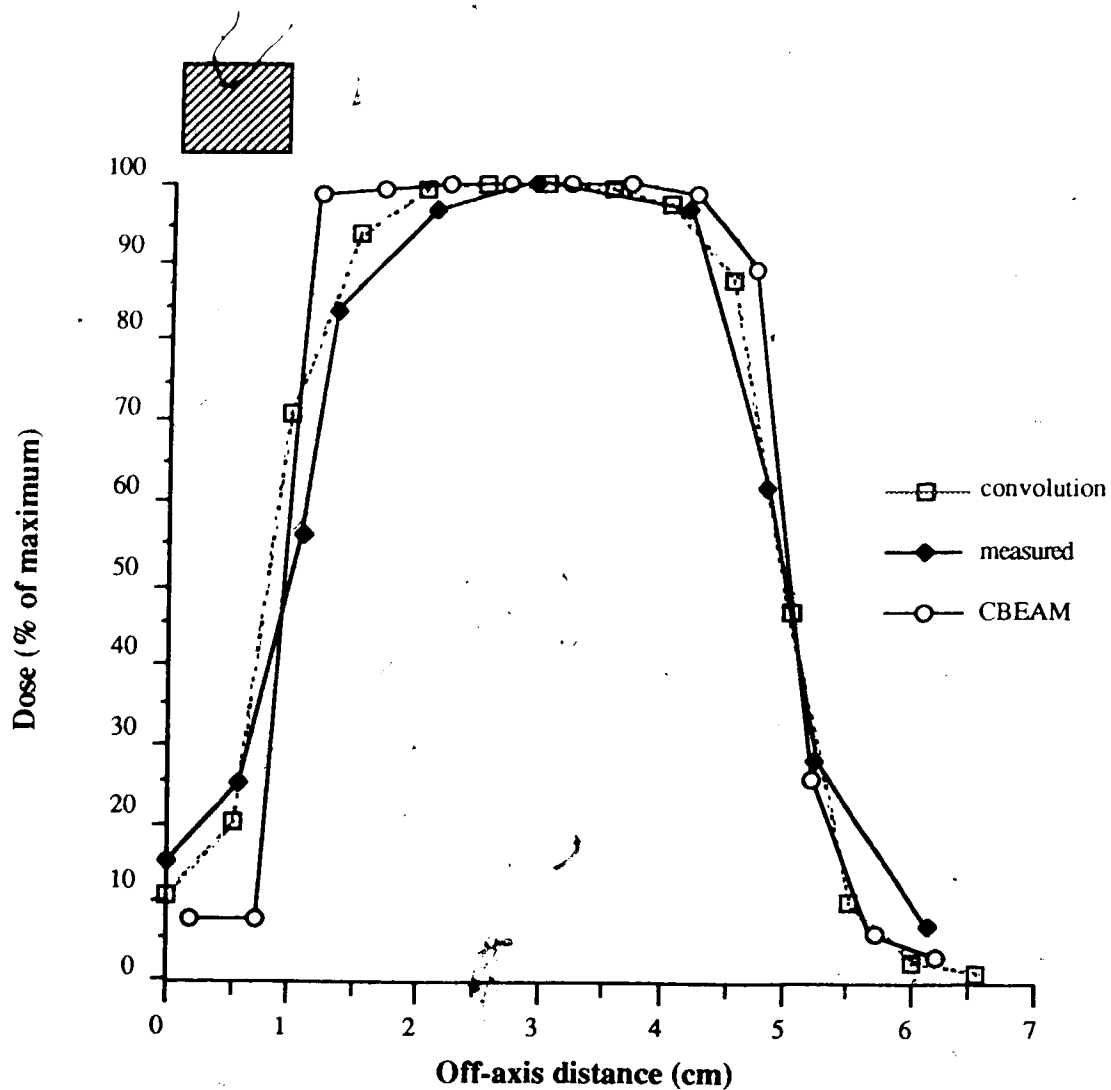
Figure 4.31. Dose profile plot at a depth of 5 cm for a 15 MV X ray beam, blocked by a lead shield.

4.4.4 Angular Spectrum of the Incident Beam

The angular spectrum of incident particles at each point on the surface of the medium has been mentioned as being required for a number of reasons; beam divergence, finite source width, exogenous scatter from field production and field shaping sub-systems. An angular spectrum requires transportation of secondary particles in the direction of the incident particles. This is turn requires (to be rigorous) the alignment of the kernels along the incident direction and thus prohibits the use of the convolution technique.

Reasonable agreement seems to be achieved for the beam divergence problem if the fluence is calculated for a divergent beam and the kernels remain untilted. The finite source width has been prevously discussed. The angular spectrum of incident particles resulting from scattering by the field production sub-system (i.e. field flattening filter and collimators) has been calculated from Monte Carlo techniques and appears significant only in its contribution to the diffuseness of the beam boundaries (i.e. penumbra) (Mohan 1985). The modelling of the field shaping sub-system appears to be the largest unsolved problem (Robinson and Scrimger 1987). It has yet to be shown whether the convolution method can actually solve this problem (e.g. by transporting primary particles from the field shaping sub-system onto the patient sub-system).

4.4.5 Finite Heterogeneous Phantom.

The use of a homogeneous water equivalent medium is required by the convolution formalism in order to:

1) match the medium to that in which the kernels were generated. This eliminates the need to have kernels for each atomic number and density.

2) ignore the inhomogeneity problem in which the kernels must somehow be modified prior to "convolution".

The infinite medium is required in order to avoid modifying the kernel near the medium boundaries (e.g. on beam entrance and exit side of phantom). These contour corrections

may be considered as "inhomogeneity corrections". Thus, a finite or an inhomogeneous
medium requires the modification of the convolution kernel. This again makes the kernel
spatially variant, requiring a "superposition" algorithm instead of a strict convolution.

A finite inhomogeneous (with respect to electron density) medium also impacts on
the primary fluence calculation although this does not pose a severe problem. The primary
fluence calculation would proceed as follows:

- the incident fluence is specified everywhere on the surface of the irradiated
  system. This fluence may include an energy and angular spectrum.

- the particles incident on the irradiated system are transported along their
  incident direction to the surface of the phantom.

- The primary fluence may then be calculated everywhere within the phantom.
  The "water equivalent" distance traversed in the phantom is obtained by "ray-
  tracing" and applied to attenuate the primary fluence within the hetergeneous
  phantom.

The major difficulty with phantom inhomogeneities is the modification of the
kernel. As shown earlier, the total kernel contains the transport of both charged particles
and scattered photons. Thus, any correction must consider the mean path taken by both
particle types! If electrons deposit their energy on-the-spot, then inhomogeneities require
kernel modification to account for the transport of photons only. If electrons do not deposit
their energy on-the-spot, then both the photon and electron paths must be suitably
corrected. The current set of kernels contains the energy deposition from electrons set-in-
motion by the primary photon. However, the transport of secondary photons and the
energy deposition of any electrons they set in motion are coupled together in the first,
second, and multiple scatter kernels.

The transport of photons through inhomogeneities is generally modelled by a
simple density scaling of the photon components of the kernels (Mackie et.al. 1985, Mohan
et.al. 1986, Boyer et.al. 1986, Ahnesjö 1987) and has produced remarkably good results

in 1D. Other techniques have been suggested for scaling the electron component of the kernels (Andreo and Brahme 1983, Kornelson 1986). A discussion of these kernel-modifying techniques is considered beyond the scope of this work. However, it should be noted that the availability of the five kernel categories allows modification of each kernel in a manner specific to the order of the scattered photon.

If atomic number inhomogeneities are to be considered, then a full set of kernels will be required for each type of material. This is probably not too critical for the patient sub-system since most tissues are "water equivalent". However, kernels are certainly required for materials encountered in the field production, field shaping, and field verification sub-systems.

4.4.6 Electron Contamination of a Photon Beam

Although not one of the explicitly stated assumptions of the convolution algorithm, we have assumed that only photons are incident on the irradiated system. In practice, electron contamination from the field production sub-system is present in most photon beams (Mackie 1984). This may be modelled by performing a convolution calculation for an incident beam of electrons, provided suitable electron kernels are available. This dose distribution would then be added to the dose distribution resulting from the incident photon beam. The convolution algorithm has been applied to the electron beam dose calculation problem and has met with limited success (Hogstrom et.al. 1982, Cygler et.al. 1987, Mackie 1987). Further investigation is required in the modelling of electron beams with the convolution method before the problem of electron contamination can be rigourously solved. In particular, the transport of electrons in heterogeneous materials remains as a difficult problem today (Perry, 1988).

4.4.7   Implementation Restrictions

The restrictions discussed in this section are imposed by this specific implementation of the convolution algorithm and are not restrictions of the convolution algorithm in general.

As discussed earlier (§3.3), the convolution kernels represent energy deposited when a primary photon interacts in the center of the interaction voxel. In practice, photons interact throughout the interaction voxel which are of finite size. Thus, it may be neccessary to 'blur' the kernels to account for the interaction of primary particles throughout the interaction voxel (Mackie, personal communication).

In the determination of the primary fluence in a voxel, we have attributed the fluence at the voxel center to the entire voxel. If the voxels are small enough that the fluence is uniform (or changing linearly)[10] across the voxel, then the fluence at the center is a good approximation of the average fluence. However, if the fluence changes cannot be assumed to be linear across a voxel, then a number of fluences should be calculated through out the voxel and the average of these fluences attributed to the voxel. This complication has been addressed for those pixels at the edge of either a field boundary or a field modifying device.

All Cartesian convolution kernels used in this work have contained cubic voxels. This requires that the fluence matrix also be comprised of cubic voxels. When a series of CT slices is used to generate the fluence matrix, the linear dimensions of the voxel in the CT plane are the same. However, the spacing in the third longitudinal direction may be quite different. Thus, it may be advantagous to use voxels which are rectangularly shaped.

The convolution kernels used in this work were the total kernels for a specific energy. When attacking the inhomogeneity problem, it may be beneficial to perform multiple superpositions, one for each kernel category.

---

[10]As noted earlier, $e^{-\mu x} \approx 1 - \mu x$, for small μx.

All convolutions performed in this work have been either 1D or 2D. Ultimately, we may wish to perform a 3D convolution over the entire irradiated 3D volume of the patient. The extension from 2D to 3D is straightforward. The only complications to arise should be an escalation in calculation times and this may be remedied by hardware and software advances.

4.4.8 Hardware and Software Restrictions

The hardware and software restrictions discussed here are related to the time taken to perform a convolution calculation and the resources available in our laboratory.

We have seen that the size of physical memory limits the amount of data that can be quickly accessed, and hence causes "page faults". By increasing the size of the physical memory, fewer page faults would be incurred, resulting in a decreased calculation time. For example, a real space convolution with a resolution of 0.5 cm and a maximum phantom size of 40 cm^3, would require physical memory of:

$$80^3 \text{ voxels/array} \times 4 \text{ bytes/voxel} \times 3 \text{ arrays} = 5.85 \text{ MBytes}$$

to be able to "hold" all data arrays required for the convolution. Additional physical memory is also required by the program, other users of the computer, and the computer operating system. Memory sizes of this magnitude are readily available with present technology at reasonable cost.

Another means of speeding up the convolution algorithm is by using a faster computer or by using additional specialized hardware such as an array processor or custom made arithmetic processors (AMI S28214 - a signal processing chip which performs a complex 32 point 1D FFT in 1.3 milliseconds (compared to an estimated time of 5.7 milliseconds on a VAX 11/780 processor - Table 4.3)).

On the software side, there may be some "tricks" for reducing the size of the kernel and fluence arrays without greatly affecting the accuracy of the calculation, yet decreasing the overall calculation time. These techniques consist of modelling high gradient regions (close to the interaction voxel) with fine resolution kernels, and low gradient regions (at a distance from the interaction voxel) with coarse resolution kernels (Mackie 1984, Boyer 1986). Multiple convolutions are then required, but because of the reduction in kernel size, the overall computation time may be improved without a loss in accuracy.

A decrease in calculation time can also be realized through software by using a more efficient FFT algorithm (e.g. using a full 2D FFT instead of the row / column decomposition method). If FFT's are performed with input functions comprised of real numbers only, it is possible to "pack" two real functions into an input function consisting of complex numbers and perform two FFT's for "the price of one" (Brigham 1974, pg 166).

Other transforms, e.g. the Hartley transform (O'Neill, 1988), may also be useful in reducing calculation times.

Chapter 5

Discussion and Conclusions

"Would you tell me, please, which way I ought to go from here?"

"That depends a good deal on where you want to get to," said the Cat.

<u>Alice's Adventures in Wonderland</u>
Lewis Carroll

5.0 Discussion and Conclusions

This chapter summarizes the importance of the work performed to date, suggests directions in which further investigation is required, and examines the fundamental question - "Is convolution a useful technique in calculating dose distributions for megavoltage photon beams?"

5.1 Discussion

In order to answer the question, it was necessary to document, review, and investigate:

- the energy deposition by the interaction of radiation with matter (chapter 2 and §3.3)

- the specification of the general dose calculation problem (section 3.1)

- a most general solution to the problem (section 3.2.1)

- ,the explicit restrictions placed on the general problem if a convolution is to be applied (section 3.2.4)

- the feasibility of the convolution algorithm in solving the photon dose calculation problem routinely (chapter 4).

5.1.1 Energy Deposition by the Interaction of Radiation with Matter

Chapter 2 presented a concise and consistent overview of the interaction of radiation with matter. In preparing this overview, many ambiguous or inconsistent descriptions were found in various references and text books. These were reconciled in this Chapter.

For example, dose is defined in many publications as dE_{ab}/dm (Johns and Cunningham, 1983). This set of symbols mathematically means that the dose, $D(m)$, is the

differential of the function, E_{ab}, with respect to m. That is, D(m) may take on a different value as m changes. This is *not* the intention of the macroscopic dose concept.

The kernels used in the convolution algorithm represent the energy deposition by charged particles according to the order of the scattered photon which set the particles in motion. It was confirmed that the energy contained in the primary spherical kernels for incident photons of 1.25 and 5.0 MeV agreed closely with tabulated values of the energy absorbed, ε_{ab}, based on fundamental radiation physics. The fraction of incident photon energy contained in each kernel type was noted in Table 3.4.

Conversion from the spherical geometry (optimal for the Monte Carlo generation of the kernels) to a Cartesian geometry (optimal for calculation and display purposes) was discussed (§3.3.2). Cartesian kernels were pictorially examined in two dimensions (2D) and appear correct. An extensive software "tool box" is now available for the display and examination of the kernels. An error identified by this work in the Monte Carlo kernel generation has been remedied on subsequent regeneration of the data by the National Research Council of Canada. These revised kernels have now been distributed worldwide for general application to radiation physics problems.

The selection of the kernel extent and voxel size is critical to both the calculation time and accuracy[12]. For example, a large kernel extent is required if field size effects are being modelled (i.e. the effect of increasing the field size must be "felt" by all dose points); or, a fine resolution kernel is required if the longitudinal dose "build-up" region is being modelled. Energy loss due to kernel extents should be kept as low as is reasonably achievable (ALARA) to avoid dose artifacts. The energy loss may be minimized by increasing the number of kernel voxels (and computation time) or by increasing the size of the kernel voxels (dose resolution decreases).

---

[12]Due to the critical nature of these parameters, it is essential that all published works using the convolution technique clearly state the kernel size and extent.

Another technique, used in this work, to decrease calculation time was to "compress" the kernel. This reduces a full 3D convolution to either a 2D or 1D convolution with commensurate reductions in calculation time.

Future work in the validation of the kernel data includes:

- a comparison of the kernels to theoretical energy-versus-angle distributions for Compton scattered electrons and photons.

- a comparison of the kernels to similar ones used in the Equivalent Tissue Air Ratio (ETAR) (Sontag 1979) and the "delta volume" methods (Wong 1983)

- the generation of first, second, and multiple scatter kernels by convolving photon fluences with primary kernels of appropriate energy.

5.1.2 Statement of the General Dose Calculation Problem

In section 3.1, an arbitrary radiation field was completely specified by the particle source term, differential in particle type, direction, energy, and location on the surface of an "irradiated system". The "irradiated system" is defined by the electron density and atomic number distribution within each element of the system. The fundamental interaction of the radiation with these elements was previously described in Chapter 2.

In this thesis, the "irradiated system" was restricted to the "patient sub-system", assuming that effects from the sub-systems further upstream (i.e. the field production and field shaping sub-systems) would be incorporated into the particles incident on the patient sub-system. Similarly, particles emerging from the patient and incident on the "verification sub-system" can be treated in this "bucket brigade" transport of particles. The pre- and post-patient sub-systems have been ignored throughout this work. However, should the algorithms developed here prove to be successful in the patient sub-system, then it should be possible to deal with these other sub-systems. The kernels and interaction coefficients suitable for the higher atomic number and electron density of the field-shaping devices or

verification detectors would then have to be generated in future work. Ultimately, this would allow comparisons with the empirical exit doses, completing the verification loop from treatment planning to patient dose delivery.

Alternatively, a calculation could be performed for the entire irradiated system (consisting of all sub-systems) in which the source term describes the particles incident upstream on the field production sub-system. This source term would need to be determined (only once) by experimental or Monte Carlo methods. Again, a full range of kernels for all atomic numbers and electron densities encountered in the entire irradiated system is required to support this general approach.

5.1.3 Solution to the General Problem

Once a specific problem has been defined in terms of the radiation source term, the electron and atomic number density distributions of attenuators, and the coefficients describing the interaction of radiation with matter; the problem is solved - theoretically speaking. The solution to the general problem (equation 3.1) involves :

- the determination of the particle fluence differential in particle type and energy everywhere within the irradiated system

- the 'looking-up' of the average energy deposited in a voxel as a function of the particle types and energy incident on a voxel, and of the electron density and atomic number in that voxel.

Unfortunately, both these quantities are extremely difficult to measure or calculate in the general case. A repartitioning and repackaging of the above information was performed in section 3.2.2, which eventually led to a superposition integral with assumptions. If a situation arises in which the assumptions are invalid and the calculated results disagree with empirical results, then the more complex fundamental solution will be required.

5.1.4 Restrictions Placed on the General Problem by the Convolution Approach

In section §3.2.4 we explicitly made additional assumptions to reduce the superposition integral to a *convolution integral*. The violation of an assumption may not prevent the use of the convolution algorithm (e.g. a monoenergetic photon beam). If, on the other hand, the violation of an assumption produces results which differ from empirical results in the dose region of interest (e.g. a heterogeneous irradiated system), then we must revert to the more general superposition integral . The practical impact of these assumptions is discussed in section §5.1.6.

5.1.5 Feasibility of the Convolution Approach

Evaluation of the convolution integral can be performed from one of two viewpoints: the "pitcher", or the "catcher". The pitcher's forward approach slowly develops the entire dose distribution in an incremental fashion; while the catcher's reverse approach determines the total dose received at a single point directly. If a complete dose distribution is to be calculated, then there is no benefit of one approach over the other. However, if the dose is only required at a few select points, the catcher's approach is computationally more efficient!

Chapter 4 dealt with the numerical evaluation of discrete convolutions in both the real (§4.1) and Fourier domains (§4.2 and §4.3). The consequence of the assumptions required by the convolution algorithm and methods of overcoming these assumptions were discussed in section §4.4.

The feasibility of using any dose calculation algorithm in a clinical setting is based on its performance in terms of: accuracy, speed, and ease of use. Each area will be discussed separately.

5.1.5.1 Accuracy

If the criterion for accuracy is to compute the dose to within an error of ±3% in the target volume and critical regions, then the convolution meets this demand in all comparisons with experiment performed in this work, with one exception. For depths between the surface and the depth of maximum dose (3 cm for 15 MV X-rays), the convolution algorithm errs in excess of 3%. This difference may be due to the failure of the present convolution technique to account for electron contaminants, and to experimental difficulties of performing dosimetry in this zone (e.g. diode response).

The convolution calculation compared well to the measured dose distribution for a 10x10 cm^2 field of 15 MV X-rays. The conventional CBEAM calculation algorithm used clinically agreed more closely with the empirical data, but this is not surprising, since in this situation this algorithm reproduces measured data it uses as its starting data base! When both algorithms are forced to be predictive (e.g. the example of a bar occluding the central axis of a beam), the convolution algorithm outperforms CBEAM.

Let us summarize the impact of the assumptions required by the convolution method (see section §4.4):

- **a monoenergetic photon beam.** Clinical X-ray beams are poly-energetic. The convolution algorithm can accomodate this situation by either using an effective energy and attenuation coefficient, or by performing a series of convolutions - one for each spectral component of the energy spectrum. The latter method accurately models "beam hardening" (and is more time-consuming), whereas the effective energy and attenuation coefficient method does not.

Our results indicate that an effective mono-energetic beam of 5 MeV was a sufficient representation for the 15 MV X-ray beam. A method was briefly

explained for determining the energy spectrum of a clinical beam. Further investigation is required into this new technique and perhaps other spectrometric methods.

- **all incident photons travel along a ray from a point source.** Reasonable agreement was achieved with the use of a "point" source (Figure 4.26). Even better agreement in the penumbra is achievable if the finite source size is considered, perhaps by "blurring" the kernels.

- **an infinite SSD.** In this work, experimental measurements were made with large SSD's in order to approach an infinite SSD. In these situations, the calculation of the fluence along mildly divergent rays was adequate (Figure 4.26). For small SSD's, the convolution kernels may also need to be "tilted" prior to energy deposition. If this is the case (e.g. large fields, short SSD), the superposition model, instead of the convolution model, is necessary with a concomitant sacrifice in calculation speed.

The large SSD may have also resulted in more energy being deposited farther beyond the beam edges, than either the convolution or CBEAM algorithms have predicted. Further experimental measurements are necessary in these low dose zones beyond the beam "edge" (Figure 4.26).

- **an irradiated system which is homogeneous and water-equivalent.** An irradiated system which is inhomogeneous prevents the use of a convolution algorithm since the kernel is spatially variant. For this case, the superposition integral needs to be evaluated and, again, kernels need to be generated for non-water materials.

- **an irradiated system of infinite size.** The effects of a finite phantom should be most visible in the "build-up" region where kernel modification might be required. The "build-up" region in a finite phantom was modelled well by the convolution model for Cobalt-60 (Figure 4.4). Thus, it appears

that kernel modifications are not necessary for radiation beams incident

normal to a flat surface.

The oblique incidence of a radiation field on a flat surface needs to be

examined in order to develop acceptable patient "contour corrections". The

performance of the convolution model in the "build-down" region at the exit

side of the patient also needs to be tested.

Work required in the near future to evolve the convolution method includes:

- comparison to more experimental data in order to determine the practical

  significance of the convolution assumptions.

- comparison to Monte Carlo calculations to determine the agreement with the

  idealized 'convolution' situation.

- extension to 3D. Although this is straight forward, is it really necessary??

  We need to investigate the use of a "multi-slice" description of the patient and

  dose distribution versus a "single-slice" approach with symmetry

  assumptions.

More advanced work needed in the next generation of the "convolution" algorithm

(e.g. superposition) includes:

- establish kernel modification algorithms to handle inhomogeneities and

  contour corrections.

- investigate the use of filters in Fourier space as a technique for implementing

  such spatially varying kernels.

- transport particles from one sub-system to another sub-system (e.g. scattered

  photons and electrons produced by retracted tissue compensators).

- investigate the the application of the convolution technique to electron beams. This might also solve the electron contamination problem noted earlier (section §4.4.6).

- once the forward problem (i.e. the calculation of a dose distribution) is solved, investigate the deconvolution of an "ideal" dose distribution in order to determine the optimal position and shape of therapeutic beams. This could greatly automate the treatment planning procedure.

5.1.5.2   Calculation Speed

We established theoretical speed gains by performing the calculation in Fourier space versus real space (section §4.3.2). As an example, we found Fourier space calculations for a 64X64 dose matrix were 16 times faster than the real space calculation with a large kernel (63x63), 4 times faster than the present CBEAM algorithm, and 2 times faster than the real space calculation with a small kernel (16x15).

Areas deserving further investigation include:

- specialized hardware (e.g. an array processor or specialized micro processors)

- better FFT algorithm (e.g. a full 2D FFT, or by 'packing' the input function).

- calculation of the dose at a minimum number of optimally-located points (e.g. few points in regions of low dose gradient and more points in regions of high dose gradient)

- the use of other types of transforms

- the possibility of performing a convolution with a kernel in spherical geometry and a fluence in a Cartesian or fan geometry

5.1.5.3   Ease of Use

Because the convolution algorithm is based on a Green's function as a modular building block, it has the versatility to be applied in different situations[13] which previously required multiple algorithms (e.g. CBEAM and IRREG). The benefits of a unified approach to different problems are:

- the treatment planning process becomes more consistent from an operator's viewpoint since only one set of "input" data is required

- maintenance of the software becomes easier because of reduced "bulk" and redundancy in the program code.

- maintenance of the database is simpler since only one set of "tweaking" parameters is required

It is expected, that future work in this area will make the convolution algorithm available for routine clinical use on the Alberta Treatment Planning (ATP) computer.

---

[13]The convolution algorithm has the versatility to model dose distributions resulting from pencil beam scanning hardware (Alonso 1980) which other algorithms would find impossible or very difficult to model.

5.2 Conclusions

Table 5.1 summarizes the dose calculation algorithms discussed in this work which make use of various fluence and kernel calculations to determine a dose distribution. Figure 5.1 shows the hierarchy of these algorithms; the most general algorithm at the top, and the least general at the bottom.

Solution name	Fluence contains	Kernel contains energy deposition plus
general	γ and $e^\pm$ transport	nil
approach One	all γ transport	$e^\pm$ transport
approach Two	primary γ transport	$e^\pm$ & secondary γ transport
approach Three	surface γ	$e^\pm$ & all γ transport

Table 5.1. Solutions to the dose calculation problem for a megavoltage photon beam.

The difficulty with the general solution and approach One are the complexity of the particle fluence calculations. This is not the case for approach Two, which included the promising superposition and convolution algorithms in which the calculation of the primary fluence is trivial. However, the requirement of an invariant kernel by the convolution algorithm limits its applicability to homogeneous irradiated systems in which the kernels do NOT need to be 'aligned' with the fluence ray-lines. If the kernel variance is too great, then the superposition algorithm is appropriate. If the results obtained by the superposition approach still disagree significantly with experimental data, then development of the "higher order" algorithms is unfortunately required.

The convolution algorithm requires the primary photon fluence everywhere within the irradiated system, and convolution kernels describing the energy spread as a result of a primary photon impulses. The extent of the kernel and size of the kernel voxels is critical in order to correctly model the dose situation of interest.
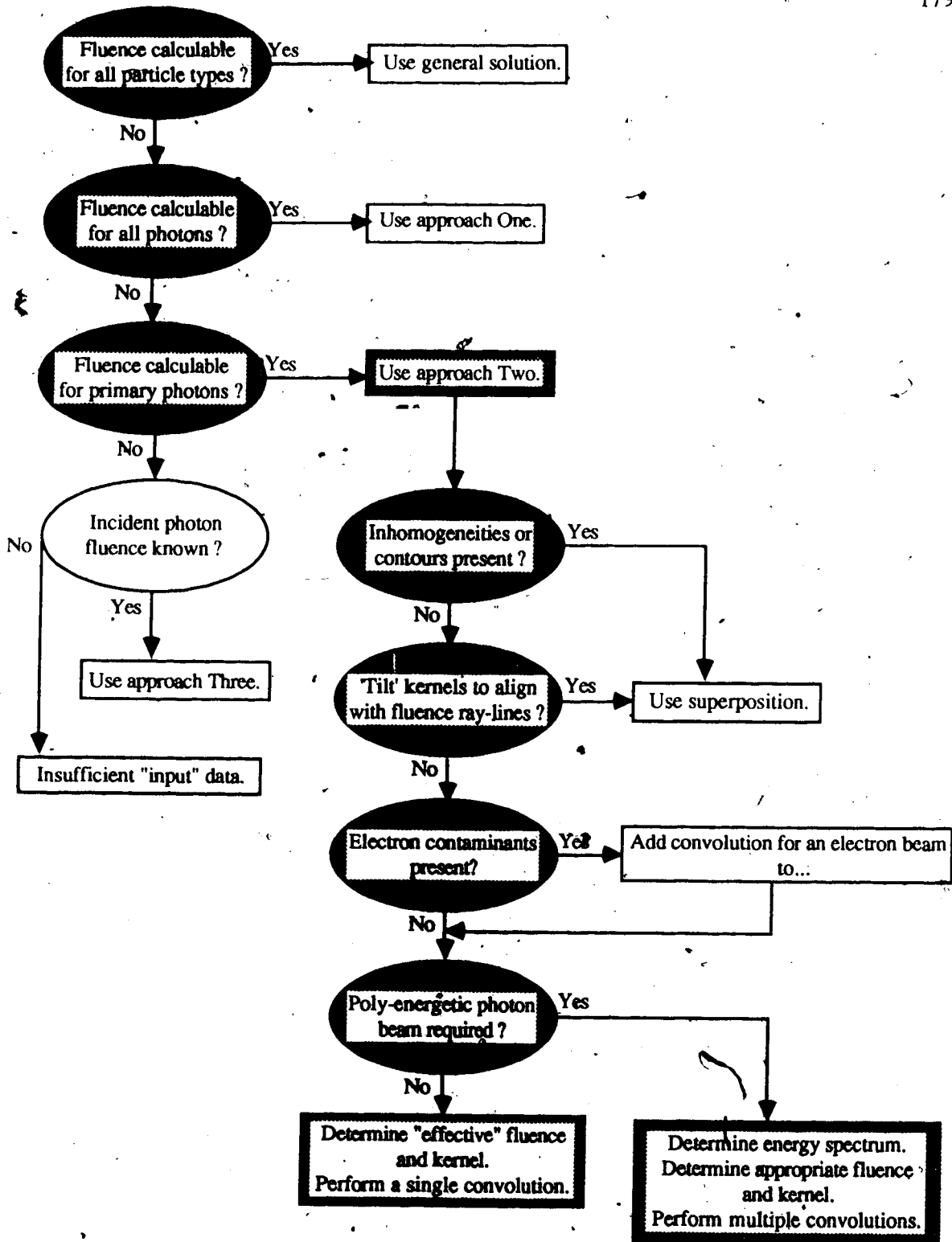
Figure 5.1. Which calculation algorithm should be used ?

The answer to the question "Is convolution a useful technique for calculating megavoltage photon beam dose distributions ?" depends upon the region in which the dose distribution is desired! For homogeneous situations (e.g. a water calculation) the convolution method is very useful but so are other well established algorithms (e.g. CBEAM). The convolution method has shown better agreement with experimental data in situations of a predictive nature than CBEAM. The application of Fourier techniques has been studied and yielded significant reductions in computation time. Other algorithms used for "inhomogeneous corrections" (e.g. TAR / SAR based) first require a calculation in water and would benefit significantly from this speed gain.

For inhomogeneous situations, the convolution technique is not appropriate; although, its "cousin" superposition technique may be applied. Unfortunately, the speed gains by using Fourier techniques are *not* realizable for this case.

The advantages of the convolution method are well known:

> **Accuracy.** Intrinsic modeling of the build-up curve, beam penumbra, and other situations of electronic disequilibrium.

> **Speed.** Calculation time savings by software (e.g. FFT's) and hardware (e.g. specialized processors).

> **Ease of use.** Unification of algorithms for beams of any size, shape, and possibly particle type (e.g. electrons).

This method is progessing well, with frantic development sometimes masking the underlying assumptions. This work is an objective appraisal of the method and its potential.

This thesis has established the "scaffolding" and relationships of various dose calculation algorithms which exist or need to be developed. The "plans" for these new methods have been proposed, and construction of the convolution algorithm has been

completed in this work. The software "tools" developed during the convolution phase will be useful during the development of the superposition algorithm.

The author remains hopeful that the footing developed thus far will permit the incorporation of the convolution/superposition algorithms into routine treatment planning. The ultimate goal remains to treat the cancer patient optimally with radiation.

Bibliography

Ahnesjö, A. (1984): Application of transform algorithms for calculation of absorbed dose in photon beams. in Proceedings of the Eighth International Conference on the Use of Computers in Radiation Therapy (IEEE Computer Society, Siver Spring, MD), 17-20

Ahnesjö, A. (1987): Invariance of convolution kernels applied to dose calculations for photon beams. in Proceedings of the Ninth International Conference on the Use of Computers in Radiation Therapy (Elsevier Science Publishers, Amsterdam, the Netherlands), 99-102

Ahnesjö, A., Andreo,P., and Brahme, A.(1987): Calculation and application of point spread functions for treatment planning with high energy photon beams. Acta. Onc. 26, 49-56

Alonso, J.R. (1980): Parameters required by the accelerator design team. in MARIA Design Symposium: Radiation Oncology Vol II. U of A Press

Andreo, P. and Brahme, A. (1983): Fluence and absorbed dose in high energy electron beams, Acta. Rad. Suppl. 364, 25

Andrews, R.A. and Mackie, T.R. (1986): Spherical to Cartesian Transformation using Adaptive Quadrature, Allan Blair Memorial Clinic, Regina, Saskatchewan, internal communications

Antolak, J., Mah, E., Battista, J.J. and Scrimger, J.W. (in press): Acquisition and Display of Radiation Dose Distributions, Using Microcomputer Technology.

Attix, F.H. (1986): Introduction to Radiological Physics and Radiation Dosimetry, John Wiley and Sons, Inc.

Attix, F.H., Roesch, W.C. (1968): Radiation Dosimetry, 2nd edition, Volume 1, Academic Press, New York

Battista, J.J. and Field, G.C.(1986): Convolution Workshop, Regina 1986

Battista, J.J. et.al.(1979): CT Scanners in Radiotherapy in Europe, Br.J.Radiol., 147-151

Battista, J.J., Field, G.C., Santon,L.W., and Barnett, R.,(1984): Radiotherapy Planning on a Vax-11/780 computer. In: Computers in Radiation Therapy, p 489. Proceedings of Eighth International Conference of the Use of Computers in Radiation Therapy, Toronto. IEEE Computer Society Press.

Berger, M.J. (1963): Monte Carlo Calculation of the penetration and diffusion of fast charged particles, in Methods of Computational Physics, p 135, edited by B. Alder, S.Fernbach eds., vol 1, Academic Press, New York

Bielajew, A.F. (1987): private communication

Boyer, A.L. (1984): Shortening the caluclation time of photon dose distributions in an inhomogeneous medium, Med. Phys. 11(4),.552

Boyer, A.L. (1986): Convolution workshop, personal communication (flying sub-arrays)

Boyer, A.L. (1987): RSNA poster paper

Boyer, A.L. (1988): Relationship between Attenuation Coefficients and Dose-Spread Kernels. Radiat. Res. 113, 235-242

Boyer, A.L. and Moc, E.C. (1984): Photon beam modelling using Fourier transform techniques. In: Computers in Radiation Therapy, p 14. Proceedings of Eighth International Conference of the Use of Computers in Radiation Therapy, Toronto. IEEE Computer Society Press.

Boyer, A.L. and Moc, E.C. (1985): A photon dose distribution model employing convolution calculations. Med.Phys. 12, 169

Boyer, A.L. and Mok, E.C. (1986): Calculations of photon dose distributions in an inhomogeneous medium using convolutions, Med. Phys. 13(4), 503

Boyer, A.L. and Mok, E.C. (1986): Brachytherapy seed dose distribution calculation, employing the fast Fourier transform. Med.Phys.13(4), 525-529

Brigham E.O. (1974): The Fast Fourier Transform (Prentice-Hall, Englewood Cliffs, NJ

Byte, (1986): Raising the Titantic. Byte March, 108

Carlsson, G.A. (1978): Basic Concepts in Dosimetry. A Critical Analysis of the Concepts of Ionizing Radiatio and Energy Imparted, Radiat. Res. 75, 462-470

Carlsson, G.A. (1979): Definition of Energy Imparted: A new formulation adapted to exact solutions of the absorbed dose equation under nonequilibrium conditions, Rad. Res. 77, 209-220

Carlsson, G.A. (1981): Absorbed Dose Equations. On the Derivation of a General Absorged Dose Equation and Equations Valid for Different Kinds of Radiation Equilibrium, Rad. Res. 85, 219-237

Carlsson, G.A. (1982): Quantities and Concepts Used in Radiation Dosimetry, Int. J. Appl. Radiat. Isot 33, 953-965

Case, K.M. (1957): Transfer problems and the reciprocity principle. Rev. Mod. Phy. 29, 651-663

Chin, L.M. et. al.(1985): Progress in 3-D treatment planning for photon beam therapy, Int. J. Rad. Onc. Biol. Phys. 11, 2011

Chui, C.S., Mohan, R. and Lidofsky, L. (1984): Differential pencil beam dose computation model (abstract). Med. Phys. 11, 392

Clark, M. and Hanson, K. (1962): Numerical Methods in Reactor Analysis, Academic Press, New York

Convolution (1986): Convolution Workshop, Regina, Saskatchewan, Canada

Cooley, J.W. and Tukey, J.W. (1965): An algorithm for the machine calculation of complex Fourier series. Math. Computation. Vol 19, pp. 297-301

Cochran, W.T., Cooley, J.W., Favin,, D.L., Helms, H.D., Kaenel, R.A., Lang, W.W., Maling, G.C., Nelson, D.E., Rader, C.M., and Welch, R.D. (1967): What is the Fast Fourier Transform?, Proc. IEEE 55, 10, 1664

Courant , R. and Hilbert, D. (1937): Methods of Mathematical Physics, Vol I & II, John Wiley and Sons, New York

Cristy, M. and Williams, L.R. (1983): Applying the reciprocal dose principle to heterogenious phantoms: practical experience from Monte Carlo studies Phys. Med. Biol.28, 1289-1303

Cygler, J., Battista, J.J., Scrimger, J.W., Mah, E., Antolak, J. (1987): Electron Dose Distributions in Experimental Phantoms: A Comparison with 2D Pencil Calculations. Phys. Med. Biol. 32, 1073

Cunningham, J.R. (1972): Scatter-air ratios. Phys. Med. Biol. 17, 42-51

Cunningham, J.R. (1982): in: C.G. Orton (eds.), Progress in Modern Radiation Physics (Plenum, New York) 103-131.

Cunningham, J.R. (1983): Current and Future Develoment of Tissue Inhomogeneity Corrections for Photon Beam Clinical Dosimetry with the Use of CT, in Computed Tomography in Radiation Therapy, editors C.C. Ling, C.C. Rogers, R.J.Morton, Raven Press, New York

Dean, R.D. (1980): A scattering kernel for use in true three-dimensional dose calculations (abstract). Med. Phys. 7, 429

Dudgeon, D.E. and Mersereau, R.M. (1984): Multidimensional Digital Signal Processing, Prentice-Hall, New Jersey

Duderstadt , J.J. and Martin, W.R. (1979): Transport Theory, Wiley & Sons, New York

Evans, R.D. (1955): The Atomic Nucleus, McGraw-Hill Book Company, Inc., New York

Fano, U., Spencer, L.V., and Berger, M.J. (1959): Penetration and diffusion of x-rays. In: Handbuch der Physik (S.Flugge, ed.) Vol. 38, Part II, p 660. Springer-Verlang, Berlin

Field, G.C., Battista, J.J. (1986): Photon Dose Calculations Using Convolution in Real and Fourier Space: Assumptions and Time Estimates, in Proceedings of the Ninth International Conference on the Use of Computers in Radiation Therapy

Fitzgerald, J.J., Brownell, G.L. and Mahoney,F.J. (1967): Mathematical Theory of Radiation Dosimetry, Gordon & Breach, New York

Ford, R.L., Nelson, W.R.(1978): The EGS code system- Version 3. Stanford linear accelerator report 210

Goitein, M. (1982): Limitations of two-dimensional treatment planning programs, Med. Phys. 9(4) 580.

Heitler, W. (1954): Quantum theory of radiation, third edition, pp 215-218, Oxford University Press, Fair Lawn, N.J.

Henkelman, R.M., Poon,Y.P., and Bronskill, M.J. (1984): Is magnetic resonance imaging useful for radiation therapy planning? 8 ICCR, pg 181-185

Hogstrom, K.R., Mills, M.D. and Almond, P.R. (1981): Electron beam dose calculations. Phys. Med. Biol. 26, 445-459

Hubbell, J.H. (1969): Photon cross sections, attenuation coefficients, and energy absorption coefficients from 10 keV to 100 GeV. NSRD-NBS 29. Washington, D.C. U.S Bureau of Standards

ICRU 24: Determination of Absorbed Dose in a Patient Irradiated by Beams of X or Gamma Rays in Radiotherpay Procedures, ICRU, Washington, D.C. 1976

ICRU 28: Basic Aspects of High Energy Particle Interactions and Radiation Dosimetry, ICRU, Washington, D.C. 1978

ICRU 33: Radiation Quantities and Units, International Commission on Radiation Units and Measurements, Washington 1980

Jeffreys & Jeffreys (1956): Methods of Mathematical Physics, Cambridge University Press

Jing, M. and Boyer, A.L. (in press): Cobalt-60 wedged field modeling by FFT convolution.

Johns, H.E., Darby, E.K., Haslam, R.N.H., Katz, L., Harrington, E.L.(1949): Depth dose data and isodose distributions for radiation from a 22 MeV. betatron. Am.J.Roent.&Rad.Ther., 62, 257-268

Johns, H.E., Cunningham, J.R.(1983): The Physics of Radiology, Charles C Thomas, Springfield, Illinois

Kase, K.R., Bjärngard, B.E., Attix, F.H. (1985): The Dosimetry of Ionizing Radiation, Volume 1, Academic Press, New York

Kase, K.R. and Nelson, W.R. (1978): Concepts of Radiation Dosimetry, Pergamon, New York

Keller, A.M., and Chmelevsky, D. (1975): Concepts of microdosimetry I. Quantities. Radiat. Environ. Biophys. 12, 61-69

Kornelson, D. (1986): Modification of electron kernels, presented at the Convolution workshop

Leung, P.M.K., Sontag, M.R. , Maharaj, H. and Chenery, S. (1976): Dose measurements in the build-up region for Cobalt-60 therapy units. Med.Phys.Biol. 3, 169-172

Ling, C.C., Rogers, C.C , Morton, R.J. (1983.): Computed Tomography in Radiation Therapy, Raven Press, New York

Mackie, T.R. (1983): Photon dose calculations using a convolution method that includes non-local electron energy deposition (abstract). Med. Phys. 10, 536

Mackie, T.R. (1984): Ph.D. thesis, University of Alberta

Mackie, T.R. (1987): Calculating Electron Dose Using a Convolution / Superposition Method, in Proceedings of the Ninth International Conference on the Use of Computers in Radiation Therapy, (IEEE Computer Society, Silver Spring, MD)

Mackie, T.R.and Scrimger, J.W. (1984): Computing radiation dose for high energy X-rays using a convolution method. in Computers in Radiation Therapy, p36. Proceedings of the Ninth International Conference on the Use of Computers in Radiation Therapy, (IEEE Computer Society, Silver Spring, MD)

Mackie, T.R., Scrimger, J.W., Battista, J.J.(1985): A convolution method of calculating dose for 15-MV xrays. Med.Phys. 12, 188-196

Mackie, T.R., El-Khatib, E., Scrimger, J.W., Battista, J.J., Van Dyk, J. and Cunningham, J.R. (1985b): Lung dose corrections for 6- and 15- MV x rays. Med.Phys. 12, 327-332

Mackie, T.R., Ahnesjö, A., Dickof, P., Snider, A. (1987a): Development of a Convolution / Superposition Method for Photon Beams, in Proceedings of the Ninth International Conference on the Use of Computers in Radiation Therapy, (IEEE Computer Society, Silver Spring, MD)

Mackie, T.R., Bielajew, A.F., Rogers, D.W.O. and Battista, J.J. (1988): Generation of photon energy deposition kernels using the EGS Monte Carlo code. Phys.Med.Biol. 33, 1-20

Matthews, J.L., Owens, R.O. (1973): Accurate Formulae for the Calculation of High Energy Electron Bremsstrahlung Spectra, Nucl. Instr. and Meth. 111, 157-168

Mohan, R. and Chui, C. (1985): Validity of the concept of separating primary and scatter dose. Med. Phys. 12, 726-730

Mohan, R. and Chui, C (1987): Use of fast Fourier tranforms in calculating dose distributions for irregularily shaped fields for three-dimensial treatment planning, Med. Phys. 14, 70-77

Mohan, R., Chui, C., Lidofsky, L.(1985): Energy and angular distributions of photons from medical linear accelerators,Med.Phys. 12, 592

Mohan, R., Chui, C., Lidofsky, L.(1986): Differential pencil beam dose computation model for photons. Med.Phys. 13, 64-73

Morse, P.M. and Feshback, H. (1953): Methods of Theoretical Physics, Vol I & II, McGraw-Hill Book Company, New York

Nahum, A.E. (1985): The Computation of Dose Distrutions in Electron Beam Radiotherapy, Umeå University

Nahum, A.E. (1986): Radiation Transport Calculations using EGS4, lecture 5, Ottawa, Ontario, 1986

Nelms, A.T. (1953): Graphs of the Compton energy-angle relationship and the Klein-Nishina formula from 10 keV to 500 MeV. National Bureau of Standards Circular 542

NBS 583: X-ray Attenuation Coefficients from 10 kev to 100 Mev, National Bureau of Standards circular 583

Nelson, W.R., Hirayama, A., Rogers, D.W.O. (1985): The EGS4 code system. Stanford linear accelerator report 265

Nelson, W.R. and Jenkins, T.M. (1980): Computer Techniques in Radiation Transport and Dosimetry, Plenum Press, New York

O'Connor, J.E. (1957): The variation of scattered X-rays with density in an irradiated body. Phys. Med. Biol. 1, 352

O'Connor, J.E. (1984): The density scaling theorem applied to lateral electronic equilibrium. Med. Phys. 11, 678

O'Neill, M.A. (1988): Faster than Fast Fourier. Byte April, 293-300

Perry, D. (1988): Ph.D. thesis, University of Alberta

Pruitt, J.S. and Loevinger, R.(1982): The photon-fluence scaling theorem for Compton-scattered radiation. Med. Phys. 9, 176-179

Purdy, J.A. (1982): Photon Beam Modeling and Dose Calculation Algorithms Used in Treatment Planning Computers, Continuing Education Lecture - 24th AAPM, New Orleans, Louisiana (1982)

Raeside, D.E. (1976): Monte Carlo principles and applications. Phys. Med. Biol. 21, 181-197

Roesch, W.C. (1956): Penetration of gamma ray secondaries. U.S. At. Energy Comm. Rept. HW-46697

Roesch, W.C. (1958): Dose for nonelectronic equilibrium conditions. Radiation Research 9, 399-410

Roesch, W.C. (1968): Mathematical theory of Radiation Fields, in Radiation Dosimetry, F.H. Attix, W.C. Roesch, E.Tochilin, eds., 2nd edition, Vol 1, 229-274, Academic Press, New York

Rossi, H.H. and Roesch, W.C. (1962): Field equations in dosimetry. Radiat. Res. 16, 783-795

Skarsgard, L.D., Johns, H.E., Green, L.E.S. (1961): Iterative response correction for a scintillation spectrometer. Radiat. Res. 14, 261-280

Spencer, L.V. (1971): Remarks on the theory of energy deposition in cavities, Acto Radiol. Ther. Phys. Biol. 10, 1-20

Sontag, M.R. (1979): Ph.D. thesis, University of Toronto

Sontag, M.R. and Cunningham, J.R. (1977): Corrections to absorbed dose calculations for tissue inhomogeneities, Med. Phys. 4, 431

StatWorks,(1985):, Cricket Software, pg 59

Task Group 10 (1975): Code of Practice for X-ray therapy linear accelerators, Med. Phys. 2, 110-121

Ulmer, W.(1982): On the application of stochastic partition functions for the computation of lateral profiles and depth doses in radiotherapy. Strahlentherapie 158, 305

Ulmer, W.(1983): On the application of stochastic partition functions for the computation of lateral profiles and depth doses in radiotherapy. II. Modifications of intensity and depth dose profiles by wedge filters. Strahlentherapie 159, 559

Van de Geijn, J. (1987): The extended net fractional depth dose: Correction for inhomogeneities including effects of electron transport in hpoton beam dose calculation, Med Phys. 14, 84-92

Van de Geign, J. (1972): Revised and expanded version of ECTDOS. A program for treatment planning in external beam therapy, Comp. Progs. in Biomed 2, 169

Van de Geign, J., Chu, C., and Frederickson, H.A. (1980): A unifed 3D model for external beam dose distributions, in Proceedings of the 7th International Conference of the Use of Computers in Radiation Therapy, Editor: Y. Umegi, Kawasakiand Toyko, Japan pg 22-26

Yu, C.X., Wong, J.W. and Purdy, J.A. (1987): Photon dose perturbations due to small inhomogeneities, Med. Phys. 14, 78-83

Wong, J.W, Henkleman, R.M., Fenster, A., Johns, H.E. (1981): Second scatter contribution to dose in a Cobalt-60 beam. Med. Phys. 8

Wong, J.W. et.al (1984): The delta-volume method for 3-dimensional photon dose calculations, in Proceedings of the Eighth International Conference on the Use of Computers in Radiation Therapy (IEEE Computer Society, Silver Spring, MD) 26-30

Wong, J.W. and Henkelman, R.M. (1983): A new approach to CT pixel based photon dose calculations in heterogeneous media, Med Phys. 10, 199-208

Appendices

Of shoes - and ships - and sealing wax -
Of cabbages - and kings -
And why the sea is boiling hot -
And whether pigs have wings.

Through the Looking Glass
Lewis Carroll

Appendix A - Calculation Times in Real Space

Let us determine the number of multiplications required to perform a convolution when the dose and fluence array sizes are matched. This implies that we have no interest in any dose that might be deposited beyond the bounds defined by the fluence mat ix, as shown in Figure 4.2. If this is the case, all operations which would deposit energy beyond the fluence matrix can be eliminated. This reduces the number of multiplications and hence decreases the calculation time of real space convolutions. The size of this decrease is the subject of this discussion. Using the catchers point of view, we can place the inverted kernel's interaction voxel on the dose voxel in question and perform the multiplications and additions which lie within the fluence matrix.

Restricting ourselves to 1D for the moment, we shall assume the fluence array and the dose array are both N elements long, and the kernel is M elements long (where M<N and M=top+bottom+1). The process of placing the inverted kernel origin onto a dose voxel is called a step. There will be N steps required during the convolution process, since there are N dose voxels upon which to "land" the kernel origin. The number of multiplications required at step 'i' is given by:

- the number of fluence kernels overlapping pixels upstream of the interaction voxel, min(top, N-i)

- the number of fluence kernels overlapping pixels downstream of the interaction voxel, min(bottom, i-1)

- one multiplication of the interaction voxel with the fluence element

Hence the number of multiplications (m) required for a 1D 'constrained' convolution is:

$$m = \sum_{i=1}^{N} \min(\ top,\ N-i) + \min(\ bottom,\ i-1) + 1$$

$$
= \sum_{i=1}^{N-top} top \cdot \sum_{i=N-top+1}^{N}(N-i) \cdot \sum_{i=1}^{bottom+1}(i-1) \cdot \sum_{i=bottom+2}^{N} bottom \cdot \sum_{i=1}^{N} 1
$$

Evaluating each term. individually yields

$$
\sum_{i=1}^{N-top}(top) = (N-top)top
$$

$$
\sum_{i=N-top+1}^{N}(N-i) = \sum_{i=1-top}^{0}(-i) = \sum_{i=0}^{top-1} i = (top-1)top/2
$$

$$
\sum_{i=1}^{bottom+1}(i-1) = \sum_{i=0}^{bottom} i = bottom(bottom+1)/2
$$

$$
\sum_{i=bottom+2}^{N} bottom = bottom(N-bottom-1)
$$

Hence, the total number of multiplications is given by

$$
m = (N-top)top + (top-1)top/2 + bottom(bottom+1)/2 + bottom(N-bottom-1) +N
$$

$$
= top[N-(top+1)/2] + bottom[N-(bottom+1)/2] + N
$$

$$
= N(top+bottom+1) - [top(top+1) + bottom(bottom+1)]/2
$$

$$
= NM - [top(top+1) + bottom(bottom+1)]/2
$$

Where we have used the fact that M=top+bottom+1. Note that the number of multiplications is the number required for a full convolution (NM) less those terms that distribute energy beyond the spatial extent of the fluence matrix.

simplest case 1:

top=bottom=0; i.e. 1 voxel kernel

#multiplies $= N(1) - [0+0]/2 = N$

For a 1 element kernel the number of multiplies is simply N, as expected.

simple case 2:

top=bottom=1;

#multiplies $= N(3) - [2 + 2]/2 = 3N-2$

For a three element kernel the number of multiplies is 3N less one pixel which doesn't overlap on each end, for a total of 2 saved multiplications.

practical case:

top=10, bottom=40

#multiplies $= N(51) - [10(11) + 40(41)]/2 = 51N - 875$

For N=64, the number of multiplications required for the complete convolution is 51(64)= 3264 and the number of multiplications for the restricted convolution is 51(64) - 875= 2389. i.e. only 73% of the multiplications required for a complete convolution need to be performed!!!

Table A.1 shows some estimated savings for a 1D constrained convolution with a fluence and dose matrix of 64 elements.

top	bottom	% of full convolution
15	47	69
13	50	67
10	36	76
3	12	92
31	31	75
23	23	82
15	15	88
7	7	94

Table A.1. Number of multiplications saved in a "constrained" 1D convolution as a percentage of the number of multiplications required in a full convolution.

Now, let us turn our attention to the 2D case. By symmetry we can write the number of multiplications as

$$m = \{ N_1 M_1 - [top(top+1) + bottom(bottom+1)]/2 \}$$
$$X \{ N_2 M_2 - [edge(edge+1) + edge(edge+1)]/2 \}$$

$$= \{ N_1 M_1 - [top(top+1) + bottom(bottom+1)]/2 \}$$
$$X \{ N_2 M_2 - edge(edge+1) \}$$

Table A.1 can be used to determine the savings for a constrained 2D convolution. For each of the two dimensions, look up the reduction in the number of multiplications from Table A.1 and the product yields the savings for a constrained 2D convolution.

Similarly for 3D case, we can write the number of multiplications as

$$\#multiplies = \{ N_1 M_1 - [top(top+1) + bottom(bottom+1)]/2 \}$$
$$X \{ N_2 M_2 - edge(edge+1) \} \quad X \quad \{ N_3 M_3 - edge(edge+1) \}$$

Table A.2 shows the reduction in the number of multiplies by performing a constrained convolution in 2D and in 3D.

top	bottom	edge	2D (% of full)	3D (% of full)
15	47	31	52	39
13	50	23	54	44
10	36	15	67	59
3	12	7	86	81

Table-A.2. Number of multiplications saved in a "constrained" 2D and 3D convolution as the percentage of the number of multiplications required in a full convolution.

Thus, we see that a substantial savings can be achieved when large kernels are used in a constrained convolution.

Appendix B - The Software Toolbox

During this work, computer programs were written in a modular fashion so that each step of the convolution process could be thoroughly examined. The programs of interest are:

Program	Function
FCALC	perform a Fourier space convolution, given transformed fluence and kernel arrays.
FFT	perform a fast Fourier transform, given input array.
FLUENCE	calculate the primary fluence distribution, given mu, field size, SSD, description of any filter present, filter HVL, fluence pixel spacing, fluence array size.
KERNEL	generate a 2D Cartesian kernel from the spherical data base, given incident energy, kernel category, kernel pixel size, kernel dimensions, and many other parameters useful in examining the kernels. This program is a modified version of SPHTOCRT (Andrews and Mackie 1986).
RCALC	perform a real space convolution, given fluence and kernel arrays.
REFORMAT	renormalize, magnify, or translate an array of data. Generate one of three types of output data files: colour image, black and white image, ascii text.
SHOW	display images on a graphics monitor as a black and white image, or a colour image. Multiple images can be displayed.

APPENDIX   C

Photon Dose Calculations Using Convolution in Real and Fourier Space:

Assumptions and Time Estimates

This appendix has been removed due to copyright protection.

The contents are contained in

The Use of Computers in Radiation Therapy
I.A.D. Bruinvis et. al. (Editors)
Elsevier Science Publishers B.V.
North-Holland, 1987, pp 103-106.